Numerical Investigation on Shape Impact of Deformable Droplets on Evaporation and Combustion: Method Development and Characterization

Meha Setiya

Dissertation submitted to the Faculty of the
Virginia Polytechnic Institute and State University
in partial fulfillment of the requirements for the degree of

Doctor of Philosophy
in
Mechanical Engineering

John Palmore Jr., Chair
Danesh Tafti
Joseph Meadows
Olivier Coutier-Delgosha

July 14, 2023
Blacksburg, Virginia

Keywords: Droplets, Evaporation, Combustion, DNS, Computational Fluid Dynamics

Copyright 2023, Meha Setiya

Numerical Investigation on Shape Impact of Deformable Droplets on Evaporation and Combustion: Method Development and Characterization

Meha Setiya

(ABSTRACT)

Inspired by the dilute spray regime in spray combustion, this dissertation explores the evaporation and combustion of an isolated droplet. Under a highly convective environment inside a gas combustor, due to imbalance of inertial and surface tension forces, the droplets of larger size in sprays exhibit notable deformations from spherical to non-spherical shapes. Such shape changes are generally observed but not quantified in experimental studies. Therefore, the effect of this deformation on droplet combustion dynamics is unknown yet. To bridge this gap, a comprehensive investigation of an isolated freely deforming droplet can be insightful as it can reveal more about the interaction of droplet shape with its evaporation and combustion. This work attempts to analyze and quantify the impact of such deformations on evaporation and combustion using interface-capturing Direct Numerical Simulation approach.

With the focus on small-scale processes involved in evaporation as it is a pre-step for combustion, this dissertation first covers a thorough examination on evaporation of a deformable droplet under both natural and forced convection. A single component jet-fuel surrogate n-decane is chosen. To ensure that the droplet remains stationary through out its lifetime, a novel numerical method called "gravity update method" is developed and implemented.

The results obtained from these two separate studies are validated against experimental results and analytical correlations respectively. The findings from the investigation of droplet evaporation under forced convective flow at moderate Reynolds numbers are noteworthy. The droplet shape under such flow conditions is governed by Weber number (We) which is a ratio of inertial force to surface tension force. The results demonstrated upto 20% enhancement in total evaporation rate for highly deformed droplets. This improvement is a net results of increased droplet surface area and alteration in the distribution of local evaporation flux ($\dot{m}''$). It is found that $\dot{m}''$ is proportional to its curvature up to the point of flow separation which agrees with low Re theories on droplet evaporation by Tonini and Cossalli (International Journal of Heat and Mass Transfer 2013), Palmore (Journal of Heat Transfer 2022). Beyond the flow separation point, evaporation flux distribution depends on the boundary layer development and flow evolution downstream of the droplet. For highly deformed droplets, a larger wake region creates favorable fuel vapor gradients and promotes mixing in droplet wake, hence higher evaporation flux.

Such positive impact of droplet deformation on total evaporation rate motivated further investigation on droplet combustion under a low Reynolds number convective flow. High pressure and temperature gas flow leads to Damköhler number is higher than 1. This favors the generation of envelope type flame. The results show overall little sensitivity to combustion related parameters despite the droplet shape change and significant (upto 9%) enhancement in total evaporation rate. It is also noted that while burning, droplets do not reach critical deformation conditions and break-up even beyond the critical Weber number, suggesting the suppression of deformation due to faster evaporation rate.

The findings presented in these studies provide substantial evidence for the interaction between droplet shape and flow dynamics. Therefore, it demonstrates the potential for enhancing the existing numerical models and analytical correlations by accounting the influence of droplet shape.

Numerical Investigation on Shape Impact of Deformable Droplets on Evaporation and Combustion: Method Development and Characterization

Meha Setiya

(GENERAL AUDIENCE ABSTRACT)

This work is inspired by the spray combustion in gas turbines where the pressurized liquid fuel jet is injected in the combustion chamber and converts into dilute sprays after undergoing series of processes. Due to the presence of higher air to fuel ratio for the these spray droplets, they become the localized combustion sites with rapid evaporation rates. Understanding the evaporation of these droplets becomes crucial, as it sets the stage for their subsequent combustion. In attempt to understand this chemically and fluid-dynamically complex phenomenon, abundant experimental studies are available with focus on overall atomization process and velocity field evolution. However, they lack in resolving the small-scale processes which govern the evaporation, therefore combustion.

With the intent to investigate in detail about the combustion aspect, this problem is reduced to analyzing behavior of isolated droplets. Despite the sophisticated measurement technologies particle-scale processes such as temperature and species mass fraction evolution are yet unknown. Moreover, majority of these studies are performed with simplifying assumptions. assumption has been that the droplet remains spherical throughout its lifetime. However, in practical applications, particularly when exposed to convective and turbulent environments, droplets can undergo significant deformation due to presence of inherent surface tension of liquid. This deformation can influence their evaporation and burning rates. Additionally,

the droplet's shape governs the flow field around it, potentially altering droplet-droplet interactions.

Direct Numerical Simulation (DNS) approach is one of the numerical methods which can resolve both the phases. It offers a promising approach to reveal these small-scale details, such as droplet shape, vapor and temperature field around a droplet, droplet-droplet interaction, droplet motion etc. With the aim to bridge this gap, this dissertation focuses on the study of evaporation and combustion of an isolated deformable droplet under various conditions.

Acknowledgments

Reaching this point, where I am writing this acknowledgement, marks a significant milestone in my academic journey. I am deeply grateful to the multitude of individuals who have supported and inspired me along the way.

First and foremost, I would like to express my deepest gratidue to my advisor, Dr. John Palmore Jr. for his unwavering support, guidance, and invaluable expertise throughout this journey. His insightful advice, encouragement, and continuous belief in my abilities have been a constant source of motivation.

I am also immensely thankful to the members of my advisory committee, Dr. Danesh Tafti, Dr. Joseph Meadows, Dr. Olivier Coutier-Delgosha, for their valuable insights, constructive feedback, and scholarly expertise. Their thoughtful comments and suggestions have greatly enriched this thesis and improved its overall quality. I am grateful for their time and commitment for reviewing my work and providing guidance. I would like to extend my appreciation to the staff of Mechanical Engineering department for their efforts in ensuring a seamless journey.

I would also like to acknowledge the contribution of my colleagues at CAMPhyRE group and fellow researchers whose support and discussions have enriched my research experience at Virginia Tech. Their enthusiasm, knowledge sharing, and patience to mull over problems have been instrumental in overcoming various challenges encountered during this research.

Lastly, it is difficult to put into words the immense gratitude I have for my family and family away from family, who have consistently shown unwavering love, encouragement, and

understanding. Their belief in me, patience during challenging times, and continuous support have been the pillars of my strength. I am truly blessed to have such amazing support system in my life.

Contents

List of Figures **xi**

List of Tables **xv**

1 Introduction **1**

1.1 Motivation 1

1.2 Scope and Organization of the Dissertation 6

2 Numerical Framework **9**

2.1 Introduction 9

2.1.1 Multiphase Flows and their Applications 9

2.1.2 Challenges in Multiphase Flows 10

2.1.3 Dispersed Flows 11

2.2 Current Numerical Framework 16

2.2.1 Interface Capturing Method 16

2.2.2 Conservation of Mass and Momentum 17

2.2.3 Conservation of Scalars 18

2.2.4 Matching Conditions 20

3 Development of Numerical Method to Study Droplet Evaporation **22**

3.1 Introduction 23

3.2 Gravity Update Method 23

3.2.1 Tests for Droplet Motion Under Planar Flow 25

3.3 Effect of Straining Flow on Droplet Evaporation 28

3.4 Conclusions . . . 32

4 Evaporation of Deformable Droplet Under Forced Convection 34

4.1 Introduction . . . 35
4.2 Methodology . . . 40
4.2.1 Flow Solver . . . 40
4.2.2 Quasi-steady Evaporation . . . 41
4.3 Numerical Setup . . . 41
4.4 Results and Discussion . . . 43
4.4.1 Grid Independence Study . . . 43
4.4.2 Effect of Droplet Shape on Evaporation . . . 48
4.5 Conclusions . . . 58

5 Evaporation of Deformable Droplet Under Natural Convection 62

5.1 Introduction . . . 63
5.2 Methodology . . . 68
5.2.1 Experiment-1 Methodology . . . 68
5.2.2 Numerical Methodology . . . 69
5.3 Problem Formulation . . . 71
5.3.1 Numerical Setup . . . 71
5.3.2 Initial Temperature of Liquid and Gas Phase . . . 72
5.4 Validation . . . 75
5.4.1 Validation against Experiment-1 . . . 75
5.4.2 Validation against Experiment-2 [61] . . . 77
5.5 Effect of Droplet Shape Under Natural Convection . . . 78
5.6 Discussion and Future Work . . . 79

6 Combustion of Deformable Droplet Under Forced Convection 81

6.1 Introduction . . . 82

6.2 Problem Formulation . . . 85

6.2.1 Flow Solver . . . 86

6.2.2 Combustion Mechanism . . . 86

6.3 Numerical Setup . . . 88

6.3.1 Analytical Calculation of Gas Temperature . . . 90

6.4 Results and Discussion . . . 92

6.4.1 Effect of Droplet Shape on Pure Evaporation and Combustion . . . 92

6.4.2 Comparison of 3-D vs 2-D Results . . . 103

6.5 Conclusions . . . 109

7 Summary and Future Work 111

7.1 Summary . . . 111

7.2 Future Work . . . 113

Bibliography 115

List of Figures

1.1 Process of jet breakup [85] 3

2.1 Different regimes of multiphase flow [99] 10

2.2 Classification of approaches to solve multiphase flows 14

2.3 Concept of Volume-of-Fluid method 17

3.1 Numerical setup for testing of gravity update method 26

3.2 2-D test: time history of % shift in x-location of droplet center when $\beta = 0$, $\alpha = 0.5$ (*blue*), 0.05 (*orange*), 0.005 (*yellow*), 0.0005 (*purple*) 27

3.3 3-D test: time history of droplet movement *orange dash line marks* $\beta = 0.5$ *and solid blue line marks* $\beta = 0.05$ 28

3.4 2-D: Nusselt number vs normalized time (t/τ_p) for uniform flow(*blue*) vs straining flow(*red*) 31

3.5 Pseudocolor of the velocity field at $t = 6 \times 10^{-4}s$ 32

4.1 A sketch of numerical setup and boundaries 42

4.2 d^2/d_0^2 vs normalized time for various grids 44

4.3 Nusselt Number (Nu) with cells per droplet diameter (N_{d_0}) 45

4.4 Nusselt number vs Spalding heat transfer number. *Blue solid line: Clift et al., Blue Dash line: Ranz and Marshall, Red markers: Numerical Results [Diamond marker:* $N_{d_0} = 8$, *Triangle marker:* $N_{d_0} = 16$, *Rectangular marker:* $N_{d_0} = 24$, *Circular marker:* $N_{d_0} = 32$*]* 47

4.5 Normalized total evaporation rate $(\dot{m}_{ND})$ vs normalized time (t/τ_P) at $Re = 25$ and $Re = 120$ 50

4.6 Zoomed-in plot for $\dot{m}_{ND}$ vs normalized time at $Re = 25$ 51

4.7 Normalized local evaporation flux $(\dot{m''}_{ND})$ vs non-dimensional time (t/τ_P) at $Re = 25$ and $Re = 120$ 52

4.8 Non-dimensional Surface Area (A/A_0) vs non-dimensional time (t/τ_P) at $Re = 25$ and $Re = 120$ 53

4.9 $Re = 25$: Cross-sectional view of droplet shape at $t/\tau_P = 20$. *Red :* $We = 1$, *Blue :* $We = 4$, *Green:* $We = 8$, *Black :* $We = 12$ 54

4.10 $Re = 120$: Cross-sectional view of droplet shape at $t/\tau_P = 20$. *Red :* $We = 1$, *Blue :* $We = 4$, *Green:* $We = 8$, *Black :* $We = 12$ 54

4.11 $Re = 120$: $\dot{m''}_{ND}$ for different Weber numbers at $t/\tau_p = 20$ 55

4.12 $Re = 120$: Distribution of normalized curvature and normalized $\Delta\dot{m}''$ at $t/\tau_P = 20$ 58

4.13 $Re = 120$: Vapor Mass Fraction and Gas Temperature along the line segment AA'. *Red :* $We = 1$, *Blue :* $We = 4$, *Green:* $We = 8$, *Black :* $We = 12$ . . . 59

5.1 Experiment-1 setup [20] 69

5.2 A sketch of computational domain 71

5.3 $d_0 = 0.375mm$: Experimental results for droplet evaporation under micro-gravity [61]. *Black solid line: Digitized experimental data, Cyan dash line: clipped experimental data, Cyan solid line with filled markers : clipped and shifted experimental data, Blue dash line: analytical solution* 74

5.4 $d_0 = 3.68mm$: Time history of dimensionless squared diameter *Black solid line : measured data, Cyan dash line: Smooth data* 76

5.5 $d_0 = 3.68mm$: Time history of dimensionless squared diameter, *Cyan solid line: Smooth experimental data, Blue dash line: Analytical solution, Magenta solid line : DNS solution, Magenta dash line : Linear trend line* 77

5.6 $d_0 = 0.375mm$: Comparison of time history of dimensionless squared diameter *Cyan solid line with markers : Experimental data [61], Blue dash line: analytical solution, Magenta solid line: Numerical solution, Magenta Dash line : Linear trend line* 79

6.1 A sketch of numerical setup and boundaries 89
6.2 Simple droplet burning model: Temperature variation in the radial direction [108] 91
6.3 Total evaporation rate $[kg/s]$ with t/τ_p at $Re_0 = 25$ 93
6.4 Local evaporation rate $[kg/m^2 \cdot s]$ with t/τ_p at $Re_0 = 25$ 94
6.5 Normalized total surface area with t/τ_p at $Re_0 = 25$ 95
6.6 Psueodcolors of local evaporation flux $[kg/(m^2 \cdot s)]$ at $t/\tau_p \sim 7$ at $Re_0 = 25$. 96
6.7 Psueodcolors of normalized curvature at $t/\tau_p \sim 7$ at $Re_0 = 25$ *Black line marks the liquid-gas interface.* 97
6.8 Psuedocolors of gas temperature $[K]$ at $Re_0 = 25$ at $t/\tau_p \sim 7$. *Yellow line marks the maximum* Y_{Co_2} 98
6.9 Sectional view of droplet and flame shape: $We_0 = 1$ (black) vs $We_0 = 12$ (orange), $Re_0 = 25$. *Maroon line marks flame for* $We_0 = 1$ *and blue line marks flame for* $We_0 = 12$ 99
6.10 Sectional view of droplet shapes at different Weber number at $t/\tau_p \sim 10$, $We_0 = 1$ *(Black)*, $We_0 = 16$ *(Magenta)*, $We_0 = 20$ *(Cyan)* 100
6.11 Comparison of gas temperature for different Weber numbers at $Re_0 = 25$ . . 101
6.12 Sectional view of droplet shape at $We_0 = 20$ at $t/\tau_p \sim 10$. *//Cyan: with combustion, Cyan dashed: without combustion* 102
6.13 Normalized vorticity with vectors of normalized liquid velocity at $t/\tau_p \sim 7$ at $Re_0 = 25$ *Black line marks the liquid-gas interface.* 103

6.14 2-D vs 3-D : Local evaporation flux $[kg/(m^2 \cdot s)]$ with t/τ_p at $We_0 = 12$, $Re = 25$ 104

6.15 2-D vs 3-D : Gas Temperature $[K]$ near L-G interface for combustion at $t/\tau_p \sim 7$, $We_0 = 12$, $Re_0 = 25$ *The maroon box is of size* $l \times w = 20\ \mu m \times 20\ \mu m$ 105

6.16 2-D vs 3-D : Non-dimensional curvature at $t/\tau_p \sim 7$, $We_0 = 12$, $Re = 25$. 106

6.17 2-D vs 3-D : Normalized total surface area with t/τ_p at $We_0 = 12$, $Re = 25$ 106

6.18 2-D vs 3-D : Velocity vector field for combustion at $t/\tau_p \sim 7$, $Re_0 = 25$ *blue line marks the flame* 107

6.19 2-D vs 3-D: Normalized flame stand-off distance (S^*) vs t/τ_p at $Re_0 = 25$. 108

List of Tables

3.1 Fluid properties at the boiling temperature of fuel 26

4.1 Fluid properties at $P_\infty = 20\ atm, T_{boil} = 615K, T_G = 750K$ [1] 42

4.2 % error in Nusselt Number (Nu) 48

4.3 $Re = 120$: Measurements at different points inside wake region 56

5.1 Experiment-1 : Fluid properties at $P_\infty = 101325\ Pa,\ T_{boil} = 447.3\ K, T_L = 340K,\ T_G = 360\ K$ [1] 73

5.2 Experiment-2 : Fluid properties at $P_\infty = 0.5\ MPa,\ T_{boil} = 522.7\ K,\ T_L = 521.69\ K, T_G = 640\ K$ [1] 73

5.3 $d_0 = 3.68mm$: Evaporation coefficient (K) for all cases 77

5.4 $d_0 = 0.375mm$: Evaporation coefficient (K) for all cases 78

6.1 Fluid properties at $P_\infty = 20\ atm,\ T_{boil} = 615\ K,\ T_G = 1400\ K$ 90

6.2 Measurement of flow velocity v and normalized flame length L^* at $Re_0 = 25$ 99

List of Abbreviations

Greek Symbols

α	Liquid volume fraction
$\dot{\omega}$	Chemical reaction rate $[mol/m^3 \cdot s]$
η	Kolmogorov length scale
κ	Local curvature
μ	Viscosity $[kg/(m \cdot s)]$
μ^*	Effective viscosity $[kg/(m \cdot s)]$
ν	Air to Fuel ratio
ϕ	Equivalence ratio
ρ	Density $[kg/m^3]$
ρ^*	Effective density $[kg/m^3]$
σ	Surface tension $[N/m]$

Roman Symbols

Δh_c	Lower heating value of fuel $[kJ/kg]$
$V\!\!\!\!-$	Liquid volume $[m^3]$
A	Pre-exponential factor $[(mol/m^3)^{0.75}(1/s)]$
B_q	Spalding heat transfer number
C_d	Drag coefficient
c_P	Specific heat $[J/(kg \cdot K)]$
d_0	Initial diameter of the droplet $[m]$
Da_0	Initial Damköhler number
E_a	Activation energy $[J/mol]$
Gr_0	Initial Grashof Number
h_{fg}	Enthalpy of vaporization $[J/kg]$
K	Evaporation coefficient (mm^2/s)
k	Thermal conductivity $[W/(m \cdot K)]$
P	Pressure $[Pa]$
R_u	Universal gas constant $[J/(mol.K)]$

Re_0	Initial Reynolds number
T	Temperature $[K]$
U	Incoming air velocity $[m/s]$
W_i	Molecular weight of species ‘i’
We_0	Initial Weber number
Y_i	Species mass fraction of species ‘i’

Subscripts

∞	Far field condition
G	Gas
i	Species number
L	Liquid

Chapter 1

Introduction

1.1 Motivation

The age of industrial revolution started with the invention of internal combustion engine. With the advancement of time, engineers have devised several applications of fuel combustion used in a wide range of industries such as metal industry, glass and ceramic industries, power generation in marine, land-based (automotives) and aviation segment. Different types of fuels such as diesel, petrol (gasoline), Compressed Natural Gas (CNG), Liquified Petroleum Gas (LPG) and biofuels are used in a variety of applications based on their respective requirement [2, 11]. Under the favorable temperature and pressure conditions, these fuels oxidize and release energy which is utilized in various applications. The extent of oxidation of these fuels governs the efficiency of combustion. This further controls the type and level of emissions and the overall quality of combustion. These emissions include carbon dioxide (CO_2), carbon monoxide (CO), NOx, particulate matter with the diameter equal to and less than $2.5\mu m$ (PM2.5), Polycyclic Aromatic Hydrocarbons (PAHs), Volatile Organic Compounds (VOCs) [4]. The rising demand of controlled emissions due to visible climate change has created the need to conduct extensive research on the factors that affect the quality of the combustion process. An in-depth understanding of the combustion phenomenon can open avenues toward development of more efficient and environment-friendly engines.

Specific to the aviation and automotive industry, liquid fuels are generally used due to their higher calorific value, compact energy densities, and ease of storage [39]. In order to burn the fuel efficiently, the pressurized liquid fuel jet is injected through a small orifice into hot pressurized air inside combustion chamber. As described by Reitz [81], the liquid jet exposed to these conditions starts breaking up into larger stretched liquid ligaments in the primary breakup zone. The separated fluid ligaments further break into relatively larger size droplets where the surface tension and inertial stresses compete against each other. This regime of droplet formation is generally called as secondary breakup zone. The larger droplets continue to subdivide further until they are small enough to sustain their shape in turbulent flow. This regime is known as dilute sprays. A pictorial representation of the jet breakup and various regimes is adapted from Roth et al. [85] and shown in Fig. 1.1.

Typically, the dense spray regime covers the primary and secondary breakup zone (spray formation region) and some part of the spray region Fig. 1.1. A typical length scales in this regime are of the order of nozzle diameter in millimeters. This regime has always been difficult to study experimentally [58]. As highlighted in a review by Masri [58], one of the key issues in this regime is to resolve the structure of the liquid filaments and mass depletion rates from the liquid core. This means capturing the three dimensional shape of the liquid fragments along with the velocity field is a difficult task. Despite of using very sophisticated imaging techniques such as planar laser-induced fluorescence (PLIF)[42], the large optical depth due to the liquid core and the dense cloud in the spray region makes the capturing of 3-D nature of flow intractable [51]. Therefore, the majority of the experimental and a few numerical studies [19] mainly focus on the global characteristics of this regime. Some of these characteristics are the velocity field, penetration length, the spray cone/spreading angle and interaction of jet with the wall.

In dilute spray regime, the liquid volume loading is generally less than 1% [21]. This suggests low droplet-droplet interaction i.e. droplet collision and coalescence. Moreover, the size in

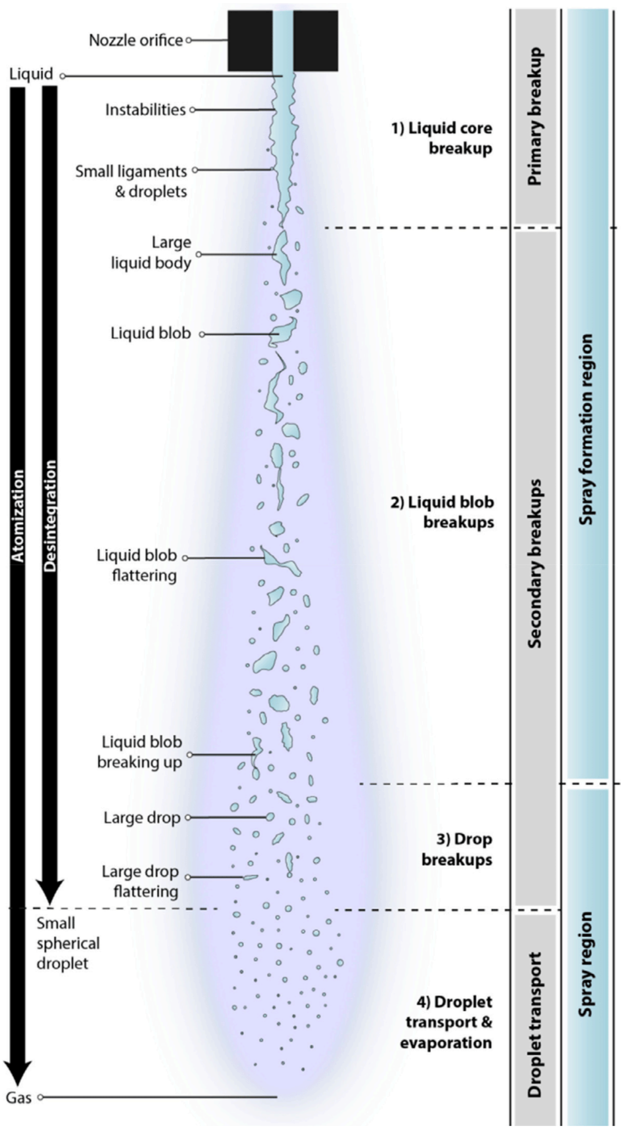

Figure 1.1: Process of jet breakup [85]

dilute spray regime varies from a few micrometers to thousands of micrometers [48, 98]. These droplets in dilute spray regime become local sites where the evaporation rates are faster due to higher air to fuel ratio and turbulence. The turbulence in air-fuel mixture helps in accentuating the chemical and transport processes and the vapor envelope is formed around these droplets [38]. The presence of high temperature compressed air inside combustor favors the initiation of combustion at these local sites. Depending upon the group number

G developed by Chiu et al. [15] the mode of combustion: individual or group combustion in a cloud of droplets is determined.

The combustion research community has shown a keen interest in this regime due to its comparative simplicity in contrast to the dense spray regime. Due to minimum droplet-droplet interaction, this regime is generally reduced to study of an isolated droplet approach such that the focus remains on the droplet evaporation, mixing and its interaction with the external flow. Within the dilute spray regime, although the larger droplets are fewer in count, they contribute to the major portion of the spray mass as this scales with the cube of droplet diameter. For example, the volumetric contribution of a single droplet of $d = 1000\ \mu m$ is equivalent to 10^6 times of small droplets of size $d = 10\ \mu m$. Because of this fact, the mean droplet diameter by mass is significantly larger than the mean particle diameter (as seen in [48]). Moreover, the overall evaporation behavior of the large droplet is different from the small droplets. For example, experimental study by Verwey and Birouk [110] showed that the evaporation of small droplets or the droplets of a size approaching the Kolmogorov length scale stay unaffected by the presence of turbulence in a zero mean velocity flow. However, the evaporation of the large droplets is enhanced by the turbulent environment even in zero mean velocity. Furthermore, based on the fundamental d^2 law [108], large droplets evaporate faster than smaller droplets due to proportionality between the total evaporation rate and the size of droplet. Hence, the presence of higher fuel-vapor in the vicinity of these droplets, they become the rate limiter for combustion [22]. Therefore an improved understanding of these droplets is important.

Essentially with greater simplifications, a broad level of understanding about evaporation and combustion of isolated droplets have been developed. Experimental studies such as [23, 26, 41, 44, 46, 62] cover the droplet evaporation under various ambient conditions. Even with a wealth of results available in this regime, the intricate small-scale dynamics of the flow still remains unknown. As highlighted in the reviews by Jenny et al. [38], Masri [58], the scalar flow field (i.e. the temperature, vapor-mixture mass fraction field) is a challenging task from the experiment point of view. Besides these two scalar fields, non-spherical droplet shapes are observed during many of the experiments such as [9, 27, 34, 88]. However, the influence of droplet shape was never focus of those studies. The analytical and numerical approach can help in gaining insights about these small-scale dynamics. Some noteworthy studies using analytical approach [3, 47, 105, 106] and numerical approach [32, 90, 115] demonstrate the potential of exploring this domain in further detail. The subsequent chapters will provide a comprehensive discussion of the existing literature relevant to different problem statements covered under this dissertation.

In a broader context, the numerical approaches to solve multiphase flows can be categorized as Eulerian-Eulerian, Eulerian-Lagrangian and Fully-resolved simulations. In case of dispersed flows, the first two categories consider the droplets as point-sources, therefore not reesolving the internal flow. A detailed discussion on the numerical approaches for solving multiphase flows is covered in Chapter 2. Out of these numerical approaches, Direct Numerical Simulation (DNS) is based on fully-resolved approach. DNS involves solving the dynamics of flow using first principles i.e. conservation of mass, momentum and energy. This means that DNS can resolve all the spatial and temporal scales of the flow, capturing all the small-scale details without relying on assumptions or turbulence models. As described by Sirignano [98], a true direct numerical simulation approach which can resolve both liquid and gas phases with distinct liquid-gas interface can be helpful in simulating these type of flows. Such frameworks based on different methods for fully-resolved simulations have been developed recently [63, 69, 86, 89].We are utilizing a framework based on Interface-capturing approach using Volume of Fluid method for phase-changing flows [69] in this work. Chapter 2 covers the details about it.

1.2 Scope and Organization of the Dissertation

With the emphasis on large droplets, this dissertation focuses on the study of droplet evaporation and its combustion in various ambient gas environment using direct numerical simulation. Due to the presence of convective flow conditions inside the combustion chamber [16, 79], an imbalance of inertial forces and surface tension exists. This can be characterized using a non-dimensional number called "Weber number" [54], defined as

$$We = \frac{\rho_G U_{rel}^2 d_0}{\sigma} \tag{1.1}$$

For a fixed Reynolds number (ratio of inertial force to viscous force $Re = \frac{\rho_G U_{rel} d_0}{\mu_G}$), small droplets will have higher surface tension due to higher curvature and small Weber numbers. Hence, they tend to remain in a nearly spherical shape. However, the larger droplets will have a higher Weber number making them more susceptible to deformation from spherical to non-spherical shape [57]. As mentioned previously, such deformed (ellipsoidal) shapes were observed during experiments but the explicit effect of shape change was not accounted, considering the droplet to be a spherical "non-deforming" particle [41, 44, 76]. Therefore, it can be hypothesized that the normalized area of deformed droplet (A_d/A_0) depends on $We,\ Re$.

$$\frac{A_d}{A_0} = f(We, Re) \tag{1.2}$$

Here, A_0 is the initial surface area of the droplet.

Considering the droplet shape to be spherical throughout its lifetime, a traditional heat-transfer model for quasi-steady droplet evaporation [3] can be written as follows,

$$Nu = f(Re, Pr, B) \tag{1.3}$$

Here, Nusselt number Nu, Prandtl number $Pr = \mu_G \, c_{PG}/k_G$ is and Spalding heat transfer number $B = c_{PG}(T_\infty - T_\Gamma)/h_{fg}$.

In general, the geometrical features of the object immersed in ambient flow impact the flow development around it [101, 102, 113]. This, in turn, alters the momentum transfer between the object and ambient flow, affecting the boundary layer development. This highlights the importance of considering the object's shape when analyzing flow dynamics in a broader context. Intuitively, this phenomenon carries a greater importance and increased complexity in case of evaporating/combusting droplets. The existence of temperature and fuel-vapor gradients between the cold droplet and hot ambient air involves both heat and mass transfer. Therefore, based on this knowledge, it is hypothesized that the droplet deformation will have a relationship with heat and mass transfer. It can be written in the following form,

$$Nu = f(Re, Pr, B, We) \tag{1.4}$$

To test this hypothesis at first, we study the evaporation of a deformable droplet under various convective inflow conditions. These inflow conditions are generally described by inlet velocity profile (uniform or non-uniform flow) and its magnitude [5] along with the thermophysical properties such as pressure and temperature. The impact of inlet velocity magnitude and thermophysical conditions on the evaporation of non-deformable droplet is well understood both theoretically and experimentally. Many of the experimental studies on the droplet evaporation consider the droplet to be of spherical shape for its entire lifetime [83, 119]. Hence, such interaction of droplet deformation and inlet flow has not been explored for the evaporation problem yet. Therefore, to quantify the effect of droplet shape on its evaporation, a detailed DNS study is performed and covered under Chapter 4.

The second objective is to investigate the evaporation of deformable droplets under natural convection. The presence of temperature gradient between hot (evaporating) droplet and cold ambient air generates a natural convection current due to variable buoyant forces. Moreover, the strength of this buoyancy driven flow can be enhanced by the gravity field. The impact of natural convection is generally ignored when the droplets are exposed to flow with forced convection [88]. However, in the absence of forced convection, such flow development around the droplet can have significant impact on the droplet evaporation time [12, 31, 111]. Therefore, Chapter 5 investigates the droplet evaporation under buoyancy driven flows.

The third objective of this work is to extend the effect of droplet shape on its combustion. The motivation here is to analyze the complex relationship between change in evaporation rate due to droplet deformation and its effect on the combustion parameters such as flame shapes and their area evolution. This is covered under Chapter 6.

To fulfill these objectives, a numerical framework built upon an in-house code is utilized. The details of this framework along with a general approach to solve multiphase flows is covered under Chapter 2. Furthermore, to minimize the droplet movement, a non-intrusive method to suspend the droplet is developed under this work which is discussed in Chapter 3. The results from these fully-resolved simulations can contribute towards an improved understanding of the small-scale combustion dynamics. This understanding is hoped to be utilized for enhancement of existing numerical models for droplet evaporation and combustion.

Chapter 2

Numerical Framework

2.1 Introduction

Before diving into the details of numerical framework used in this work, a brief discussion on multiphase flows and the existing numerical approaches are discussed here. The intent here is to present a short and overall review about approaches to solve the multiphase flows.

2.1.1 Multiphase Flows and their Applications

As the name suggests, a multiphase flow involves more than one phase in a system. These phases can be both thermodynamically and fluid-dynamically different. Multiphase flows are omnipresent and observed in our daily lives such as water-air flow over the ocean surface, rain drops in air, sediment transport in river and many more. General industrial applications of multiphase flows are bubble column reactors, fluidized beds, stirred tank reactor, humidification devices, sprays in combustion, soot formation from the exhaust to name a few. Depending upon on the type of phases, the multiphase flows can be categorized as gas-liquid, liquid-liquid, gas-solid or three-phase. Classic two-phase system is shown in Fig. 2.1 and this pictorial representation is adapted from Sommerfeld [99]. This two-phase system can be classified as transition flow shown in (a), stratified/separated flow shown in (b), dispersed flow shown in (c).

One of the complexities of multiphase flows is the presence of various regimes of the same

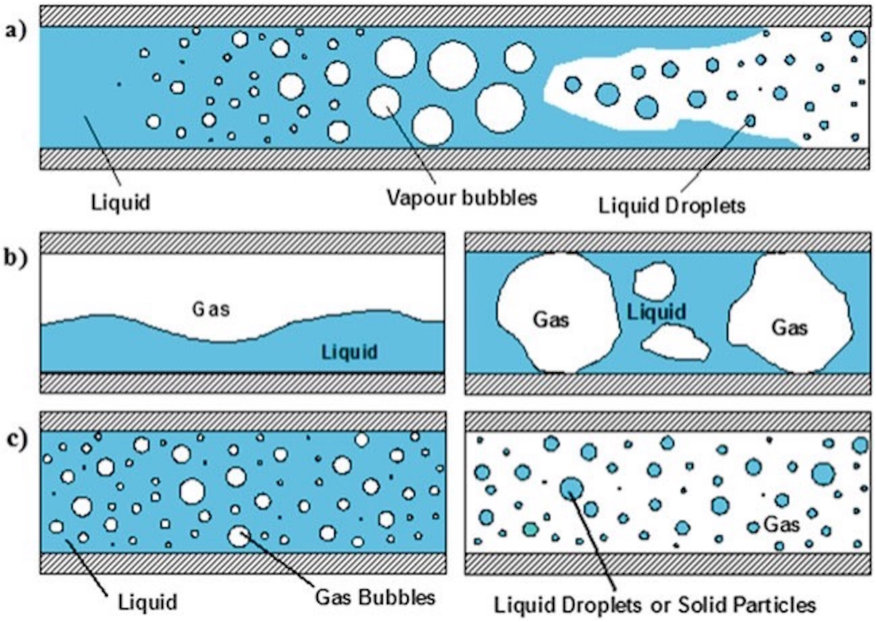

Figure 2.1: Different regimes of multiphase flow [99]

two phases at different conditions. For example: In oil-industry application, the two phase oil-water flow in a vertical pipe can go into various regimes depending upon the relative velocities between these phases. These regime are, dispersed water bubbles in oil flow, plug flow where big stretched water bubble is build and travel across the pipe, the chaotic churned flow, the annular flow flow where water displaces the oil in the core region and oil is near the wall [30]. This is one of the well known examples of multiphase flows to demonstrate the inherent complexities in solving such flows.

2.1.2 Challenges in Multiphase Flows

From the computational point of view the system equations need be solved in all phases in contrast to single-phase flow. Moreover, due to the presence of multiple phases, the phase-interaction at the interfaces need to be accounted accurately. In the above given example of oil-water flow in a vertical pipe, it is clear that the interface between two phases changes with time as well as with the flow conditions. Moreover, for a particular regime of flow, there is phase-interaction at the interface which needs attention in order to solve the system accurately [10]. In addition to this, such phase-interaction becomes further complex when phase-change is occurring. The combination of solving flow for various phases, tracking/resolving the interface and accounting for the phase-interaction makes these kind of flows difficult to solve numerically [87].

2.1.3 Dispersed Flows

As the focus of this dissertation is on isolated liquid droplet evaporation in gaseous environment, our discussion here is limited to dispersed flows. These type of flows involve a disperse phase such as bubbles/droplets/solid particles which are randomly scattered in a continuous phase such as air or water. Based on the inter-particle spacing and volume loading, dispersed flows can be identified as dilute dispersed flows or dense dispersed flows. Another way of categorizing such flows can be based on Stokes number which is a ratio of particle response timescale to flow timescale. One example of the dilute dispersed flow can be dilute spray regime in the combustion chamber where the liquid volume loading is less than 1%. Whereas, the dense dispersed flows are mostly seen in the application such as fluidized bed.

Methods to Solve Dispersed Flow

The approach to address the dispersed multiphase flows varies depending on the specific characteristics of the problem and the scale of analysis required. For instance, when studying a bubble column reactor, the focus may be on the macroscopic flow behavior at larger scales or on the dynamics of particles, including particle tracking, particle clustering, and particle wall-interactions. There are two most common approaches Eulerian-Eulerian (two-fluid) approach and Eulerian-Lagrangian approach to numerically solve these kind of problems.

Alternatively, the investigation can also zoom in on the finer details at the particle-scale (small-scale) level such as coalescence or breakup. In addition to this, the small-scale details for evaporating/burning droplets would also include the vapor-mass fraction and temperature field which are difficult to measure experimentally. Such type of investigations would require a Fully-resolved approach. Moreover, the findings from fully-resolved methods can be utilized to further refine the numerical models which RANS/LES based with point-mass particle assumption.

Eulerian-Eulerian Approach

This approach describes both the phases in Eulerian manner and assumes the two phases as interpenetrating continua. Therefore, it involves solving the fundamental equations in both phases in each computational cell based on their volume fraction. The phase-interaction due to mass, momentum and heat transfer between phases is accounted using source/sink terms in the governing equations for both phase. Hence, this method accounts for the two-way coupling between two phases. This method is relatively computationally expensive as it solves equations for both phases. The details of fundamental equations can be found in a review by Sommerfeld [99]. This approach can handle both continuous-continuous phase flows such as air-water, two immissible fluids (sloshing, filling of tank) and continuous-dispersed phase flows such as bubbles, solid, liquid drop-gas (sprays, air conditioning application water in air, sediment-transport sand-liquid water phase. The advantage of this approach over Eulerian-Lagrangian approach (discussed in Section 2.1.3 is that it can tackle the flows with large particle density. For the dispersed flows, the particles (both solid, bubbles/droplets) are still treated as point sources.

Eulerian-Lagrangian Approach

This approach is particularly applicable for low particle density dispersed flows where the particle response timescale is much smaller than the flow timescale. Typically, the carrier phase is solved using Eulerian approach and the motion of particles is solved using Lagrangian approach. The equations of motion such force balance accounting the mass of particles are used to track particles and their trajectories from the previously solved gas flow field. The source terms due to particle motion are evaluated using statistical averaging and accommodated in the momentum equation for continuous phase. Various methods are explained in a review paper by Sommerfeld [99]. Readers are redirected to it for more details.

Fully-Resolved (particle-resolving) Approach

A fully-resolved approach for deformable particles such as bubbles/droplets involves solving the flow field in both phases along with an interface tracking/capturing scheme. In contrast to Eulerian-Eulerian approach, the phases are not interpenetrating in this approach. A classification of approaches to resolve such flows is neatly described and compared in a review paper by S. Mirjalili et al. [87]. For the ease of explanation, we have redrawn figure 1 from [87] here with some modifications in it. The solid linestyle around the objects in Fig. 2.2 represents the focus of the discussion in this chapter. The dash linestyle objects are not covered in detail. The yellow color objects are approaches for diffuse interface capturing. The blue color code designates the sharp method of interface capturing. One of these methods is utilized in this work which will be discussed in Section 2.2.

In order to track or capture the interfaces (either sharply or diffusely), One-fluid formulation of two-phase flow modelling is the most common method [87, 99, 107]. This involves solving a single set of conservation equations for the entire domain including the interface as the conservation form of equations can handle discontinuity in the domain. To do so, first a function which can distinguish between two phases and the interface let's say $\phi(x,t)$ is required. Based on the value associated to this function, the phase regions (phase-1 and phase-2) are defined as,

$$\Gamma(t) = x|\phi(x,t) = a \tag{2.1a}$$

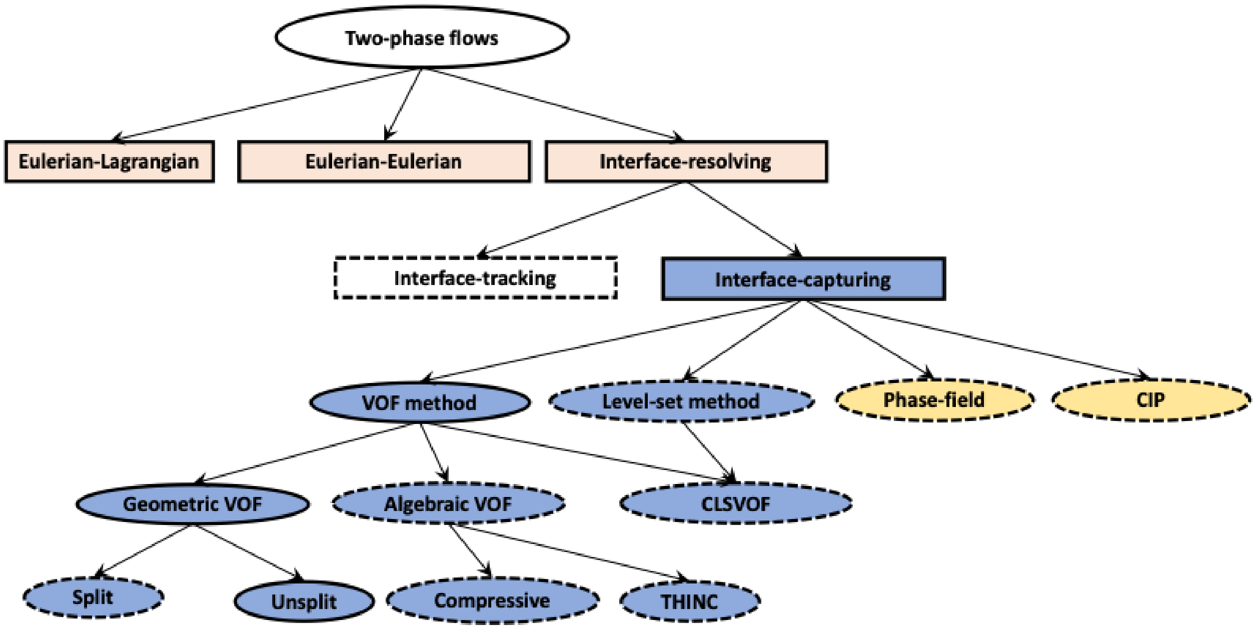

Figure 2.2: Classification of approaches to solve multiphase flows

$$\Omega_{phase-1}(t) = x|\phi(x,t) < a \tag{2.1b}$$

$$\Omega_{phase-2}(t) = x|\phi(x,t) > a \tag{2.1c}$$

A general momentum equation in conservative form can be written as,

$$\frac{\partial(\rho\boldsymbol{u})}{\partial t} + \nabla\cdot(\rho\boldsymbol{u}\otimes\boldsymbol{u}) = -\nabla p - \rho g + \nabla\cdot(\mu\boldsymbol{S}) + F_\sigma \tag{2.2}$$

Therefore, for the accurate interface capturing, the governing equations between phases are tied-up through local density ρ, viscosity μ and surface tension F_σ. The way local density and viscosity is computed defines whether the interface is sharp or not. Moreover, for the given Eq. (2.2), term F_σ is a source term which exists only at the interface. The remaining governing equations for the system can be written in the same fashion and can be found in [107].

Another critical requirement of the two-phase solver is to balance the forces at interface. For a deformable interface, a special attention is required to balance the surface tension force and pressure gradient across the interface. The surface tension force in Eq. (2.2) can be implemented as stress form in integral (surface) method or as a body force in volumetric method.

Out of these two, volumetric formulation of surface tension force is much more popular [75]. A well known Continuous Surface Force (CSF) formulation of surface tension force can be written as $F_{ST} = \sigma\kappa\delta_S\mathbf{n}$, here δ_S is a Dirac delta function specific to methods, σ is surface tension, $\mathbf{n}$ is normal vector and κ is curvature. One of the challenging task in implementing surface tension is computation of normal vector and curvature. Curvature is computed by taking the divergence of normal vector. Various techniques have been developed to compute these two accurately.

Interface tracking approach (also known as surface/integral method) marks the interface using interface grid and uses local fluid velocity for interface advection. The advantage of this method is accurate interface structure and sharpness. However, it can not easily handle changes in topology such as droplet collision or coalescence [99].

Instead of tracking the interface, Interface capturing approach (volume method) reconstruct the interface using a phase indicator function. For example: VOF method uses liquid volume fraction (α) and Levelset Method uses a levelset signed distance function (φ) to reconstruct the interface. Without phase change, a general interface transport equation for a indicator function f can be written as

$$\frac{\partial f}{\partial t} + \nabla \cdot (uf) = 0 \tag{2.3}$$

The reconstruction method and the transport of phase indicator function is different for VOF and level-set based methods. The pros and cons of these two approaches are well described under [87]. Therefore, not repeated here.

2.2 Current Numerical Framework

The objectives described under Section 1.2 are explored numerically using a finite volume based framework. This framework is built upon an in-house code NGA which is a low Mach number incompressible multiphase solver [18]. The framework uses interface-capturing Direct Numerical Simulation approach for evaporating (phase change) flows with large density ratios. The fundamental governing equations to describe this system are continuity, momentum, energy and species transport equations. These are described briefly in this section. The readers are referred to [69] for more details on methods and algorithms used in developing this framework. Subscripts L, G, V refer to liquid, gas and vapor phase respectively throughout this work.

2.2.1 Interface Capturing Method

The current framework uses Volume-of-Fluid (VOF) approach to capture the interface between liquid and gas phase. In this approach the liquid volume fraction (α) is defined in each cell as shown in Fig. 2.3. $\alpha = 0$ refers to a cell in gas phase and $\alpha = 1$ refers to cell in liquid phase. In case of a cells containing both liquid and gas phase, α ranges between 0 and 1. The interface location is identified based on this non-zero gradient. In the interface containing cells, the effective density (ρ^*) and effective viscosity (μ^*) is computed in a following manner.

$$\rho^* = \rho_G + (\rho_L - \rho_G)\alpha \tag{2.4a}$$

$$\mu^* = \mu_G + (\mu_L - \mu_G)\alpha \tag{2.4b}$$

The reconstruction and transport method for the interface is covered under Section 2.2.3. Using this approach, the gas and liquid velocity field is treated as single field. Therefore, the governing equations are solved only once for unified velocity field. It is worth highlighting here that the densities for both phases do not vary with time in this incompressible flow

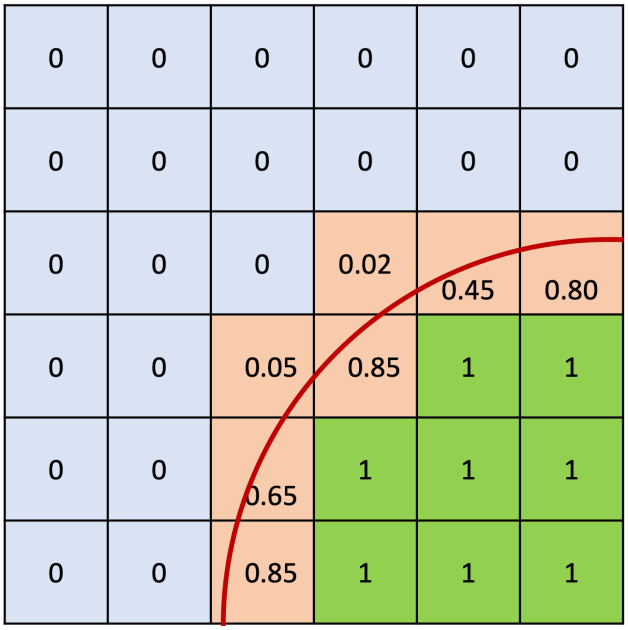

0	0	0	0	0	0
0	0	0	0	0	0
0	0	0	0.02	0.45	0.80
0	0	0.05	0.85	1	1
0	0	0.65	1	1	1
0	0	0.85	1	1	1

Figure 2.3: Concept of Volume-of-Fluid method

solver for the case of droplet evaporation in Chapter 4 and combustion in Chapter 6 under forced convection. However, to accommodate the density variation due to temperature gradients between gas and droplet in Chapter 5, these densities vary according to Bousinessq approximation which is explained under Section 5.2.2.

2.2.2 Conservation of Mass and Momentum

Using a single field approach, the momentum equation for both liquid and gas phase can be written as,

$$\frac{\partial\left(\rho\boldsymbol{u}\right)}{\partial t}+\nabla\cdot\left(\rho\boldsymbol{u}\otimes\boldsymbol{u}\right)=-\nabla p-\rho g+\nabla\cdot\left(\mu\boldsymbol{S}\right),\text{where}\tag{2.5a}$$

$$\boldsymbol{S}=\left(\nabla\boldsymbol{u}+\nabla\boldsymbol{u}^{\top}-\frac{2}{3}\nabla\cdot\boldsymbol{u}\right)\tag{2.5b}$$

Here, ρ and μ are the effective fluid density and effective dynamic viscosity; $\boldsymbol{u}$ is the velocity, p is pressure, g is gravitational acceleration vector and $\boldsymbol{S}$ is stress tensor.

The momentum equation in Eq. (2.5a) is tied up with continuity equation,

$$\nabla \cdot \boldsymbol{u} = 0 \tag{2.6}$$

The pressure is computed from the incompressibility constraint for the velocity field. It is solved using Pressure Poisson equation using Ghost Fluid Method (GFM) by Liu et al. [52].

2.2.3 Conservation of Scalars

As the droplet is evaporating with a receding liquid-gas interface, the transport of scalar quantities temperature, species mass fractions and the liquid volume fraction (α) is involved in this problem. To represent the temperature field sharply, a two-field approach by Ma and Bothe [55] is implemented. For low-Mach number flows, neglecting the viscous work, the conservation of energy in the liquid phase can be written as,

$$\frac{\partial(\rho_L\ c_{p,L}\ T_L)}{\partial t} + \nabla \cdot (\rho_L\ c_{p,L}\ T_L\ \boldsymbol{u}) = \nabla \cdot (\rho_L\ c_{p,L}\lambda_L \nabla T_L) \tag{2.7}$$

Here $\lambda_L = \ k_L/(\rho_L\ c_{p,L})$, known as thermal diffusivity.

Similarly, the gas phase energy equation can be written as,

$$\frac{\partial(\rho_G\ c_{p,G}\ T_G)}{\partial t} + \nabla \cdot (\rho_G\ c_{p,G}\ T_G\ \boldsymbol{u}) = \nabla \cdot (k_G \nabla T_G) + \dot{\omega}_T \tag{2.8}$$

Here $\lambda_G = \ k_G/(\rho_L\ c_{p,G})$, known as thermal diffusivity of gas, $\dot{\omega}_T$ is the heat source term due to combustion. This term is zero when the droplet evaporation is taking place in a non-reactive environment.

The chemical species transport is only solved in the gas phase. This can be described as,

$$\frac{\partial(\rho Y_i)}{\partial t} + \nabla \cdot (\rho Y_i \boldsymbol{u}) = \nabla.(\rho D\ \nabla Y_i) + \dot{\omega}_i \tag{2.9}$$

Here Y_i is "i" species mass fraction, D is diffusivity in air and $\dot{\omega}_i$ is the chemical source term for each species. For droplet evaporation related problems, the fuel droplet is a non-reactive single component jet fuel surrogate. Therefore, $\dot{\omega}_i$ is zero and only one species (Y_F) will be solved. The species mass fraction of inert air will be computed using $Y_{air} = 1 - Y_F$. However, for combustion related problems, depending upon the combustion mechanism, $n+1$ number of species will exist where n is number of active species in gas phase, N_2 is a non-reactive inert species. This is further explained under Section 6.2.2.

In case of receding interface, for constant thermophysical properties, the transport equation for liquid volume fraction (α) is given by

$$\frac{\partial \alpha}{\partial t} + \left(\boldsymbol{u}_L + \frac{\dot{m}''}{\rho_L}\boldsymbol{n}_{\boldsymbol{\Gamma}}\right) \cdot \nabla \alpha = 0 \tag{2.10}$$

Here, $\boldsymbol{u}_L$ is extrapolated liquid velocity, $\frac{\dot{m}''}{\rho_L}\boldsymbol{n}_{\boldsymbol{\Gamma}}$ is the interface recession velocity and combined $\left(\boldsymbol{u}_L + \frac{\dot{m}''}{\rho_L}\boldsymbol{n}_{\boldsymbol{\Gamma}}\right)$ is seen by the VOF solver [65]. As mentioned previously, the liquid mass fraction α is defined such that it is 1 in a purely liquid cell and 0 in a purely gas cell. The interface is formed sharply where a non-zero gradient of α is found. To reconstruct the interface, this framework uses Piecewise Linear Interface Calculation (PLIC) in which interface is approximated as a line in 2-D or a plane in 3-D. To compute the interface normal vectors, a second-order accurate Efficient Least-square VOF Interface Reconstruction Algorithm (ELVIRA) is used Pilliod and Puckett [73]. Interface curvature κ is computed using a quadratic least square fit on reconstructed level-set from the VOF field. For the advection of the interface, an unsplit method under geometric VOF is used. In this method, the second term in Eq. (2.10) is transported in a single timestep without splitting the advection operator in each spatial direction [56]. The readers are referred to [63, 69] for more details of numerical algorithms used for interface reconstruction.

Here, $\dot{m}''$ is local evaporation flux satisfies the following equation,

$$\frac{\mathrm{d}}{\mathrm{d}t}\int_{L}\rho_L dV = -\int_{\Gamma}\dot{m}'' dS \tag{2.11}$$

Here, subscripts Γ is referred to variables measured at interface.

2.2.4 Matching Conditions

To ensure the adherence to conservation of mass in both phases, the jump condition for mass at liquid-gas interface can be written as,

$$[\boldsymbol{n}.\boldsymbol{u}]_{\Gamma} = \dot{m}''\left[\frac{1}{\rho}\right]_{\Gamma} \tag{2.12}$$

Here the bracket notation is used for the jump across the interface specified as $[\phi]_{\Gamma} = \phi_G - \phi_L$.

Similarly, the jump condition for momentum is

$$[p]_{\Gamma} = -\sigma\kappa - \dot{m}''^2\left[\frac{1}{\rho}\right]_{\Gamma} \tag{2.13}$$

where σ is surface tension and κ is local curvature of the interface and is positive when the liquid is locally convex. The details of implementation of Ghost Fluid Method for matching conditions is given in [69].

As the evaporation is taking place, the thermodynamic equilibrium at the interface due to heat and mass transfer is maintained using the Clausius-Clapeyron relation Eq. (2.14a) and

Eq. (2.14b).

$$X_{F,\Gamma} = exp\left(\frac{-h_{fg}W_v}{R}\left[\frac{1}{T_\Gamma} - \frac{1}{T_{sat}}\right]\right) \tag{2.14a}$$

$$Y_{F,\Gamma} = \frac{XW_v}{XW_v + (1-X)W_G} \tag{2.14b}$$

Here, h_{fg} is latent heat of vaporization, W_v and W_G molecular weight of fuel-vapor and gas, T_Γ is interface temperature and T_{sat} is a constant saturation temperature for given ambient conditions.

To balance the energy transfer by conduction and diffusion of fuel-vapor at interface, the energy equation and species transport must simultaneously satisfy the following conditions across the interface,

$$\dot{m}'' = \frac{[\boldsymbol{n}_\Gamma \cdot k\nabla T]_\Gamma}{h_{fg}} \tag{2.15}$$

$$\dot{m}'' = \frac{[\boldsymbol{n}_\Gamma \cdot \rho_G \; D\nabla Y_F]_\Gamma}{Y_{F,\Gamma} - 1} \tag{2.16}$$

For a given evaporation flux ($\dot{m}''$), Eq. (2.14), Eq. (2.15) and Eq. (2.16) must be satisfied simultaneously. Therefore, vapor mass-fraction and interface temperature are dependent on each other and must be solved in an iterative manner.

This completes the description of system in the form of governing equations. The next step from this point is to use this framework for the numerical analysis of various flow problems. The additional set of equations (if any) will be discussed in their respective chapters.

Chapter 3

Development of Numerical Method to Study Droplet Evaporation

The work covered in this chapter was part of the following conference publications,

1. Meha Setiya and John Palmore Jr., Method to study effect of straining flow on droplet vaporization at low Reynolds number. Spring Technical Meeting Eastern States Section of the Combustion Institute, March 2020 [92].
2. Meha Setiya and John Palmore Jr., Effect of straining flow and droplet shape on vaporization rate of liquid fuel droplet. APS Division of Fluid Dynamics Meeting, January 2020 [93].

3.1 Introduction

In a general sense, the focus of this thesis work is to study the small-scale dynamics of an isolated droplet. Due to the flow development in the domain, the droplet will have tendency to to move from its original position if no suspension or motion restriction technique is applied on it. Various methods have been devised to keep it at a predetermined location. For example: most of the experimental studies restrict the droplet motion by suspending it either by a ring or using cross-fibers [20, 61, 76, 110], such that it stays at a fixed location for any given flow condition (Forced or Free convection). However, this additional fiber at the centre of droplet can affect the flow field within the droplet as well as outside it. Moreover, although this fiber material is nearly thermally insulated, such droplet suspension method can affect the heat transfer to the droplet [14]. This leads to shorter droplet decay time for droplet due to additional heat from fiber to droplet. To avoid this problem in our numerical analysis, a numerical method for non-intrusive droplet suspension is developed which is discussed in detail in Section 3.2 along with its testing on various flow conditions.

3.2 Gravity Update Method

An initial method to minimize the droplet motion with a non-intrusive technique was developed by Palmore Jr and Desjardins [68]. This method mimics the flow over droplet as falling with its terminal velocity (U_T). Therefore, no acceleration is experienced by the droplet. In the coordinate system moving with the droplet movement, the droplet appears stationary while the air flows around it at its terminal velocity (U_T). As time increases, due to droplet deformation, the internal flow and evaporation, the drag force changes. In literature, the drag correlations used to predict U_T for spheres show a few percent accuracy [17] in prediction. Ultimately, the change in drag leads to change in terminal velocity. Therefore, inflow velocity needs to be modified with time to keep the droplet at its fixed position. For the reader's convenience, this method is called “Inflow velocity update”. As the modified inflow velocity is an output of this method, the results using this method show that the achieved inflow velocity is usually lower than the targeted velocity based on the Reynolds number. Therefore, there is less control over the magnitude of inflow velocity.

In order to have better control over the inflow velocity (therefore on Inlet Reynolds number) a robust method for inflow boundary condition is required. To do so, we have developed an alternative approach which is embedded in the numerical framework described in Chapter 2. This approach updates the applied gravity on the droplet with time instead of updating the inflow velocity. This will be called “gravity update method”. The details of the current method are as follows,

As the droplet is falling with its terminal velocity ($U_T = U_{in}$), the force balance of gravitational, drag, and buoyancy force on the droplet can be written as,

$$(\rho_L - \rho_G)\ \forall\ g = \frac{1}{2}\ C_d\ \rho_G\ U_{in}^2\ A \tag{3.1}$$

Here $\forall$ and A are liquid volume and surface area of the droplet respectively.

From the definition of Reynolds number based on initial diameter d_0, the inflow velocity is calculated as,

$$U_{in} = \frac{Re\ \mu_G}{\rho_G\ d_0} \tag{3.2}$$

As the inflow velocity U_{in} needs to be constant, to balance the changing drag force due to change in drag coefficient (C_d), the gravity needs to be altered in all three directions at every timestep using a feedback controlled expression. Gravity in x-direction at $(n+1)^{th}$ timestep is modified as

$$g_x^{n+1} = g_x^n - \alpha \left[\frac{U_{drop}}{\tau_p} + \frac{\beta(x_{drop}^{n+1} - x_{init}^0)}{\tau_p^2} \right] \tag{3.3}$$

Here U_{drop} is the droplet velocity in the direction of gravity, x_{init}^0 is initial x-coordinate of droplet centre, x_{drop}^{n+1} is x-coordinate of droplet centre at $(n+1)^{th}$ timestep, τ_p is particle response time, α and β are arbitrary constants.

The update in applied gravity is designed such a way that the droplet remains at x_{init}^0 all the time. It is done by adjusting the gravity using the correction formula which is second term on the right hand side in Eq. (3.3). The first contributor in gravity correction is acceleration of droplet due to its velocity U_{drop}. This acceleration depends on particle response time τ_p. As the surface tension force governs the flow physics, τ_p is set to be multiples of capillary time scale [100] which is defined as,

$$\tau_p = \sqrt{\frac{\rho_L + \rho_G}{\sigma}} \left(\frac{d}{2\pi} \right)^{3/2} \tag{3.4}$$

The second contributor in gravity correction is acceleration of droplet center with respect to its initial location. Eq. (3.3) is implemented in all three directions in the same fashion.

3.2.1 Tests for Droplet Motion Under Planar Flow

Numerical Setup

This method is initially tested on a 2-D droplet of n-decane evaporating under $Re = 20$ with $\beta = 0$. The domain size ($L_x \times L_y$) for this study is ($30\ d_0 \times 40\ d_0$) where the initial droplet diameter $d_0 = 1 \times 10^{-4}\ m$ and it is initially located at $(-5d_0, 0)$ to the left of center of the domain as shown in Fig. 3.1. A fixed inflow boundary condition is applied on the left edge of the domain. The right edge is used as a convective outflow. The remaining boundaries in y and z directions are treated as periodic. A structured grid with $N_x \times N_y = 576 \times 768$

selected for this study. The gas and liquid fluids properties used in this analysis are listed in Table 3.1. These properties are taken at atmospheric pressure $P_\infty = 1\ atm$ and temperature 447.3K (boiling temperature of fuel) [1]. It is important to highlight that these properties of fluids are constant and do not change over time.

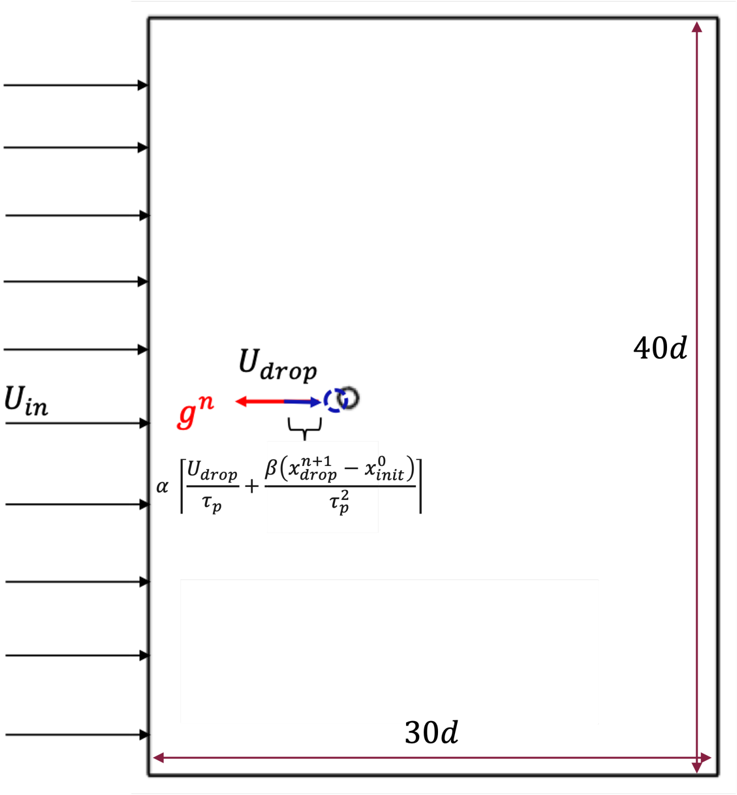

Figure 3.1: Numerical setup for testing of gravity update method

Property	Units	Gas	Liquid
Density ρ	kg/m^3	0.789	603.8
Viscosity μ	$kg/(m \cdot s)$	2.47×10^{-5}	1.92×10^{-4}
Specific heat c_P	$J/(kg \cdot K)$	1020.21	2812.10
Thermal conductivity k	$W/(m \cdot K)$	0.037	0.094
Surface tension σ	N/m	—	0.010
Latent heat of vaporization L_v	J/kg	—	2.763×10^5
Boiling temperature T_{boil}	K	—	447.3

Table 3.1: Fluid properties at the boiling temperature of fuel

Results

As the focus of this section is on the droplet motion, to quantify the change in droplet location with time, Fig. 3.2 shows the history of droplet centre x-coordinate with normalized time with varying α values. The smallest change over the time was observed for $\alpha = 0.5$.

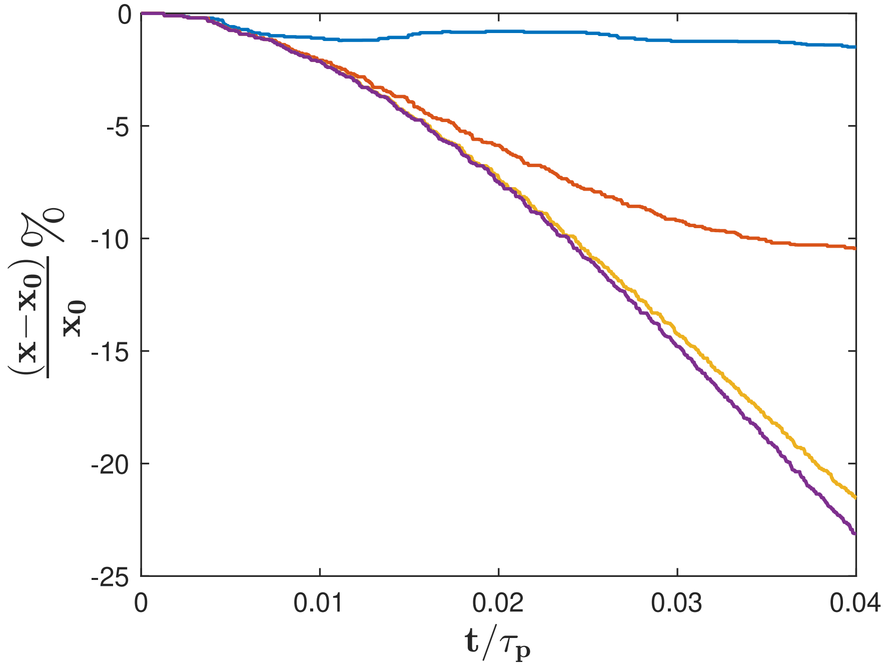

Figure 3.2: 2-D test: time history of % shift in x-location of droplet center when $\beta = 0$, $\alpha = 0.5$ (*blue*), 0.05 (*orange*), 0.005 (*yellow*), 0.0005 (*purple*)

To test this method further in 3-D case, the same numerical set-up as described previously is extended in 3-D. The smallest movement of droplet was observed in case of $\alpha = 0.5$ and $\beta = 0.05$. These values were found by trial and error method. Figure (3.3) shows the % shift in droplet motion with non-dimensional time in x,y, and z direction for two β values. $\alpha = 0.5$ is constant in the shown results which was a learning from previous 2-D studies [92]. Time is normalized using τ_p. As the time progresses, higher droplet movement is observed with higher value of $\beta = 0.5$. Moreover, the % shift in location is above 5% for the same after $t/\tau_p = 3$. Hence, $\beta = 0.05$ is finalized for the 3-D studies. Based on these results,

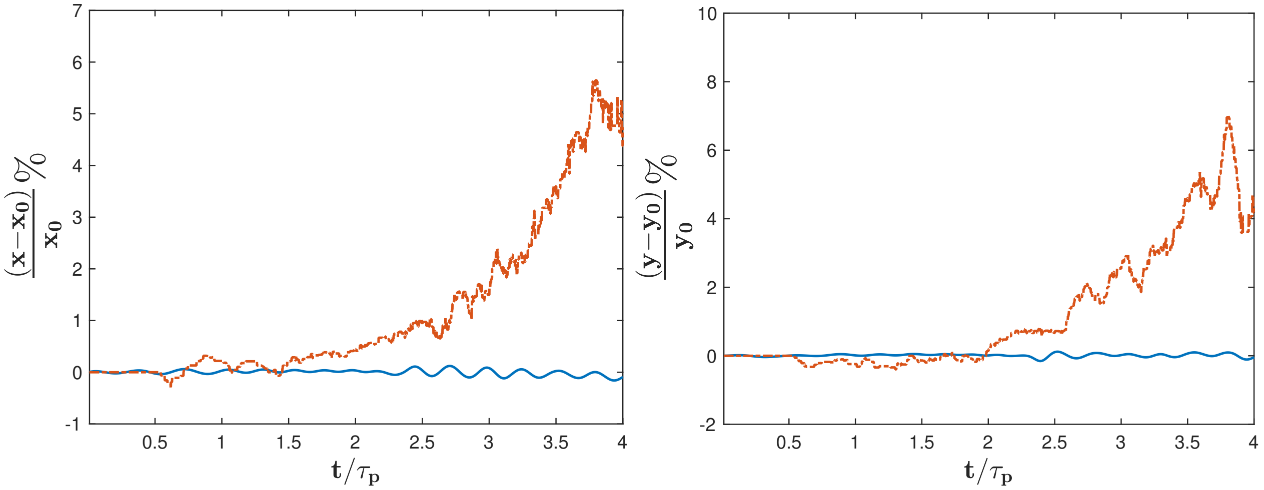

(a) % shift in x-location

(b) % shift in y-location

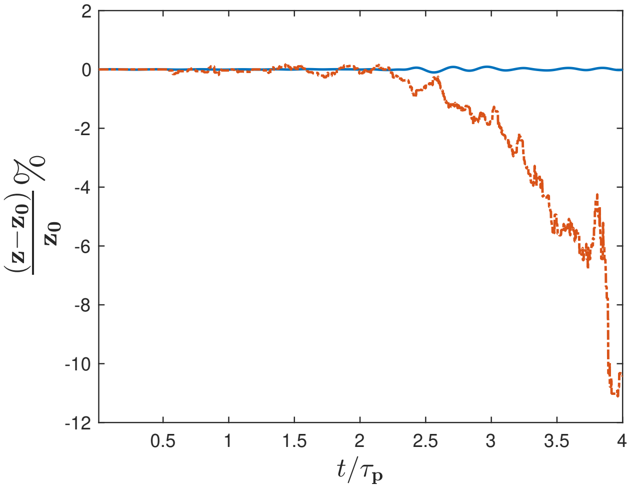

(c) % shift in z-location

Figure 3.3: 3-D test: time history of droplet movement
orange dash line marks $\beta = 0.5$ *and solid blue line marks* $\beta = 0.05$

this numerical method with $\alpha = 0.5$ and $\beta = 0.05$ has been utilized to effectively control the droplet motion for all our 3-D studies presented under upcoming chapters.

3.3 Effect of Straining Flow on Droplet Evaporation

To further test this numerical method, the droplet evaporation under non-planar convective flow is studied. Therefore, this section examines the droplet motion and effect of flow strain on the evaporation rate at $Re = 20$ [101]. Inspired from studies by [5, 6], a relative comparison between the evaporation of droplet under planar flow vs straining flow in presented in this section.

Analytical Method

To identify the appropriate flow conditions for this problem, the dimensional analysis is performed. For the sake of simplicity, the deformed droplet can theoretically be considered an ellipsoid in this problem. Hence, area of an ellipsoidal droplet will be dependent on incoming air properties and liquid fuel properties. This can be written as follows,

$$A_d = f\big(A_0,\ U_{in},\ Sd,\ \rho_G,\ \rho_L,\ \mu_G,\ \mu_L,\ \sigma\big) \tag{3.5}$$

Here, A_0 is total surface area of initially spherical droplet, U_{in} is inflow mean velocity, S is strain rate, ρ_G and ρ_L density of gas and liquid phase respectively, μ_G and μ_L dynamic viscosity of gas and liquid phase respectively, σ is surface tension of liquid.

The selected independent variables for this analysis are ρ_G, Sd and A_0. Using the non-dimensional analysis for this problem, the non-dimensional terms (π-terms) can be written,

$$\frac{A_d}{A_0} = f\left(\frac{U_{in}}{Sd},\ \frac{\sigma}{\rho_G\ (Sd)^2\ \sqrt{A_0}},\ \frac{\rho_L}{\rho_G},\ \frac{\mu_G}{\rho_G\ Sd\ \sqrt{A_0}},\ \ \frac{\mu_L}{\rho_G\ Sd\ \sqrt{A_0}}\right) \tag{3.6}$$

Eq. (3.6) includes the π-terms, area ratio (ratio of area of ellipsoid and sphere), strain velocity ratio, Weber number based on strain velocity, density ratio, Reynolds number based on strain velocity respectively. We note that $\sqrt{A_0} \sim d$, therefore we can write the Re_{strain} as,

$$Re_{strain} = \frac{\rho_G\ S\ d^2}{\mu_G} \tag{3.7}$$

The inflow velocity varying in y-direction for the given strain rate can be written as,

$$U(y) = U_{in} + S\ y \tag{3.8}$$

As Kolmogorov theory states that many relevant turbulent statistics can be described using only ν_g and ϵ [40]. Accordingly a characteristic velocity gradient scale (which represents the strain rate) can be defined,

$$S = \left(\frac{\epsilon}{\nu_g}\right)^{\frac{1}{2}} \tag{3.9}$$

This can be expressed in terms of Kolmogorov length scale as follows,

$$S = \left(\frac{\nu}{\eta^2}\right) \tag{3.10}$$

Where Kolmogorov length scale η can be written as,

$$\eta = \left(\frac{\nu^3}{\epsilon}\right)^{\frac{1}{4}} \tag{3.11}$$

Numerical Setup

The test configuration for this analysis is same as shown in Fig. 3.1. Besides the other boundary conditions, the inlet flow profile needs to be determined a priori. A linearly increasing velocity in y-direction with a particular strain rate is chosen for this work. As demonstrated in Eq. (3.10) the strain rate S depends on Kolmogrov scale length η. In sprays, the largest droplets are of the same order of magnitude as the Kolmogorov length scale [109]. Therefore, η can be assumed to be a multiple of d_0. Hence, the ratio of $\eta/d_0 = \sqrt{2}$ is considered for this study such that $(\eta/d_0)^2 = 2$. This leads to strain rate value $S = 1500\ 1/s$.

Results

To evaluate the effect of ambient flow field on the evaporation rate of the droplet, the variation of Nusselt number with time for uniform flow and straining flow are compared in Fig. 3.4. The time history of Nusselt numbers depicts that the evaporation rate is higher for flow with strain case (orange) [92]. Although, the evaporation rate is fluctuating for each flow type, a consistent higher value for staining flow is observed. These fluctuations could be due to the simplified reduced 2-D geometry of the droplet. This can be further explained by the difference in velocity field. The pseudocolor of velocity field in Fig. 3.5 show that the due to presence of strain in the incoming flow leads to asymmetry of flow around the droplet. Such velocity gradient causes higher shear stresses on the droplet, therefore higher velocity at the top surface than the velocity at the bottom of the droplet. Moreover, the flow behind the droplet forms a skewed wake region. This leads to higher gradient of temperature near the droplet, hence higher evaporation rates.

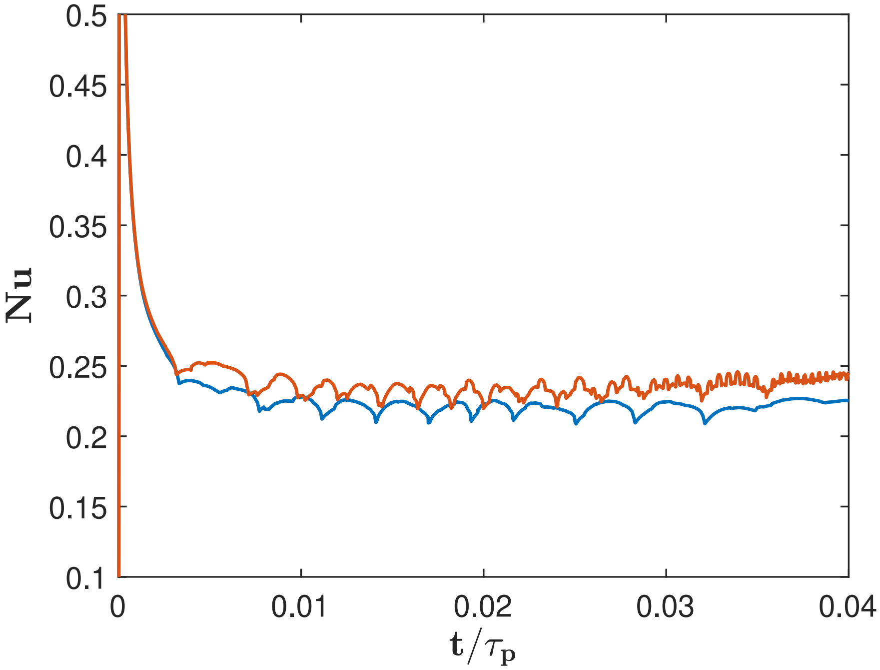

Figure 3.4: 2-D: Nusselt number vs normalized time (t/τ_p) for uniform flow(*blue*) vs straining flow(*red*)

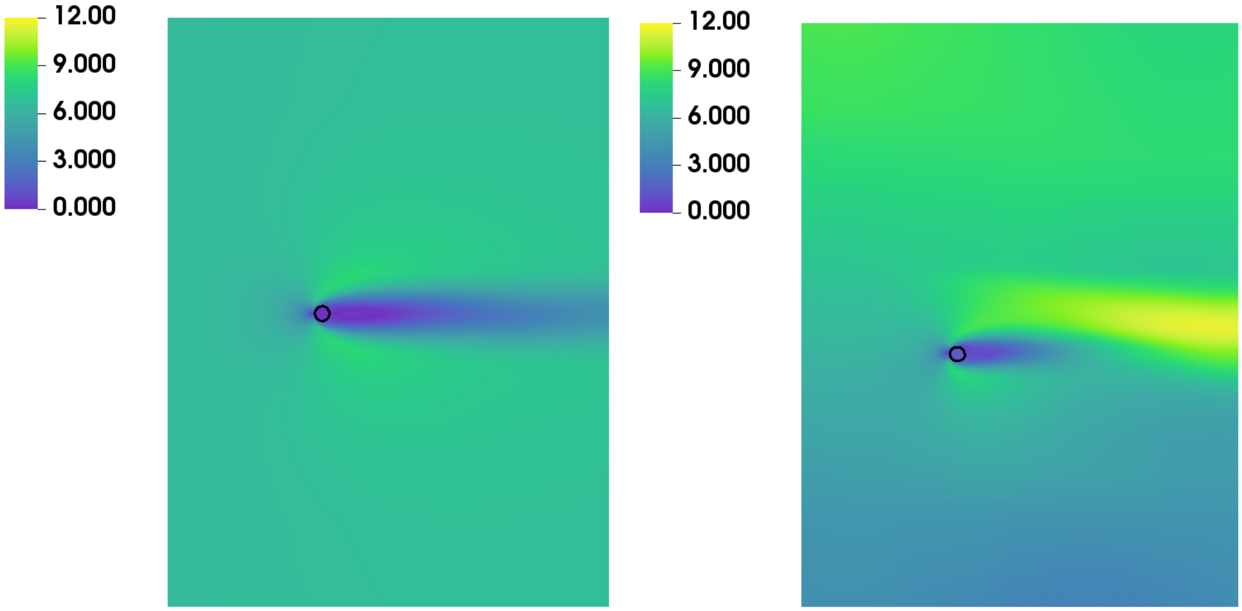

(a) Velocity field for uniform flow (b) Velocity field for straining flow

Figure 3.5: Pseudocolor of the velocity field at $t = 6 \times 10^{-4} s$

3.4 Conclusions

This chapter covered the development of a non-intrusive method to stabilize the droplet at its predetermined location throughout its evaporation lifetime. The need of this method was realized due to significant motion of the droplet while it is exposed to convective flow conditions. This method named as “gravity-update method” mimics the flow over droplet which is falling at its terminal velocity. To restrict the motion of droplet, it updates the applied gravity in a feedback loop manner. The feedback loop requires appropriate value of two coefficients α and β to drive the update in gravity correctly. After a thorough testing of this method, the least change in droplet center is found when the two coefficients are $\alpha = 0.5$ and $\beta = 0.05$. These coefficients are used for the upcoming studies.

Post development of this method, a preliminary 2-D study demonstrates the effect of inlet flow profile on the evaporation rate of the droplet. Due to presence of the linear strain in the inlet flow, higher shear stresses are imparted by the ambient air on the droplet. Moreover, due to skewed flow around the droplet, higher velocities and favorable temperature gradients are generated. This results in higher evaporation rate in case of straining flow when compared to planar flow.

Chapter 4

Evaporation of Deformable Droplet Under Forced Convection

The work discussed in this chapter was published as a peer-reviewed journal article. The details of article are as follows,

- Meha Setiya and John Palmore Jr. Quasi-steady evaporation of deformable liquid fuel droplets. International Journal of Multiphase Flow, Volume 164, 2023. doi:10.1016/j.ijmultiphaseflow.2023.104455 [95].

4.1 Introduction

With an emphasis on large droplets, this work focuses on analyzing the effect of droplet shapes on their evaporation. As mentioned in Section 1.1, the droplet size in the spray varies from a few microns to hundreds of microns [48, 98]. Within the spray, the overall evaporation behavior of the large droplets is different from the small droplets. For example, experimental studies such as [110] showed that the evaporation of small droplets or the droplets of a size approaching the Kolmogorov length scale stay unaffected by the presence of turbulence in a zero mean velocity flow. However, the evaporation of the large droplets is enhanced by the turbulent environment even in zero mean velocity. Moreover, in real sprays, although the larger droplets are fewer in the count, their volume fraction contributes to the majority of the spray volume. This is because the volume of a droplet is proportional to the cube of its diameter. Therefore, the droplet size plays an important role in the atomization process and further in combustion [48].

Due to the presence of turbulent and convective flow conditions inside combustion chamber [16, 79], an imbalance of inertial and surface tension exists. Hence, droplets can deform from a spherical shape to a non-spherical shape [57]. This deformation can be characterized by a non-dimensional number called "Weber number" [54] defined as,

$$We = \frac{\rho_G U_{rel}^2 d_0}{\sigma} \tag{4.1}$$

Here, ρ_G is gas density, $U_{rel} = (U_{in} - U_{droplet})$ is the relative gas velocity with respect to droplet velocity, d_0 is the initial diameter of the droplet and σ is the surface tension of the liquid droplet. As Weber number governs the droplet shape, small Weber numbers ($We < 1$) lead to nearly spherical shapes. Whereas, large Weber numbers lead to more deformed shapes. Therefore, for the same liquid properties, small droplets will have lower

Weber numbers, hence nearly spherical shapes. Whereas, larger droplets will have higher Weber numbers, hence complex deformed shapes.

A great amount of experimental, as well as numerical studies on droplet evaporation and combustion are available with the assumption of droplets as a spherical "non-deforming" particles under convective flow conditions [41, 44, 76]. However, there is a dearth of theoretical and analytical literature on the evaporation and combustion of "deformable" droplets. Before diving into the evaporation of deformable droplets, this chapter reviews major results on the evaporation of spherical droplets first. It is important to highlight that the term evaporation rate is somewhat ambiguous. In the combustion community[108], "evaporation rate" is widely used to refer to the net rate of change in mass of the droplet. However, in other contexts, the term "evaporation rate" is also used to describe the net rate of change in mass taken per unit surface area. In an effort to remove such ambiguity, a terminology of "total evaporation rate (net rate of change in mass)" and "evaporation flux (net change in mass taken per unit surface area)" is introduced which will be used throughout this work.

A widely common and fundamental approach in this field is to study quasi-steady droplet evaporation under quiescent ambient conditions. The result of such studies is the d^2 law which states that the total evaporation rate of a spherical droplet is proportional to its instantaneous diameter. Moreover, the droplet square diameter decreases linearly with time under such ambient conditions [98, 108].

An analytical study on droplet evaporation under convective flow by Law et. al [47] simplifies the flow over droplet by representing it as the flow of a gas stream over a liquid fuel stream. In the pressurized environment, the liquid surface velocities are significant when compared to free stream velocity. The higher surface velocity affects the internal motion in liquid which affects the evaporation rate. It was also shown that an increase in evaporation rate leads to a reduction in the interface velocity due to the thickening of the boundary layer around the liquid surface.

Such alteration in the gas phase boundary layer was further elaborated in a work by Renksizbulut and Yuen [82] who studied the effect of the composition of fuel-air and gas flow near the droplet on its evaporation rate. These numerical studies were performed at Reynolds numbers ranging from $Re = 10$ to $Re = 100$ for various liquid droplets and a solid sphere. Here, Reynolds number based on the initial droplet diameter d_0 can be defined as $Re = \frac{\rho_G U_{rel} d_0}{\mu_G}$. The results of this study revealed that decreasing the droplet surface temperature does not directly increase the Nusselt number (hence the evaporation rate) due to the presence of a steeper temperature gradient. The cold boundary layer of gas affects the evaporation rate via its effects on the thermal conductivity of the gas.

A work by Haywood et. al. [32] focused on the variable thermophysical properties of gas and transient processes in gas and liquid phase involved in droplet evaporation. The transient processes in the liquid phase were receding droplet size, fluid motion inside the droplet, and liquid heating. For inflow at $Re = 100$, an increase in the Nusselt number was seen in the early lifetime of the droplet due to the beginning of the surface blowing. Once, steady evaporation establishes, Nusselt number variation flattens with time. The angular variations in droplet surface temperature and fuel vapor mass fraction were more prominent at the early stage of evaporation due to strong sensitivity to vapor pressure. Moreover, due to the unsteady nature of liquid motion, the liquid temperature rises quickly up to the droplet surface temperature as time progresses and liquid heating can be considered quasi-steady.

Another common assumption in evaporation studies is neglecting liquid heating due to radiation. A recent work by Merino et. al. [60] quantified the effect of radiation using order of magnitude analysis. They studied evaporation of a single droplet in an inert stagnant environment under micro-gravity conditions. The authors identified the relevant timescales involved in evaporation. It was found that for larger droplets ($d > 0.5mm$) in high ambient temperature, the timescales for radiation heating and conduction heating are of the same order. Hence, d^2 trend can deviate significantly from the expected linear profile.

A recent comprehensive numerical work by Ray et. al. [80] quantified the effect of pressure, temperature, convection and initial-liquid phase composition on droplet evaporation. The droplet shape was considered to be nearly spherical as Weber number was $We \approx 0.3$ for the given conditions. Results showed faster evaporation rates at higher pressure due to net effect of decrease in gas diffusivity and surface tension, and increased latent heat. Higher ambient temperature and higher convective velocity favor the reduction in droplet lifetime.

The previous literature includes a wide variety of approaches used to study the evaporation of spherical droplets. Several major results exist demonstrating the effect of various environmental factors on their evaporation. However, much less work has directly studied the effect of deformation on evaporation. Haywood et al. [33] studied the dynamics of evaporating droplets in convection using a 2-D (axisymmetric) finite volume code. The code used a dynamic body-fitted mesh to solve for the droplet deformation and interface recession. However, their study focused on the effect of evaporation on droplet drag, and results for the effect of deformation on the evaporation rate were not studied in detail.

Mashayek [57] studied the effect of shape on droplet evaporation in quiescent flow using a finite element code. The work chose to impose droplet shape using arbitrary linear combinations of spherical harmonics. The work showed that evaporation enhances due to deformation, and it suggested that local evaporation could be related to the interface curvature.

Schlottke and Weigland [90] developed one of the first direct numerical simulation solvers for droplet evaporation in three dimensions. They validate the solver with correlations by

Ranz and Marshall [78], Kumala et al. [43], Renksizbulut et al [84]. Their results clearly indicated the non-uniform evaporation that occurs over the surface of the droplet, and the corresponding non-uniformity of vapor in the wake.

A theoretical study by Tonini and Cossali [105, 106] derived analytical solution for the steady state evaporation of ellipsoidal droplets under quiescent flow assuming constant density in both phases. To take into account of droplet non-sphericity on its evaporation, analytical expressions for evaporation rate and evaporation flux for ellipsoidal droplets (prolate and oblate shapes) were developed which generalize to the spherical droplet as well. The deformation parameter is $\epsilon = a_r/a_z$, where a_r is the radial spheroid axis and a_z is axial spheroid axis. Another variable β is ratio of surface area of spheroid (A_{sphd}) to the spherical droplet (A_{sph}), for the same liquid volume $\beta = A_{sphd}/A_{sph}$. Results showed for the same volume and β, prolate droplet ($\epsilon < 1$) has higher total evaporation rate in comparison to oblate shape ($\epsilon > 1$). Furthermore, the contours of vapor concentration revealed the relation between local vapor flux and the surface curvature is related to the fourth root of local Gaussian curvature of the droplet. This suggested that the maximum vapor flux is seen at the higher curvature region and the low flux is low curvature or flatter regions of the droplet.

The idea of non-spherical droplet evaporation was further expanded by Palmore [67] using a perturbation theory in his recent work. The work looked at evaporation and combustion of non-spherical droplets. The use of more realistic physics-based droplet shapes [104] than the ellipsoid is one of the novelties in his work. The assumption for this work were, the droplet at its saturation temperature, large density and viscosity ratio between liquid and gas, single component fuel and unity lewis number. The theories were established for a quiescent flow conditions. For a fixed low Re flow, We was selected as a perturbation parameter. The results agreed with the findings by Mashyek [57] and Tonini and Cossali [106] that the local evaporation flux relates to the local interface curvature. Moreover, higher total evaporation rate for prolate shapes than oblate shapes within the limit of smaller deformations was consistent with [106], [105]. The author also substantiated that although the total surface area of non-spherical droplet is higher than the spherical droplet, the total evaporation rate droplet does not scale by the total surface area ratio of non-spherical to a spherical droplet. In other words, it is the local evaporation flux that is affected by deformation.

It is noted again that the theoretical analysis by Tonini and Cossalli [105, 106], Palmore [67] as well as the numerical simulations by Mashayek [57] were performed under quiescent flow. Hence, a true quantification of the effect of deformation on the evaporation of freely-deforming droplets under planar convective flow is yet unknown. Therefore, the goal of this work is to gain insights about the interaction of droplet deformation and its evaporation rate under convective flow using DNS.

This work is organized as follows: Section 4.2 includes the further details about the flow solver in addition to Section 2.2. Section 4.3 discusses the numerical setup and boundary conditions. Subsequently, Section 4.4.1 includes the grid independence study and validation of solver with Abramzon and Sirignano analytical correlations. Finally, Section 4.4.2 demonstrates the main study on the influence of the deformation and planar flow on evaporation. The paper concludes with Section 4.5.

4.2 Methodology

4.2.1 Flow Solver

The fundamental equations to describe this problem and details of the numerical solver are same as discussed under Section 2.2.

4.2.2 Quasi-steady Evaporation

This section deals with quasi-steady droplet evaporation. From the thermodynamics point of view, a process is called quasi-steady when the system is slowly changing its state (i.e. pressure, temperature, entropy) while staying in continuous equilibrium with the surrounding. The quasi-steady assumption is very common within the literature of droplet evaporation and combustion studies, and many of the previously mentioned studies actually were in this regime. The d^2 law, a fundamental observation in droplet evaporation and combustion, is also derived under quasi-steady configurations.

In this computational code, the quasi-steady approach is implemented by fixing the liquid volume as constant throughout the simulation. Numerically, this is achieved by ignoring the evaporation flux term in Eq. (2.10). However the term is not ignored in other relations (Eqs. (2.9), (2.12), (2.13), (2.15) and (2.16)). This approach is somewhat analogous to the experimental studies on droplet evaporation using porous spheres [83, 119]. In that context, a liquid layer fully coats the outside of the sphere, and it evaporates slowly. Each sphere is fed with fluid through a tube such that the liquid volume remains constant throughout the study. This numerical approach for quasi-steady evaporation can especially be helpful in developing correlations of total evaporation rate as a function of initial Re and We. As in this case, the values for these quantities are constant in time.

4.3 Numerical Setup

The numerical setup for this study includes a single deformable droplet of diameter $d_0 = 100\ \mu m$ evaporating in a hot and pressurized incoming flow at $P_\infty = 20\ atm$ [115] and $T_\infty = 750\ K$. These conditions were selected to mimic environment of a gas turbine combustor. As a simplification, the liquid droplet is at its boiling temperature $T_\Gamma = 615\ K$. Hence, the internal heating of the droplet is not considered. Constant thermophysical properties of air and liquid fuel at these ambient conditions are listed in Table 4.1.

Property	Units	Air	Fuel
Density ρ	kg/m^3	9.41	300
Viscosity μ	$kg/(m \cdot s)$	3.48×10^{-5}	4.00×10^{-4}
Specific heat c_P	$J/(kg \cdot K)$	1086	13220
Thermal conductivity k	$W/(m \cdot K)$	0.054	0.079
Latent heat of vaporization h_{fg}	J/kg	—	4.81×10^4
Boiling temperature T_{boil}	K	—	615.05

Table 4.1: Fluid properties at $P_\infty = 20\ atm, T_{boil} = 615K, T_G = 750K$ [1]

The domain is of size $10d_0 \times 8d_0 \times 8d_0$ and the droplet is located at $(-d_0, 0, 0)$ with respect to origin $(0, 0, 0)$ as shown in Fig. 4.1. This domain size and the location of droplet center is selected such a way that the boundaries do not influence the flow field around the droplet.

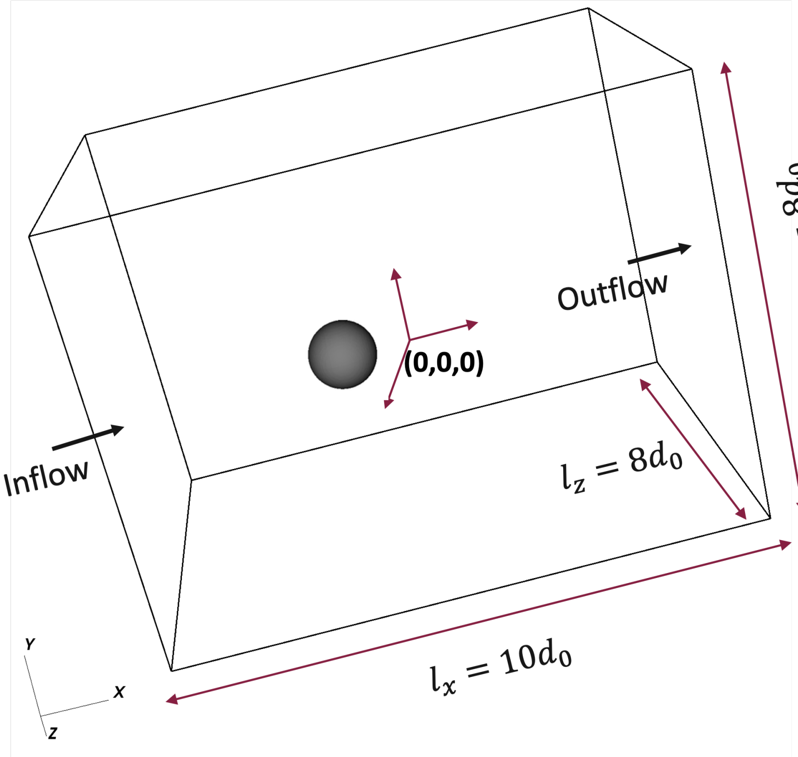

Figure 4.1: A sketch of numerical setup and boundaries

A uniform structured grid is used for this work. As depicted in Fig. 4.1, a fixed inflow boundary condition is applied on the negative x-face of the domain. To keep the droplet at its predetermined location, a method is deployed which mimics the flow over droplet as falling with its terminal velocity (U_T). This method has been tested and detailed in Section 3.2 and our previous works [50, 92]. This results in nearly constant U_{rel}. An outflow boundary condition is applied on the positive x-face of the domain. The remaining faces are treated as periodic boundaries. The domain is initialized with initial conditions obtained using d^2 law. This numerical setup is kept same for all the studies presented in this chapter.

It is important to note that because quasi-steady conditions are sought, data are analyzed after an initial transient period has ended. This transient period exists because droplets tend to oscillate when exposed to the flow. It takes some time for the internal forces on a deformed curved surface (surface tension and viscous forces) to balance with external aerodynamic pressure to reach a stable droplet shape [90]. The time to reach this shape is roughly, proportional to the capillary time scale τ_p given by Eq. (3.4).

4.4 Results and Discussion

4.4.1 Grid Independence Study

A grid convergence study is performed to find an optimum grid resolution required to capture the dynamics for the given problem. This is done by varying the grid length $dx = 12.5,\ 6.25,\ 4.17,\ 3.13,\ 2.08\ \mu m$. This corresponds to the number of cells per initial droplet diameter $N_{d_0} = 8,\ 16,\ 24,\ 32,\ 48$. The flow conditions $Re = 120$ [101], $We = 12$ are selected for this study. This Weber number is chosen to be below the critical Weber number for the onset of breakup which is usually 12 [36, 45, 54]. However, it is important to note that the droplet breakup does not solely depend upon Weber number. Other conditions such as density ratio, viscosity ratio, Ohnesorge number, flow velocity and type of flow around it affect the breakup time and the breakup mode [72, 112]. For a wide range of conditions relevant to liquid droplets in the air, $We \lesssim 12$, is sufficiently predictive for non-breakup.

The results from the grid independence study are plotted in terms of a non-dimensional parameter d^2/d_0^2 with non-dimensional time (t/τ_p) as shown in Fig. 4.2. It is noted that the slope of each curve is approximately constant after an initial transient period. The results also show that as N_{d_0} increases, the magnitude of the slope of droplet decay increases. Moreover, the slope of curve for $N_{d_0} = 24$ is observed to be nearly the same as $N_{d_0} = 32$ and $N_{d_0} = 48$.

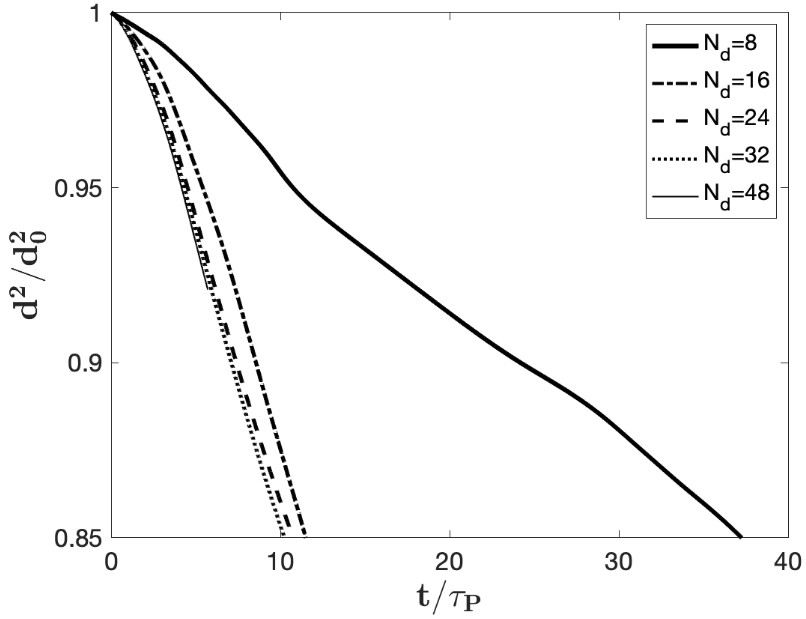

Figure 4.2: d^2/d_0^2 vs normalized time for various grids

Various grids are further compared in terms of Nusselt number Nu, which can be expressed as,

$$Nu = -\frac{2r}{(T_\Gamma - T_\infty)}(\boldsymbol{n}_\Gamma \cdot \nabla T) \tag{4.2}$$

Here r is the radius of droplet at that instant and $\boldsymbol{n}_\Gamma$ is the normal vector at the liquid-gas interface. Fig. 4.3 shows the surface average Nu for each grid. It is noted that unphysical droplet breakup was observed for $N_{d_0} = 8$ and 16, however, this does not appear at $N_{d_0} = 24$. Further refinement beyond $N_{d_0} = 24$ does not affect the breakup behavior of the solution. As the grid resolution is increasing, the gradients of temperature are captured more finely. Hence, Nusselt number is observed to be increasing. In case of $N_{d_0} = 24$, Nusselt number is found to be only 2.2% and 4.5% lower with respect to $N_{d_0} = 32$ and $N_{d_0} = 48$ respectively. Hence, $N_{d_0} = 24$ is found to be computationally appropriate for this work.

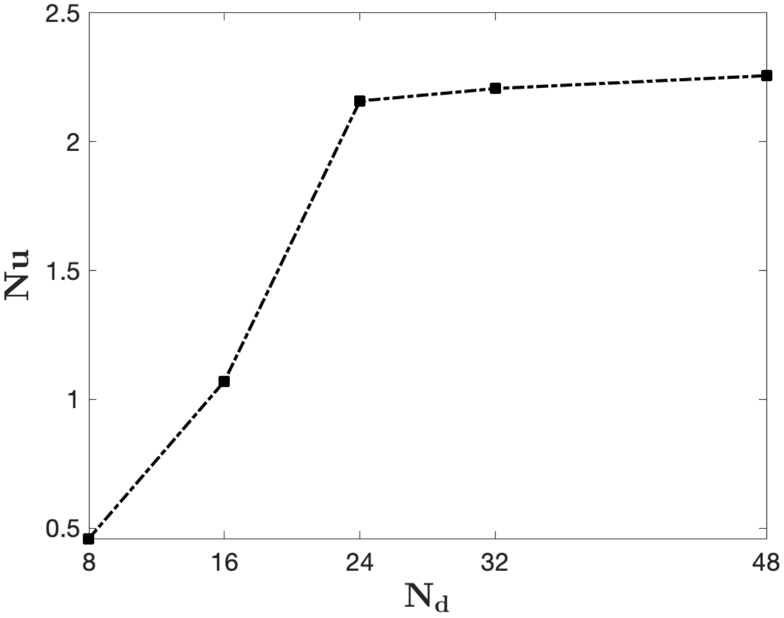

Figure 4.3: Nusselt Number (Nu) with cells per droplet diameter (N_{d_0})

Validation

This section discusses the validation of the numerical results against a semi-analytical theory of droplet evaporation developed by Abramzon and Sirignano [3]. This theory represents evaporation as rapid heat and mass transfer in a thin film over the droplet. The film theory predicts the Nusselt number as a function of Spalding heat transfer number ($B =$

c_{p_g} $(T_\infty - T_\Gamma)/h_{fg}$, Reynolds number ($Re$) and Prandtl number ($Pr = \mu c_p/k$). The film theory uses a correlation for the mass transfer in non-evaporating flows and further modifies it for to account of the film due to evaporation. Nusselt number in a non-evaporating flows is denoted as Nu_0 and Nusselt number for evaporating flows is denoted as (Nu). After correction in Nu_0 due to evaporation, Nu can be written as,

$$Nu = 2\left(\frac{\ln(1+B)}{B}\right) + (Nu_0 - 2)(1+B)^{-0.7} \tag{4.3}$$

The study by Abramzon and Sirignano [3] includes two expression for Nu_0. The first correlations for Nu_0 by Clift et al. [17] (CEA) is as follows,

$$Nu_{0,CEA} = 1 + (1 + Re\ Pr)^{1/3} f(Re) \tag{4.4}$$

Where, $f(Re) = 1$ when $Re \leq 1$ and $f(Re) = Re^{0.077}$ when $Re > 1$ in Eq. (4.4).

The second correlation for Nu_0 by Ranz and Marshall [78] (RM) is as follows,

$$Nu_{0,RM} = 2 + 0.552 Re^{1/2} Pr^{1/3} \tag{4.5}$$

The correlation from CEA is known to be more accurate, particularly at small Reynolds numbers. However, the RM correlation appears to be more widely used in practice. The modified Nusselt number for evaporating flow (Nu) using these two correlations is shown in Fig. 4.4. The plot shows the comparison of Nusselt number for an evaporating sphere (Nu) using Clift et. al. (solid blue line) and Ranz and Marshall (blue dot-dahsed line) at various Spalding heat transfer numbers.

Now, in order to test the accuracy of solver against the empirical correlations, the numerical results for the following conditions are overlaid on it. The flow conditions $Re = 25$ [101],

$We = 1$ [54] are selected for this study. These conditions are chosen to best match with the empirical correlations which deal with spherical droplets with fully attached boundary layer. This is done by varying the grid length $dx = 12.5,\ 6.25,\ 4.17,\ 3.13\ \mu m$. This corresponds to number of cells per initial droplet diameter $N_{d_0} = 8,\ 16,\ 24,\ 32$.

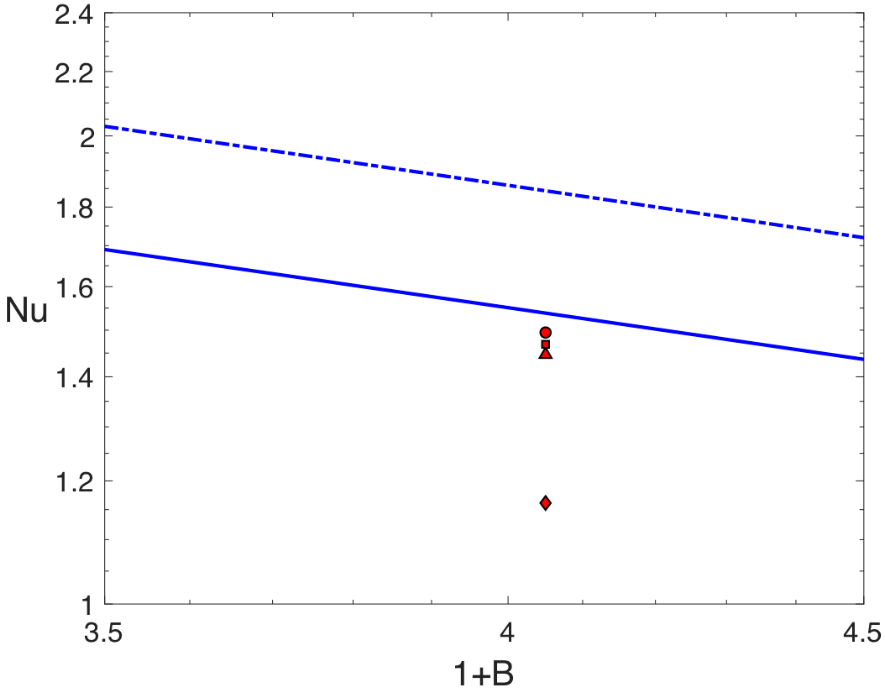

Figure 4.4: Nusselt number vs Spalding heat transfer number. *Blue solid line: Clift et al., Blue Dash line: Ranz and Marshall, Red markers: Numerical Results [Diamond marker: $N_{d_0} = 8$, Triangle marker: $N_{d_0} = 16$, Rectangular marker: $N_{d_0} = 24$, Circular marker: $N_{d_0} = 32$]*

The numerical results are shown here as markers in red with outline of black color. For a particular Spalding number $B = 3.05$, an increasing trend in Nusselt number is seen with the grid refinement. Additionally, Nusselt number from the numerical simulation move towards the correlation. The difference between the simulation results and the CEA correlation (Eq. (4.4)) is much less than that of the CEA correlation to the RM correlation (Eq. (4.5)). This suggests that the simulation results are within a reasonable band of error against the true solution. The % error with respect to empirical correlations from Clift et. al. is

$\boldsymbol{N_{d_0}}$	$\boldsymbol{Nu}$	**% error**
8	1.161	24.49
16	1.446	5.93
24	1.468	4.50
32	1.494	2.82

Table 4.2: % error in Nusselt Number (Nu)

tabulated in Table 4.2. Less than 5% error is seen between the simulation results and the CEA correlation for mesh size greater than $N_{d_0} = 24$. Therefore, based on these analysis, $N_{d_0} = 24$ is found to be an appropriate grid size in terms of computational expense as well as accuracy for further work.

4.4.2 Effect of Droplet Shape on Evaporation

After finding the appropriate grid and validating the results with the empirical correlations, this section covers the study of effect of droplet shape on its evaporation rate. As discussed previously, the droplet shape is governed by Weber number. In order to analyze the interaction of droplet shape with its evaporation rate, an isolated droplet with various Weber numbers under a convective flow is studied.

The droplet is nearly stationary and stays at its predetermined location, for a fixed U_{rel}, Re based on initial diameter d_0 is constant and We is modified by changing the surface tension. It is also important to recall that these non-dimensional numbers are constant and do not vary with time. $Re = 25$ and $Re = 120$ are selected for this study to cover a range of boundary layer behaviors. At $Re = 25$, the flow over a solid sphere is fully attached and at $Re = 120$, the flow behind a solid sphere is clearly separated with the steady ring vortex formation [101]. The range of Weber numbers selected for this study is $We = 1 - 12$ [54] which leads to the droplet shapes from spherical to highly deformed.

It is worth discussing the fact that as the droplets deform, they move from a spherical shape to a disk-like shape. More importantly, the effective diameter of the disk is larger than that of the original sphere, and this will affect the flow dynamics. In this work, this effect is captured implicitly through the measurement and discussion of the Weber number. However, no explicit measurements of the droplet deformation are made to quantify its effect on the flow. Such an approach is useful in practical model development for droplets since parameters such as Re and We are easy to measure. And this approach was chosen here since such model development is the long-term goal of this work.

The results for these cases are compared in terms of the normalized total evaporation rate ($\dot{m}_{ND}$) and its contributors: normalized local evaporation rate per unit area (normalized local evaporation flux) ($\dot{m''}_{ND}$), normalized surface area (A/A_0). These parameters are normalized using the total evaporation rate of droplet under quiescent flow based on d^2 law [108], defined as $\dot{m}_{d^2} = 4\pi r_0 \rho D ln(1 + B)$.

Normalized Total Evaporation Rate

Figure 4.5 shows the time history of normalized total evaporation rate ($\dot{m}_{ND}$). In all cases, the instantaneous evaporation rate starts at zero and rapidly increases. Since the droplet is preheated to the saturation temperature, this transient period is due to the adjustment of the gaseous flow field around the droplet. After some period of time, a plateau-like behavior is observed. At low Reynolds number $Re = 25$, the difference in $\dot{m}_{ND}$ is seen in the beginning for $We = 1 - 12$ (marked in dotted lines). However, at later time ($t/\tau_P > 15$), $\dot{m}_{ND}$ reaches a steady value for all Weber numbers. A more closer (zoomed-in) look at the results at $Re = 25$ displayed in Fig. 4.6 shows an increasing trend in $\dot{m}_{ND}$ with increase in We. Based on the spatially and time-averaged solution (after $t/\tau_P > 15$), the % increase in $\dot{m}_{ND}$ at $We = 12$ with respect to $We = 1$ is 3%. At $Re = 120$, a significant increase in total evaporation rate is observed with increase in Weber number as shown in the Fig. 4.5. This

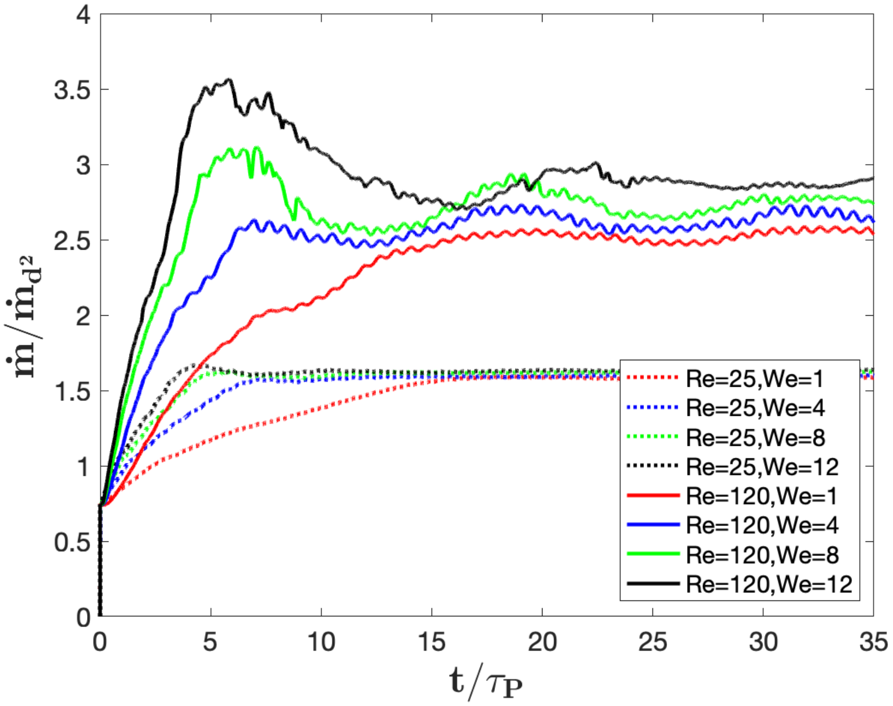

Figure 4.5: Normalized total evaporation rate ($\dot{m}_{ND}$) vs normalized time (t/τ_P) at $Re = 25$ and $Re = 120$

suggests that the Weber number has a clear effect on $\dot{m}_{ND}$ at higher Re. The % increase in $\dot{m}_{ND}$ at $We = 12$ with respect to $We = 1$ is 20%. Moreover, an oscillatory trend is observed for all the Weber numbers higher than 1 at both $Re = 25,\ 120$ especially during the transient period (till $t/\tau_p < 7$). This is more prominent at $Re = 120$. This appears to be due to oscillations in droplet surface area in Fig. 4.8.

Normalized Local Evaporation Flux and Normalized Total Surface Area

To find out the contribution of local evaporation flux ($\dot{m}''$) and surface area at $Re = 25$ and $Re = 120$, the results for normalized surface-averaged $\dot{m}''_{ND}$ and normalized surface area A/A_0 are plotted in Fig. 4.7 and Fig. 4.8, respectively. Results in Fig. 4.7 show that at $Re = 25$, $\dot{m}''_{ND}$ is marginally higher ($\sim 1\%$) for $We = 1$ in comparison to $We = 12$. At $Re = 120$, the effect of Weber number is clearly seen on the local evaporation flux at early

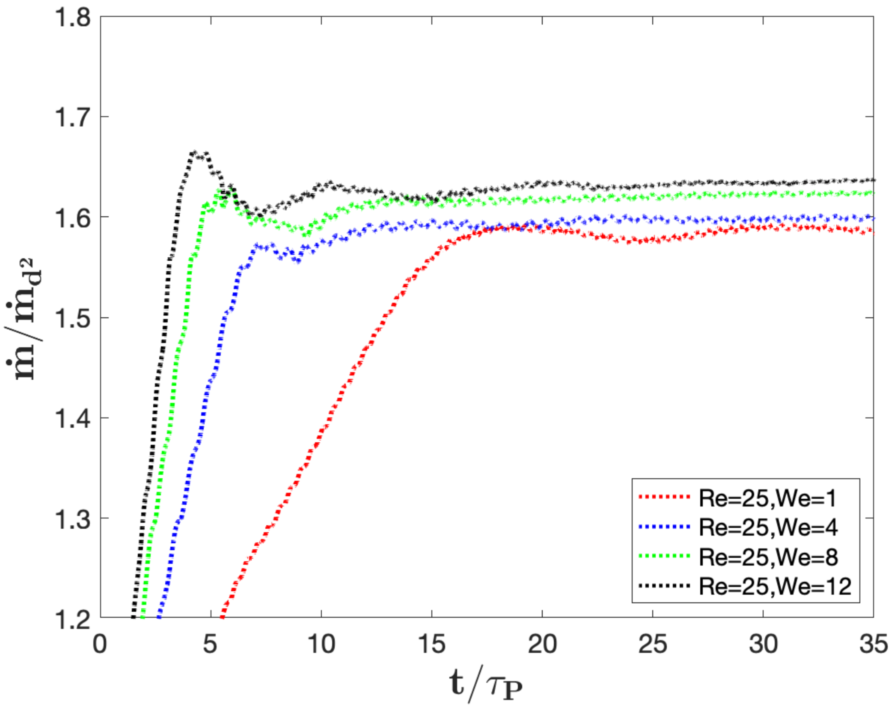

Figure 4.6: Zoomed-in plot for $\dot{m}_{ND}$ vs normalized time at $Re = 25$

time. Initially, as Weber number increases, $\dot{m''}_{ND}$ increases. However at later time, a clear trend can not be seen.

This trend in $\dot{m''}_{ND}$ seems to contradict its relation with curvature as per theoretical analysis by Tonini and Cossali [105, 106] and Palmore [67]. These previous studies were performed at $Re \approx 0$. However, in our studies, due to presence of convective flow over the droplet, the flow is more complex, for example, the flow separation is observed for both $Re = 25$ and $Re = 120$. In Section 4.4.2, we will discuss how the theories by Tonini and Cossalli and Palmore can be used to make limited predictions about the local evaporation fluxes, even for high Reynolds number studies.

Figure 4.8 shows the normalized total surface area (A/A_0) evolution with time. Here, A_0 is the initial droplet surface area. The results suggest that at any particular Reynolds number,

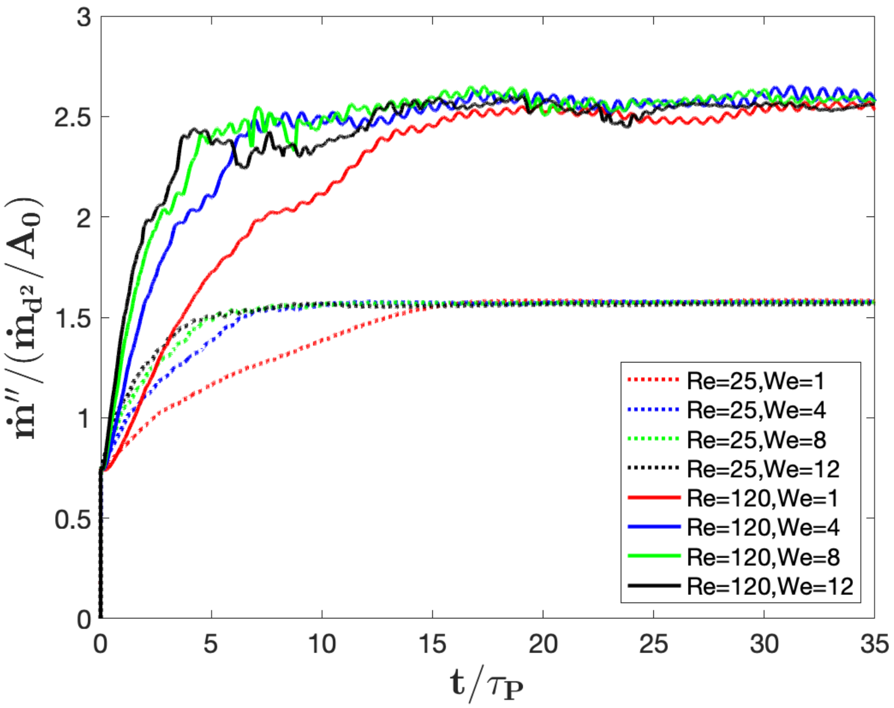

Figure 4.7: Normalized local evaporation flux ($\dot{m}''_{ND}$) vs non-dimensional time (t/τ_P) at $Re = 25$ and $Re = 120$

the droplet higher than $We = 1$ deforms significantly and reaches a peak of total surface area. Oscillations in droplet shape are reflected in the normalized area plot in Fig. 4.8 where two peaks are observed for every Weber number case. Moreover, this observation about the peaks in surface area ratio plot correlate well with the results shown in DNS study by Schlottke and Weigland [90]. At $Re = 25$, the steady value of maximum normalized area is after $t/\tau_P > 20$ is 1.04 and it occurs for $We = 12$. The cross section area in z-plane at time instance $t/\tau_P = 20$ is compared at $Re = 25$ in Fig. 4.9. The line style and color in this figure is kept consistent with plots for $\dot{m}_{ND}$, $\dot{m}''_{ND}$ and A/A_0 in Fig. 4.5 - Fig. 4.8.

At $Re = 120$, this increase in area is nearly 20% at $t/\tau_P = 20$ with respect to a spherical droplet and is highest for $We = 12$. A sectional view of droplet shape at this time instance is shown in Fig. 4.10. From this figure, 17% elongation in length perpendicular to flow with

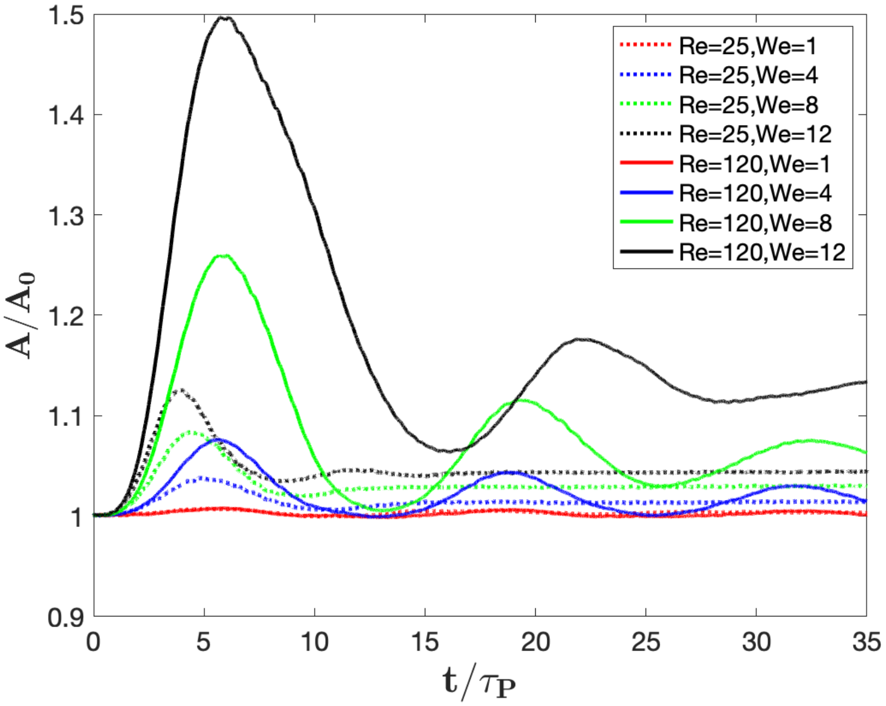

Figure 4.8: Non-dimensional Surface Area (A/A_0) vs non-dimensional time (t/τ_P) at $Re = 25$ and $Re = 120$

respect to initial diameter of spherical droplet is observed for $We = 12$. Hence, the net effect of both $\dot{m}''_{ND}$ and total surface area leads to increase in the total evaporation rate in case of $We = 12$ as shown Fig. 4.5.

Analysis of Local Evaporation Flux and Gas Flow

The qualitative analysis of the flow field at time instant $t = 20\tau_P$ is shown in Fig. 4.11. The psuedocolors of local evaporation flux along with the velocity vectors at $Re = 120$ for various Weber numbers are shown. In addition to this, four probes and a line segment are located inside the wake region to record the flow related parameters. Probe A is located near the rear stagnation point, probe B and C are located at the center of vortex and probe D is located at the end of wake.

These results show increasing deformation with increase in Weber number. This deformation

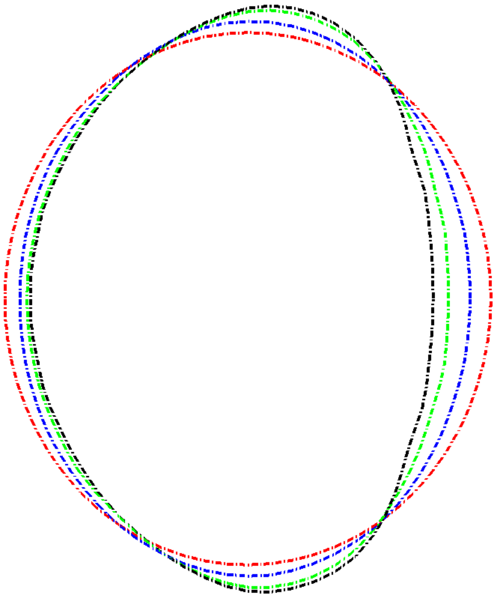

Figure 4.9: $Re = 25$: Cross-sectional view of droplet shape at $t/\tau_P = 20$.
Red : $We = 1$, Blue : $We = 4$, Green: $We = 8$, Black : $We = 12$

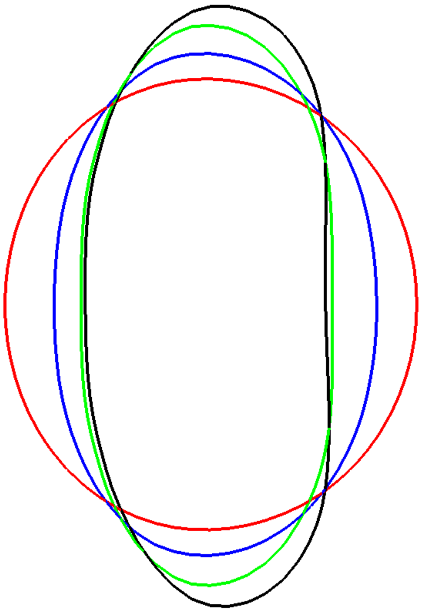

Figure 4.10: $Re = 120$: Cross-sectional view of droplet shape at $t/\tau_P = 20$. *Red : $We = 1$, Blue : $We = 4$, Green: $We = 8$, Black : $We = 12$*

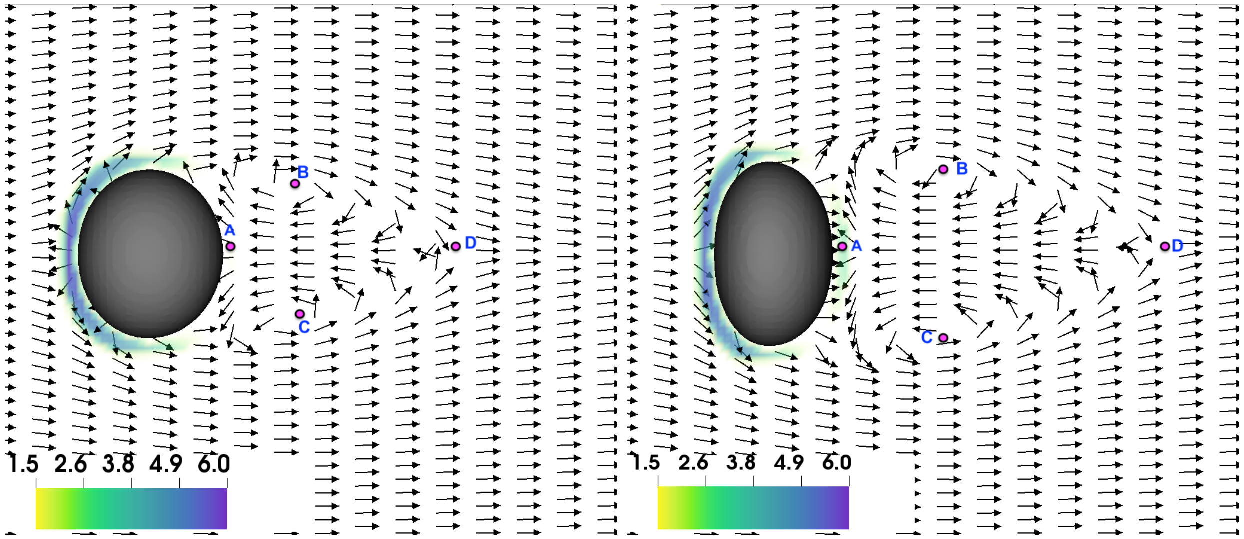

(a) $We = 1$ (b) $We = 4$

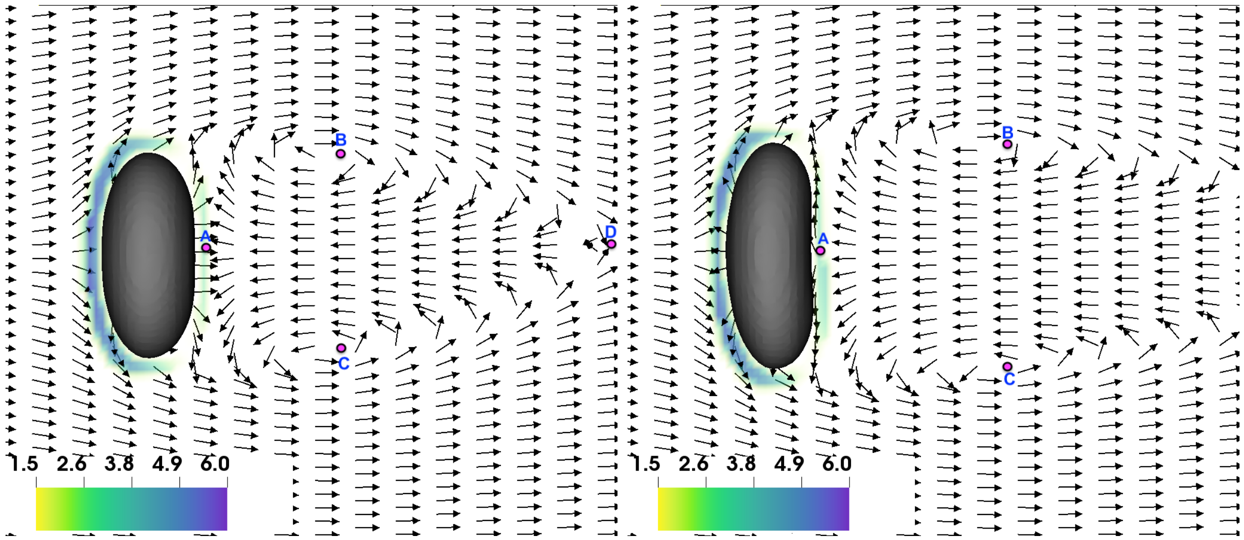

(c) $We = 8$ (d) $We = 12$

Figure 4.11: $Re = 120$: $\dot{m}''_{ND}$ for different Weber numbers at $t/\tau_p = 20$

correlates with a larger wake, both in terms of wake height H(measured between points B and C) and wake length L (measured between points A and D). Considering the flow axisymmetry, the approximate non-dimensional volume of wake scales as $V^* \sim (H/(2d))^2 \cdot (L/d)$. This data is tabulated in Table 4.3.

In terms of local evaporation flux, the majority of the evaporation occurs at the front of

$\boldsymbol{We}$	$\dot{\boldsymbol{m}}''_{\boldsymbol{ND}}$ at Pt. A	$\boldsymbol{L/d}$	$\boldsymbol{H/d}$	$\boldsymbol{V^*}$
1	2.37	1.89	0.87	0.36
4	3.06	1.99	1.13	0.64
8	3.34	2.45	1.19	0.88
12	3.62	3.42	1.45	1.86

Table 4.3: $Re = 120$: Measurements at different points inside wake region

the droplet (i.e. the windward side). Moreover, the evaporation flux in this region seems dependent on the local curvature of droplet as shown in Fig. 4.12. To elaborate on this, the psuedocolors of normalized curvature and $\Delta\dot{m}''_{ND}$ are plotted in Fig. 4.12. The curvature is normalized using curvature of a sphere of diameter d_0 and $\Delta\dot{m}''_{ND}$ is defined as $(\dot{m}'' - \dot{m}''_{avg})/(m_0/A_0\tau_D)$, where $\dot{m}''_{avg}$ averaged over time. Comparing $We = 1$ with $We = 12$, the curvature is higher in the front region which corresponds to the area of higher local $\dot{m}''_{ND}$.

Given this insight, the results of this study can now be compared with the low Re theories for evaporation by Tonini and Cossali [105, 106], and Palmore [67] which suggest the direct dependence of evaporation flux on the surface curvature. At the upstream stagnation point, the flow speed approaches zero, and accordingly the low Re theory is appropriate. Hence, the evaporation flux is found to be proportional to the curvature (shown in Fig. 4.12a and Fig. 4.12c) as predicted by theory given by [67, 105, 106]. However, as the flow develops around the droplet, this low Re approximation becomes inappropriate, and the curvature can no longer accurately predict evaporation flux. Furthermore, the low Re theories do not make any predictions for boundary layer separation, hence the previous theories have no validity for flow dynamics beyond the separation point.

It is also interesting to note that, for the non-spherical droplet such as Fig. 4.12b, the region of highest curvature occurs at the top and bottom of the droplet near the separation point, whereas the front stagnation region has a region of lower curvature than the corresponding sphere. Hence, the curvature-induced vaporization enhancement predicted by low Re theories is not experienced in practice for these highly deformed droplets. The net effect of these two phenomena imply that the evaporation flux for the deformed droplet on the front of the droplet must be lower than that of the spherical droplet. In addition to this, it will be demonstrated later that the evaporation flux on the rear is higher for deformed droplets, resulting in approximately equal overall local evaporation flux. This effect is also visible in the rear in Fig. 4.12d.

This enhancement in the downstream region can be attributed to the wake interaction with the fuel vapor. The velocity vectors in Fig. 4.11 show the presence of a vortex ring formation for all cases. The length of wake region is observed to be increasing with increase in Weber number. These details are quantified and tabulated in Table 4.3. It is clear that scaled volume of wake region is nearly 5 times larger for $We = 12$ in comparison to $We = 1$. As vapor mixing occurs only in wake, the larger wake is leading to the lower average vapor concentration. Since evaporation is driven by the gradient of vapor concentration between the liquid surface and its surrounding, the evaporation flux in this region is enhanced. An analogous claim can be made for the temperature, however in this case the temperature is increased in the wake due to mixing.

This viewpoint is supported by Fig. 4.13, which delineates the vapor mass fraction and temperature profiles behind the droplet. The data are extracted on a line segment that starts at $(-0.7d_0, 0, 0)$ (near the rear of the droplet) and ends at $(2.5d_0, 0, 0)$ to cover the maximum wake length, as demonstrated in Fig. 4.13a. The vapor mass fraction is decreasing monotonically with We, whereas the temperature has the opposite trend. In both cases, the trend indicates mixing of values between the interface conditions and the farfield conditions. Accordingly, this leads to higher gradients and higher evaporation rates in the wake region as shown in Fig. 4.11 with increase in We number.

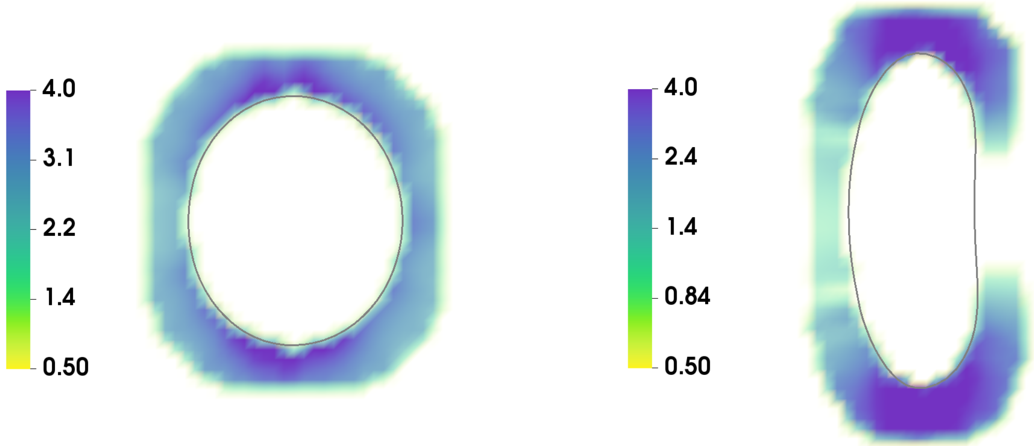

(a) $We = 1$: Normalized curvature (b) $We = 12$: Normalized curvature

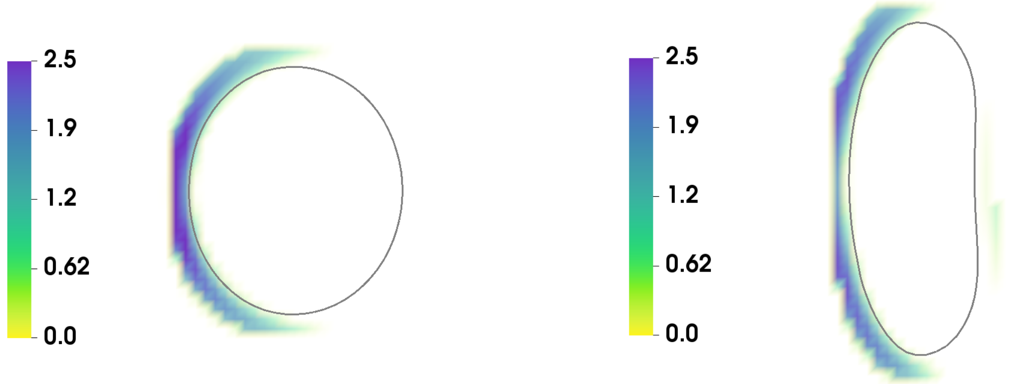

(c) $We = 1$: $\Delta\dot{m}''_{ND}$ (d) $We = 12$: $\Delta\dot{m}''_{ND}$

Figure 4.12: $Re = 120$: Distribution of normalized curvature and normalized $\Delta\dot{m}''$ at $t/\tau_P = 20$

4.5 Conclusions

With the motivation to understand the complex relationship between the droplet shape and its evaporation rate, this chapter covers the droplet evaporation under convective flow using interface capturing Direct Numerical Simulation for multiphase flows. The liquid-gas

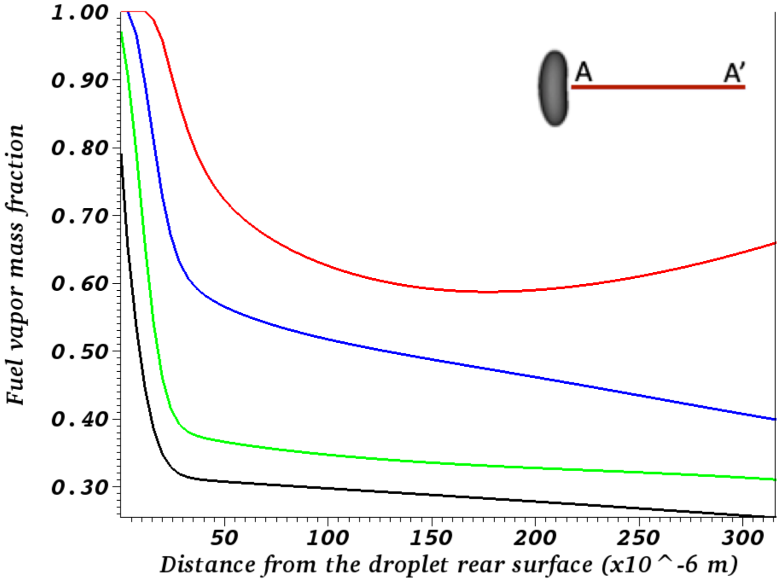

(a) Vapor Mass Fraction

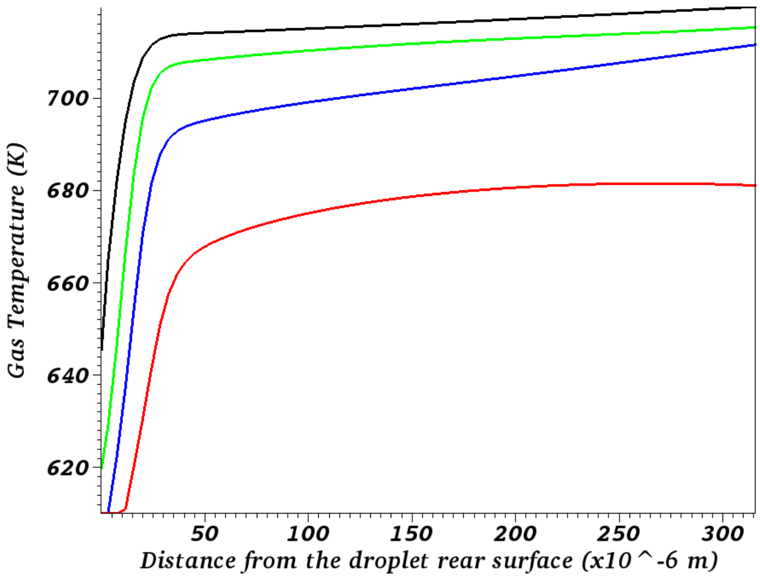

(b) Gas Temperature

Figure 4.13: $Re = 120$: Vapor Mass Fraction and Gas Temperature along the line segment AA'.
Red : $We = 1$, *Blue* : $We = 4$, *Green:* $We = 8$, *Black* : $We = 12$

interface can deform freely in these studies. A grid independence study is performed and the solver accuracy is validated against empirical correlations for droplet evaporation by Abramzon and Sirignano [3].

To analyze the effect of droplet shape on its evaporation rate, quasi-steady approach is implemented, where the liquid volume is artificially kept constant in simulations while still solving the remaining equations for the fluid dynamical system. For a constant relative inflow velocity, the droplet shape is varied by modifying Weber number from $We = 1 - 12$. The convective flow velocity is modified by changing initial Reynolds number $Re = 25, 120$.

At $Re = 25$, the increase in total evaporation rate at $We = 12$ with respect to $We = 1$ is 3% which is marginal. However, at $Re = 120$ and $We = 12$, 20% enhancement in total evaporation rate is observed when compared to $We = 1$. To understand the source of this enhancement, the total evaporation rate was decomposed into evaporation per unit surface area ($\dot{m}''$) and surface area. This enhancement is mostly coming from increase in surface area due to deformation and the averaged value of evaporation flux seems to be nearly same for all Weber number.

At first glance, this appears to contradict the established theories for droplet evaporation Tonini and Cossali [105, 106], Palmore [67]. However, this effect is due entirely due to the high Reynolds number phenomena including boundary layer separation. Interestingly, for the front (i.e. windward) stagnation region that forms over the droplet, the evaporation flux is proportional to the interface curvature, as predicted by the low Re theory. However, as a consequence of the boundary layer behavior, the evaporation flux for deformed droplets is lower on their fronts when compared to nearly spherical droplets.

After the flow separation, the formation of wake and its interaction with fuel vapor is observed at the downstream. Due to this interaction, the evaporation flux on the rear (i.e. leeward) side of the droplet is enhanced where the flow is separated. This effect largely cancels out the diminished evaporation flux on the front of the droplets, and results in similar values for surface averaged evaporation flux. This emphasizes the importance of boundary layer development in evaporation for higher Reynolds number flow and suggests a more complex relationship between Weber Number, Reynolds Number, and evaporation phenomena than had been previously predicted.

Chapter 5

Evaporation of Deformable Droplet Under Natural Convection

The work covered in this chapter is submitted as a draft paper for the AIAA SciTech conference (2024) [96]. The complete details are as follows,

- Meha Setiya and John Palmore Jr. Evaporation of deformable droplets under natural convection: comparison of DNS results with experiments. In AIAA Science and Technology Forum and Exposition (AIAA SciTech Forum), 2024.

5.1 Introduction

In most of the spray combustion systems, the sprays are exposed to mixed convective environment (i.e. combination of natural convection and forced convection) [77]. Besides the ambient gas flow conditions, the size of droplets in sprays also varies from a few micrometers to a thousands of micrometers [98]. Since the large droplets make most of spray mass [94], the evaporation of these can be a rate limiter for combustion [22]. The overall effect of mixed/forced convection on the evaporation of these droplets is well known from literature [67, 95, 120]. However, the effect of natural convection is generally neglected in forced convection dominant flows. The experimental studies such as [12, 31, 111] showed a significant potential in natural convection to modify the evaporation/burning rates of droplets. These changes in overall burning rates and flame shape are more evident in the complete absence of gravity such micro-gravity conditions [71, 88]. This hints towards an interaction between droplet evaporation and buoyancy driven flow around it. With the motivation to understand the interaction between the natural convection and droplet evaporation, this study focuses on droplet evaporation under buoyancy-driven flow using Direct Numerical Simulation (DNS).

In case of droplets evaporating under quiescent flow, the presence of temperature gradients between two fluids governs the density variation in flow. This leads to the generation of natural convection current due to variable buoyant forces on the fluids. This phenomenon is generally characterized by a non-dimensional number known as Grashof number [8].

$$Gr_0 = \frac{g \Delta\rho d_0^3}{\rho \nu^2} \tag{5.1}$$

Here, $\Delta\rho$ is the density change due to temperature change in a phase, g is gravitational acceleration, ν is the kinematic viscosity of the gas, d_0 is the initial diameter of the droplet. For evaporating flows, this density change in gas phase is evaluated as $\Delta\rho = \bar{\rho_\Gamma} - \rho_\infty$ where

$\bar{\rho_\Gamma}$ mean density of gaseous mixture at the droplet surface [26]. Moreover, due to the presence of surface tension and flow development around the droplets, they have tendency to deform from initial spherical shape to a non-spherical shape. Such non-spherical shapes were also observed in experimental studies on burning droplets under normal gravity conditions [88]. However, this was not under the scope of their work. In such buoyant flows, the shape of droplet can be characterized using "Eötvös Number (Eo)" [17], defined as ,

$$Eo_0 = \frac{\Delta \rho g d_0^2}{\sigma} \tag{5.2}$$

here σ is surface tension of liquid.

To address this problem in a systematic manner, this paper first reviews the major work on droplet evaporation under quiescent flow.

The experimental studies such as [27, 59, 61, 88] covered the droplet evaporation under quiescent flow. Sato et al. [88] studied the effect of pressure under normal and micro-gravity on combustion of n-octane. With the rise in ambient pressure till critical pressure, the burning rate was seen to be increasing. Whereas, the burning rate decreased with ambient pressure above critical pressure under normal gravity. The results also showed the presence of natural convection under normal gravity increases the heat and mass transfer rates from the droplet surface, therefore shorter burning times when compared to micro-gravity cases. Moreover, non-spherical flame shapes were seen under normal gravity and spherical flame shapes in micro-gravity cases at all ambient pressures. This indicated towards the strength of gravity and its interaction with flow development around the droplet.

Another experimental study by Verwey and Birouk [111] investigated the effect of droplet size varying between $140 - 700\ \mu m$ on its evaporation rate under quiescent conditions at elevated pressures (below critical pressure) and temperature in normal gravity. The results showed that, at any particular ambient pressure, larger droplets evaporate faster in comparison to smaller droplets which is in agreement with the d^2 law [108]. The ambient pressure affects the evaporation rate coefficient ($K = d(d^2)/dt$) positively for larger droplets ($d_0 > 400\mu m$). Moreover, the evaporation rate at higher pressure tends to deviate from the d^2 law distribution at the later stages of evaporation due to higher natural convection especially for larger droplets. The authors also suggested that the effect of Grashof number is more prominent at high pressure conditions. These observations were also noted by Chauveau et al. [12] for evaporation of $d_0 = 1.5\ mm$ droplet in quiescent flow under normal gravity. The d^2 law was corrected using Grashof number to account for the effect of buoyancy.

Gokalp et al. [27] conducted low temperature droplet burning under normal and reduced gravity conditions under both natural and forced convection. They found that the assumption of spherical flame no longer holds for convective conditions. Moreover, due to presence of silica filament to hold the droplet, the droplet shape was closer to an ellipsoid than a sphere in their experiment. The burning rates or surface regression rates using d^2 law involved calculation of characteristic dimension based on equivalent surface area or volume of a sphere. However, the effect of droplet shape specifically on burning rate was not the focus of their work.

Another interesting experimental investigation by Hegseth et al. [34] focused on visualizing the liquid phase only and demonstrated the effect of surface tension on droplet evaporation. A methanol droplet of size 1 mm was studied under stagnant air at atmospheric pressure and room temperature. Results showed that the gradient of temperature at the droplet surface due to evaporation induces gradient of surface tension. This variation in surface tension drives the circulating (cellular) flow within the droplet which is also known as marangoni instability. Higher internal motion leads to lower difference in temperature between the droplet surface and its core. Such convective flow was absent inside water droplet and strongly present inside acetone droplet, suggesting that the internal flow is dependent of the density ratio of two fluids [47, 49, 50]. The gas-vapor flow outside the droplet was not resolved in their study.

A latest experimental work by Murakami et al. [61] presented the droplet evaporation of n-decane under normal gravity and microgravity. The focus of this work was investigation of the unsteadiness in evaporation due to natural convection. Larger droplets were observed to be more susceptible to evaporation enhancements due to prominent natural convection at pressure lower than the critical pressure. The results showed that the droplet evaporation coefficient reflects the unsteady evaporation behavior with time and it does not stay constant during the entire evaporation time.

On numerical and anlytical work front, Habchi and Ebrahimian [31] developed a model for multi-component droplet evaporation with correction in heat transfer and gravity. The heat flux was corrected by including the conventional conduction heat flux and the heat flux due to enthalpy diffusion of species. The relevant non-dimensional number Sherwood (Sh) and Nusselt number (Nu) were corrected using Grashof number (Gr). The assumptions for this model were: the droplet is spherical at a constant surface temperature, no radiation, Soret and defour effects were considered. Including these assumptions and corrections, this proposed model showed good agreement for single component droplet evaporation under quiescent flow at different temperatures with results reported in [13].

Gogos et al. [26] developed an axisymmetric numerical model for droplet evaporation (n-hexane, n-heptane) at elevated pressure conditions under normal gravity and micro-gravity. The results were validated against experimental work by [59, 61]. Their numerical model included a non-ideal gas behavior, the solubility of inert gas inside the liquid, variable liquid and gas properties, real gas effects on the vapor–liquid equilibrium at droplet surface and the internal circulation inside droplet. To compute liquid-vapor equilibrium at the interface, authors used Peng-Robinson equation of state. One of the key assumptions was the droplet shape stays spherical considering the Weber number (due to buoyant flow) is small. However, the droplet shape was observed to be nearly elliposidal at high pressure conditions under normal gravity. This was due to decrease in surface tension with increase in pressure. Their results also showed that the evaporation under micro-gravity is less sensitive to rise in pressure when compared against normal gravity.

Based on this review, the previous studies either considered the droplet to be spherical for the entire droplet lifetime [12, 26, 88] or they solely focused on resolving the liquid phase [34]. Therefore, there is a gap in understanding the interaction of the natural convection, droplet shape on the droplet evaporation both under normal gravity and micro-gravity. This work intends to bridge that gap using Direct Numerical Simulation (DNS) approach which can resolve both the liquid and gas phase along with the droplet deformation. The main aim of this work is to expand our understanding of evaporation in environments with partial gravity.

As a first step towards this aim, the focus of this paper is to validate the numerical results with two sets of experimental results. The first data set includes the latest experimental data for droplet evaporation under atmospheric conditions in micro-gravity. This experiment was conducted by one of our co-authors at international space station. The second test data is an existing experimental data from Murakami et al. [61] for the evaporation of a single isolated droplet of n-decane in quiescent flow under micro-gravity. The initial diameter of the droplets used in the experiments are $d_0 = 3.68\ mm$ and $d_0 = 0.4\ mm$ respectively which is considerably larger than $d_0 = 0.1\ mm$ as smaller droplets are less sensitive to natural convection [26]. For the ease of understanding, these experimental results will be designated as Experiment-1 and Experiment-2 respectively from this point forward. This paper is organized as follows, Section 5.2 details about the methodology used in experiments and numerical analysis. Section 5.3 covers the details of problem formulation and numerical setup. This is followed by results and discussion under Section 5.4.

5.2 Methodology

5.2.1 Experiment-1 Methodology

The experimental data for droplet evaporation were obtained in the Multi-user Droplet Combustion Apparatus (MDCA) onboard the International Space Station (ISS) as part of the Flame Extinguishment-2 (FLEX-2) program. The experimental set-up is adopted from Dietrich et al. [20] and shown here in Fig. 5.1.

Experimental procedures are briefly discussed here, and detailed descriptions of the hardware can be found in [7, 20, 37]. Two needles, separated by a small distance, are used to dispense liquid fuel and form fuel droplets. The needles are retracted once the desired droplet size is reached. Two hot wires are then energized, attempting to ignite the fuel droplet. For the evaporation results reported here, the ignition mechanism failed to ignite the droplet due to various reasons such as insufficient input energy and the distance between the hot wires and the droplet. Therefore, the droplet continues to evaporate without combustion for a relatively short period of time. The droplet evaporation process is recorded by a High Bit-Depth Multispectral (HiBMs) camera (1 MP at 30 fps) with backlighting. The images of burning n-decane droplets in the FLEX-2 program were previously reported in [53], which emphasized the droplet and flame dynamics as the initial droplet size varies. In this experimental work (Experiment-1), the efforts have been focused on the evaporation rate of n-decane with no chemical reactions. The images of droplet evaporation were analyzed in [117], and the data are used here to validate the numerical modeling.

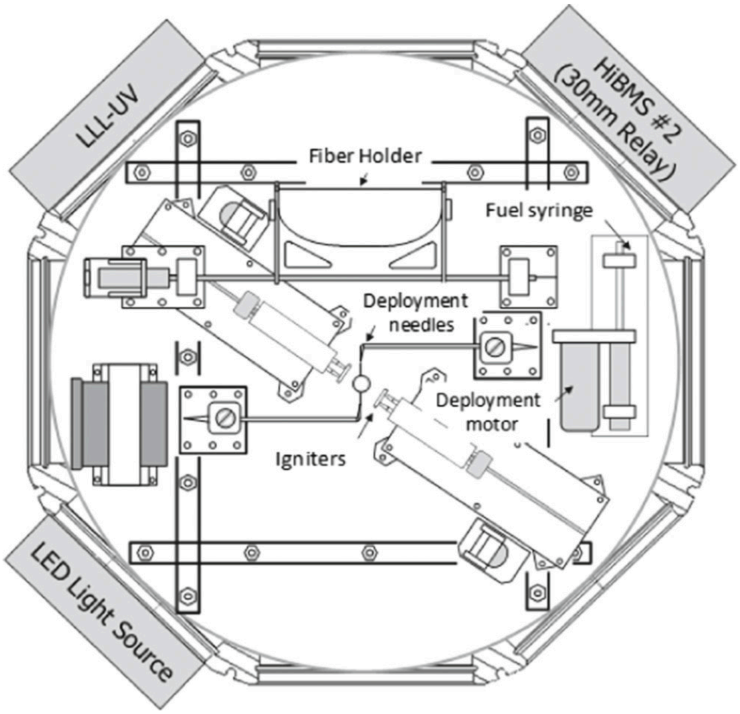

(a) Schematic of the Multi-user Droplet Combustion Apparatus (MDCA)

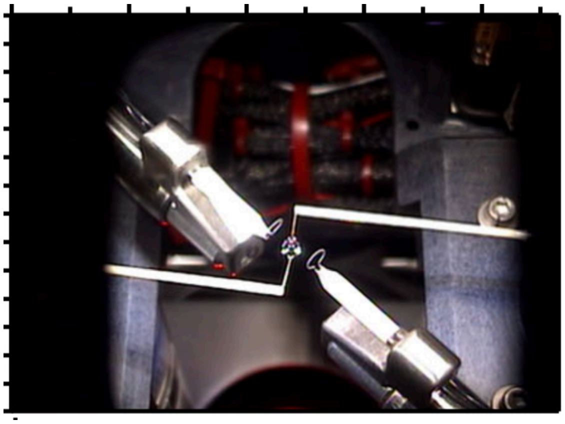

(b) FLEX image of droplet before ignition

Figure 5.1: Experiment-1 setup [20]

5.2.2 Numerical Methodology

The problem described under Section 5.1 is simulated using a finite volume based framework. The details of this framework are discussed in Section 2.2, therefore not repeated here. In addition to transport equation, the computation of variable density is discussed in this section.

Variable Density in Each Phase

To include the capability of solving natural convection flow physics into our incompressible flow solver, the Boussinesq approximation for both liquid and gas phases is implemented. The density in the gas phase varies as per ideal gas law [8] which can be written as,

$$\rho_G^* = \frac{P_{thermo}}{RT_G} \tag{5.3}$$

Here P_{thermo} is thermodynamic pressure, R is specific gas constant which depends upon the molecular weight of vapor-air mixture, computed as $R = R_u/MW_{mix}$.

Similarly, the density variation in liquid phase depends upon the coefficient of thermal expansion (β) and the temperature difference between varying core liquid temperature (T_L) and liquid surface temperature (T_Γ). The density in liquid phase can be expressed as,

$$\rho_L^* = \frac{\rho_L}{1 + \beta(T_L - T_\Gamma)} \tag{5.4}$$

Therefore, the gas phase density varies with thermodynamic pressure, temperature and the fuel-vapor mass fraction which evolve over time. Whereas, the liquid phase density varies with liquid temperature. These variable densities are used in the transport equations as descibed in Section 2.2.

5.3 Problem Formulation

5.3.1 Numerical Setup

To study this problem numerically, two isolated droplets of n-decane are selected and analyzed separately. The initial droplet diameters of these are $d_0 = 3.68\ mm$ (from Experiment-1) and $d_0 = 0.375\ mm$ (from Experiment-2). These droplets are located at the center of a cubic domain of size $(25d_0)^3$ as shown in Fig. 6.1. To resolve the gas and liquid phase appropriately, a uniform grid of size $\Delta x = \Delta y = \Delta z = d_0/16$. This corresponds to 16 grid cells per droplet diameter ($N_d = 16$). This domain size is selected such a way that the boundaries do not influence the flow near the droplet. The left x-boundary of the domain is treated as an inflow boundary and right x-boundary is free outflow, the boundaries in y and z directions are treated as periodic boundaries. The inflow velocity is approximately zero for quiescent flow conditions.

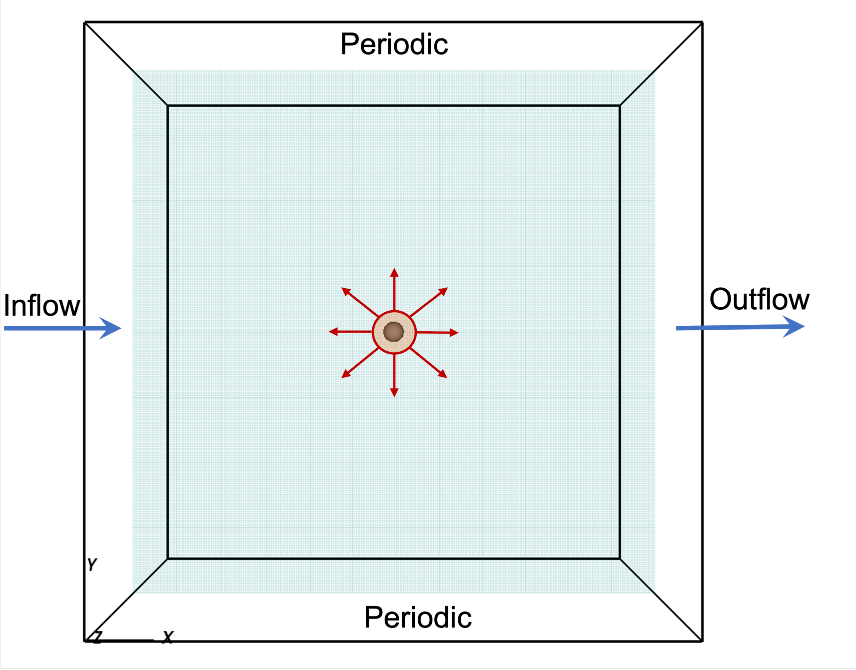

Figure 5.2: A sketch of computational domain

Instead of using the exact conditions from the measured data and the conditions mentioned in Murakami et al. [61], the temperature of liquid and gas is derived from the experimental results. This is discussed in detail under Section 5.3.2. The motivation behind deriving these conditions is the uncertainty in the measurement of the droplet surface and ambient gas conditions. For example, in the results from Murakami et al. [61] the droplet was significantly heated while it was moved from the droplet generator to test section. The added motion to the droplet led to additional shear stress at the interface and hence introduced internal circulation, which led to higher surface temperatures. This was reported by Gogos et al. [26], Zhang et al. [121] in their validation work. It is also important to note that the droplet is suspended using a $7\mu m$ $Al_2O_{3/}SiO_2$ fiber in experiment whereas it is freely floating in the presented numerical studies. Although this fiber material is nearly thermally insulated, such droplet suspension method can affect the heat transfer to the droplet [14]. While setting up the case, the gravitation acceleration (g) is set to $g = 1 \times 10^{-04}\ m/s^2$ to mimic micro-gravity conditions from the Experiment-2.

The fluid properties at these conditions [1] are given in Tables 5.1 and 5.2. The thermophysical properties such as thermal conductivity and dynamic viscosity are constant and do not vary with time. The initial fuel-vapor mass fraction at the droplet surface (Y_{F0}) is computed using Clausius-Clapeyron Equation Eq. (2.14a) which is detailed under Section 2.2.4.

5.3.2 Initial Temperature of Liquid and Gas Phase

This section demonstrates the evaluation of liquid and gas temperature for numerical setup. In case of Experiment-2, as original test data from Murakami et al. [61] was unavailable, the results reported in Figure 4 in [61] are digitized and shown here in Fig. 5.3. The black solid line represents the digitized experimental results. An increase in d^2/d_0^2 in the beginning of evaporation is observed. This could be due to thermal expansion of liquid droplet and initial unsteady evaporation behavior. Moreover, the slope of the black line does not remain

Property	Air	Fuel
Temperature (T)	360	340
Density (ρ)	0.98	693.88
Viscosity (μ)	2.12×10^{-5}	5.03×10^{-4}
Specific heat (c_p)	1009.50	2355.70
Thermal conductivity (k)	3.09×10^{-2}	11.89×10^{-2}
Latent heat of vaporization (h_{fg})	–	373943.66
Surface tension (σ)	–	1.95×10^{-2}
Coefficient of thermal expansion (β)	–	1.12×10^{-3}

Table 5.1: Experiment-1 : Fluid properties at $P_\infty = 101325\ Pa,\ T_{boil} = 447.3\ K, T_L = 340K,\ T_G = 360\ K$ [1]

Property	Air	Fuel
Temperature (T)	640	521.69
Density (ρ)	2.72	524.87
Viscosity (μ)	3.15×10^{-5}	1.20×10^{-4}
Specific heat (c_p)	1059.40	3053.60
Thermal conductivity (k)	4.80×10^{-2}	8.10×10^{-2}
Latent heat of vaporization (h_{fg})	–	218660
Surface tension (σ)	–	4.89×10^{-3}
Coefficient of thermal expansion (β)	–	2.41×10^{-3}

Table 5.2: Experiment-2 : Fluid properties at $P_\infty = 0.5\ MPa,\ T_{boil} = 522.7\ K,\ T_L = 521.69\ K, T_G = 640\ K$ [1]

constant throughout the droplet lifetime. This suggests that the evaporation coefficient (K) varies with time as reported in the paper. Such unsteadiness will be missing in analytical solution as it involves a steady state evaporation and demonstrate a constant linear slope of the d^2 distribution. Therefore, to compare the analytical against experimental data, the experimental data is clipped at $d^2/d_0^2 \approx 0.88$ such that the curve shown in dash blue line without markers have nearly constant slope $K = 2.80 \times 10^{-07}\ m^2/s$. Now, this clipped data is shifted to time ($t/d_0^2 = 0$) such that d^2/d_0^2 starts at 1 with initial diameter of droplet as $d_0 = 0.375\ mm$. This data is further used for validation purpose.

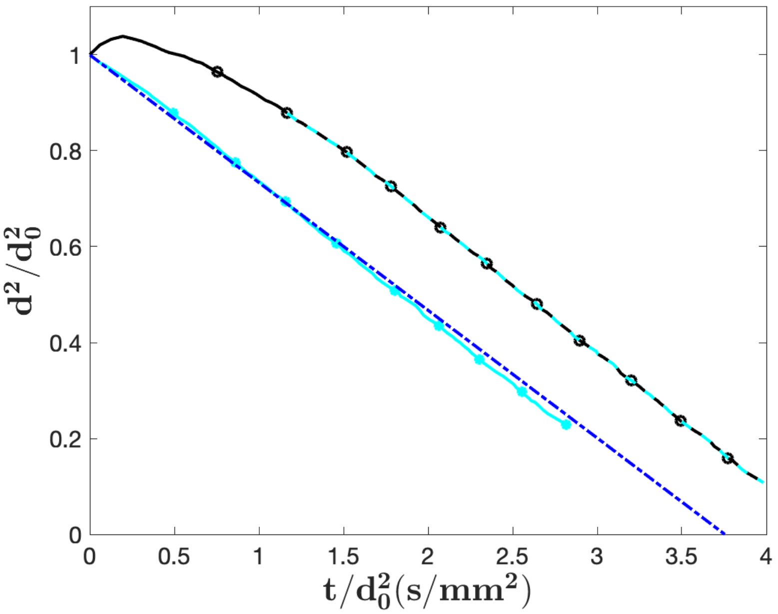

Figure 5.3: $d_0 = 0.375mm$: Experimental results for droplet evaporation under microgravity [61].
Black solid line: Digitized experimental data, Cyan dash line: clipped experimental data, Cyan solid line with filled markers : clipped and shifted experimental data, Blue dash line: analytical solution

To derive the boundary conditions for DNS, an analytical solution for droplet evaporating under quiescent flow is used [108]. This analytical solution (shown in cyan) of d^2/d_0^2 for a droplet evaporating under quiescent can be written as,

$$d^2/d_0^2 = 1 - K * (t/d_0^2) \tag{5.5a}$$

$$K = \frac{8k_G(\bar{T})ln(1 + B_q)}{\rho_l(T_\Gamma)c_{p,G}(\bar{T})} \tag{5.5b}$$

$$B_q = \frac{c_{p,G}(\bar{T})(T_\infty - T_\Gamma)}{h_{fg}} \tag{5.5c}$$

Here $\bar{T}$ is mean temperature , K is evaporation coefficient and B_q is Spalding heat transfer number. Gas and liquid properties for this solution are computed at mean temperature. The analytical solution which matches the most of d^2/d_0^2 trend of experimental result is found when $K_{analytical} = 2.67 \times 10^{-7}\ m^2/s$. This corresponds to $T_\infty = 640\ K$ and $T_\Gamma = 521.69\ K$. These temperatures are used to evaluate gas and liquid properties at $P_\infty = 0.5 MPa$ for DNS.

The boundary conditions for Experiment-1 are also derived in the same fashion, therefore the process is not repeated here. For atmospheric pressure condition and evaporation coefficient $K = 1.79 \times 10^{-8}\ m^2/s$ from experiment, the derived boundary conditions are $T_\infty = 358.2\ K$, $T_\Gamma = 338.2\ K$, $Y_{F\Gamma} = 0.0493$.

5.4 Validation

5.4.1 Validation against Experiment-1

This section covers the comparison of DNS solution against analytical solution and the results from Experiment-1. The measured data in Experiment-1 (shown in black in Fig. 5.4) is significantly fluctuating, an in-built Matlab function is used to smooth/filter the data. This smooth data is shown in Cyan colored dash line. The d^2/d_0^2 higher than 1 is observed in these results which may be present due to initial droplet heat-up. It is also observed that the droplet lost a small amount of mass for a short period of time during this experiment. The normalized squared diameter dropped from 1 to 0.992 in 0.6 s/mm^2 normalized time.

To utilize this filtered data further for the validation purpose, it is clipped using the same approach discussed in Section 5.3.2. Fig. 5.5 shows the comparison of dimensionless squared diameter obtained from three different approaches. The filtered and clipped experimental results are shown in cyan solid line with markers. The analytical solution for steady evaporation of droplet under quiescent flow [108] is plotted in blue dash line. As the evaporation coefficient is constant for analytical solution. The slope of this curve matches with exper-

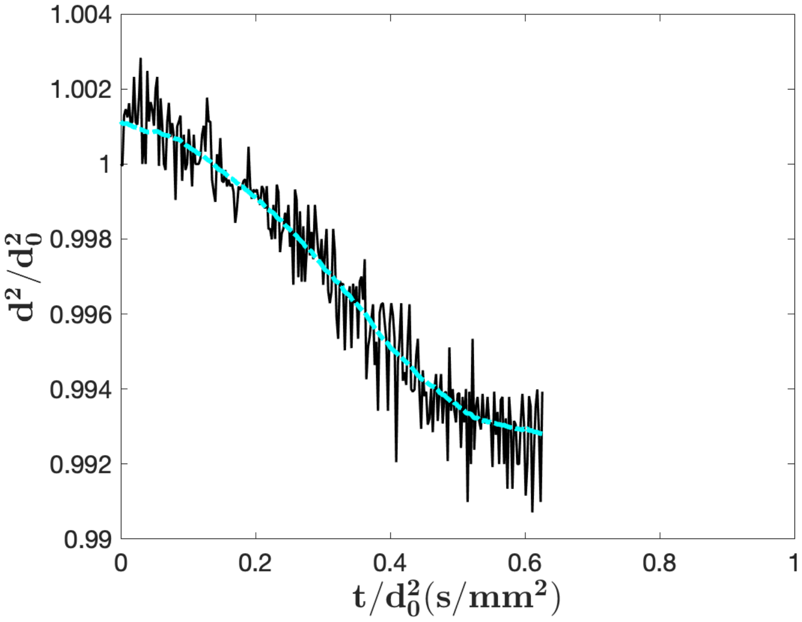

Figure 5.4: $d_0 = 3.68mm$: Time history of dimensionless squared diameter
Black solid line : measured data, Cyan dash line: Smooth data

imental d^2 trend after $d^2/d_0^2 = 0.996$. The numerical solution are shown in magenta solid line.

As mentioned previously in Section 5.3.2, the droplet surface temperature in this case is well below the boiling temperature. Therefore, the initial vapor-mass fraction is low at the droplet surface. This leads to smaller gradient for the diffusion. In addition to this, the presence of lower temperature gradient leads to longer droplet decay time. For the given data from Experiment-1, the DNS solution is observed to deviate from the analytical as well as experimental results as shown in zoomed-in plot. Though, the difference in magnitude of d^2/d_0^2 is of the order 10^{-5}, it could be due to initial transient droplet heat-up. This will be further investigated in future. To compare this quantitatively over a relatively longer period of time, an extrapolated linear trend line (magenta dash line) is fitted to DNS solution is shown in Fig. 5.5. The slope of the trend line is computed and tabulated in Table 5.3. The

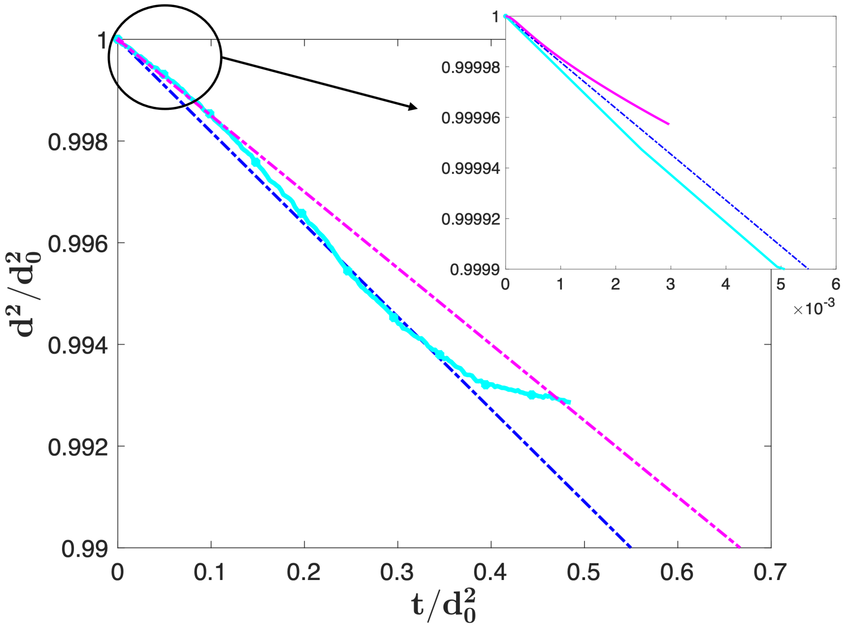

Figure 5.5: $d_0 = 3.68mm$: Time history of dimensionless squared diameter,
Cyan solid line: Smooth experimental data, Blue dash line: Analytical solution, Magenta solid line : DNS solution, Magenta dash line : Linear trend line

time required for droplet to decay from $d^2/d_0^2 = 1$ to $d^2/d_0^2 = 0.99$ is also listed in this table.

Experiment-1	Evaporation coefficient (mm^2/s)	droplet lifetime (s) till $d^2/d_0^2 = 0.99$
Experimental	1.79×10^{-2}	0.550
Analytical	1.82×10^{-2}	0.549
Numerical	1.57×10^{-2}	0.667

Table 5.3: $d_0 = 3.68mm$: Evaporation coefficient (K) for all cases

Although the longer time history of the droplet for this experiment could not be obtained, the DNS solution set match reasonable well with the given dataset. The droplet decay time observed in DNS (computed from extrapolation) is $\approx 22\%$ higher than Experiment-1.

5.4.2 Validation against Experiment-2 [61]

This section covers the comparison of DNS results against analytical solution and experimental results from Murakami et al. [61]. Fig. 5.6 shows the normalized squared diameter (d^2/d_0^2) variation with normalized time (t/d_0^2) obtained from three different approaches. The analytical solution in blue dash line is observed to match well with normalized d^2 distribution obtained from experiments in cyan solid line with markers till $d^2/d_0^2 \approx 0.5$. The experimental results deviate from analytical solution near the end of the droplet lifetime. In case of DNS results, an unsteady behavior of d^2/d_0^2 is observed in the beginning of droplet evaporation from $t/d_0^2 = 0 - 0.01\ s/mm^2$. The DNS solution (solid magenta line) is seen to have a higher slope for this time duration and therefore a higher evaporation coefficient. However, after the transient period of droplet heat-up, DNS solution exhibit nearly the same slope as analytical solution. Moreover, the extrapolated DNS results shown in dashed magenta line slightly under-predict the slope (evaporation coefficient), hence yield a slightly higher droplet decay time. A similar observation was also found in validation work by Zhang [120]. Furthermore, the extracted evaporation coefficients and the droplet lifetimes are reported in Table 5.4. The droplet lifetime for analytical solution is close to the experimental value of it.

Experiment-2	Evaporation coefficient (mm^2/s)	droplet lifetime (s)
Experimental	2.804×10^{-1}	3.56
Analytical	2.663×10^{-1}	3.75
Numerical	2.483×10^{-1}	4.02

Table 5.4: $d_0 = 0.375mm$: Evaporation coefficient (K) for all cases

5.5 Effect of Droplet Shape Under Natural Convection

This section will cover the interaction of droplet shape and the flow development around it. The droplet shape is primarily governed by surface tension and droplet diameter. The strength of buoyancy driven flow is governed by temperature/density gradient and gravity field. Therefore, to study this interaction, relevant non-dimensional numbers such as Eötvös number in Eq. (5.2) and Grashof number in Eq. (5.1) will be varied by modifying the surface tension, temperature gradients and/or gravity.

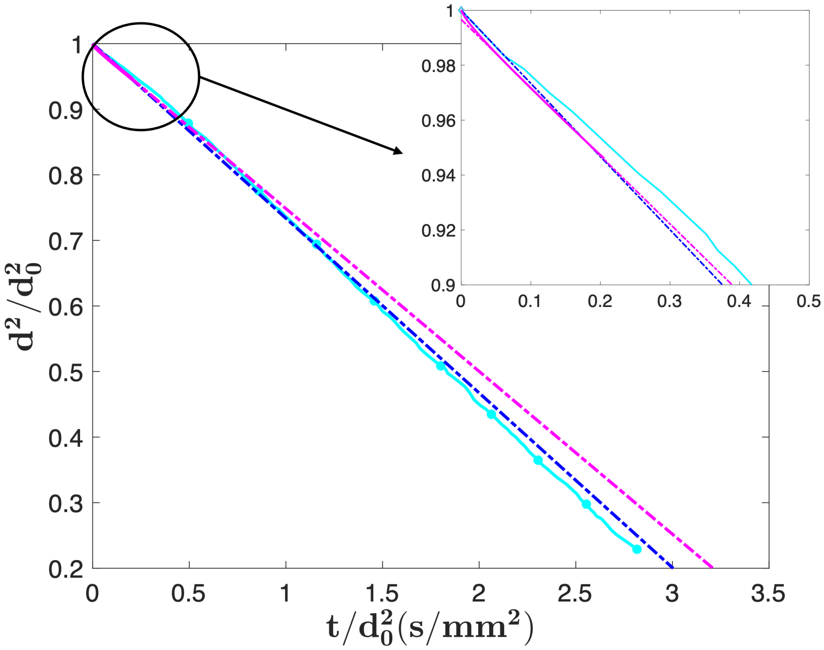

Figure 5.6: $d_0 = 0.375mm$: Comparison of time history of dimensionless squared diameter *Cyan solid line with markers : Experimental data [61], Blue dash line: analytical solution, Magenta solid line: Numerical solution, Magenta Dash line : Linear trend line*

5.6 Discussion and Future Work

This work covers the validation of the numerical results for droplet evaporation under buoyancy driven flow against the experimental and analytical solutions. The framework utilized for this study is based on Interface-capturing direct numerical simulation approach for solving evaporating/boiling flows. To simulate the buoyancy driven flow, the density of gas and liquid phase vary based on Bousinessq approximation as equation of state and is incorporated in our incompressible solver.

To cover a range of evaporation conditions, two test cases of droplet evaporation are simulated and compared against the experimental results performed under micro-gravity. First test case involves the evaporation of n-decane droplet of relatively larger size ($d_0 = 3.68\ mm$) under quiescent ambient air conditions. The second test case involves the evaporation of droplet of $d_0 = 0.375\ mm$ under quiescent pressurized ambient environment [61]. These cases cover the range of evaporation velocities (Stefan flow velocity) throughout the droplet lifetime.

The numerical results for evaporating droplets are quantified in terms of normalized squared diameter (d^2/d_0^2), the evaporation coefficient (K) and the total droplet decay time. In case of droplet evaporation under low temperature and low pressure conditions (Experiment-1), the slope of d^2 trend is lower than the experiment and it deviates from the experimental and anlytical solution. Therefore, the droplet decay time to reach $d^2/d_0^2 = 0.99$ is 22% higher in DNS solution. The authors intend to investigate the cause of such deviation further in the future work. On the other hand, the DNS results for droplet evaporation under high pressure, high temperature conditions are found to be in better agreement with the experimental results from Murakami et al. [61].

Based on this validation, we intend to use the solver to investigate the effect of natural convection and droplet shape on evaporation by varying the relevant non-dimensional numbers, i.e. Grashof number and Eötvös number respectively which will be covered in Section 5.5. The insights from these results can help us understand the complex relationship in the strength of natural convection, droplet shape, and their combined effect on the boundary layer development. Furthermore, this approach can be utilized for the exploration on the droplet evaporation under partial gravity environment.

Chapter 6

Combustion of Deformable Droplet Under Forced Convection

The work covered in this chapter is a compilation two papers, one : a peer-reviewed conference article at IMECE (2022) [94] and two: a peer-reviewed journal article in ASME journal of heat and mass transfer (2023) [91]. Complete article details are as follows,

- Meha Setiya and John Palmore Jr. Combustion and vaporization of deformable fuel droplets using direct numerical simulation. International Mechanical Engineering Congress and Exposition, 2022. doi:10.1115/IMECE2022-94475.
- Meha Setiya and John Palmore Jr. Combustion and evaporation of deformable fuel droplets. ASME Journal of Heat and Mass Transfer, 2023. doi:10.1115/1.4062784

6.1 Introduction

This chapter covers the droplet combustion under convective flow conditions. Due to higher volumetric contribution of the larger droplets in spray mass, this study extends on the combustion of these large droplets. Due to the turbulent and convective flow conditions inside the combustion chamber, the droplet shape is governed by the aerodynamic stresses and surface tension at the liquid-gas interface [24]. This can be written in terms of a non-dimensional number, Weber number ($We = \frac{\rho_G {U_\infty}^2 d_0}{\sigma}$) which is a ratio of these two forces. In the case of the small droplets, they will have higher surface tension due to higher curvature and small Weber numbers. Hence, they tend to remain in a nearly spherical shape. However, the larger spray droplets will have a higher Weber number and therefore higher tendency to deform.

Significant experimental as well as numerical work exists on the combustion of "spherical droplets" [41, 44, 74, 76, 115]. However, there is a dearth of literature on involving "deformable droplets". As the shape of a droplet is one of the parameters can alter the flow development around the droplet and hence can affect its combustion. Therefore, it is important to address this gap. In effort to address this gap, this paper reviews the major past work on evaporation of deformable droplets first, followed by combustion studies.

Recent analytical studies by Tonini and Cossalli [105, 106] suggested that the iso-volume spheroidal droplets (prolate and oblate) evaporate differently in comparison to spherical droplet. The local flux was found to be proportional to surface curvature under the stagnant gas environment. Furthermore, the results of analytical study using perturbation theory by Palmore [67] demonstrated the freely deformed droplets has higher evaporation rate in comparison to isovolume spherical droplet. Although, the surface area is higher for deformed droplet, the total evaporation rate of a non-spherical droplet does not scale by the ratio of surface areas times the evaporation rate of spherical droplet. At low Reynolds number (nearly quiescent flow conditions), the non-dimensional total evaporation rate given by Equation 72 in [67] suggests that, it has a complex relationship with the droplet shape (Liquid-Gas interface) governed by Weber number. It was also shown that the deformation of the droplet as represented by Weber number, enhances the combustion rate by increasing the rate of fuel evaporation. This alters the distance of the flamesheet from the droplet surface and hence, it changes the entrainment of ambient gas between flamesheet and droplet surface. However, the results from his work were limited to combustion in stagnant air ($Re = 0$). One of our recent work on pure evaporation of freely deforming droplets under convective flow in [95] demonstrated that surface averaged total evaporation rate is higher for the deformed droplets than the spherical droplets. This enhancement is associated with the local curvature in the front region and wake flow interaction with the droplet. Both these parameters are related to droplet shape.

In case of combustion in a stagnant flow, many experimental studies such as work by Xia [116] and Pacheo et al. [64] focused on analyzing the dynamics and chemistry of spherical diffusion flames. A relatively larger droplet size was chosen in the range of 100 μm to 10 mm for the majority of the experimental work as they generally try to mimic the initial Reynolds numbers (Re_0) as seen by the real spray droplets. However, matching Re_0 with the larger droplets in experiments mean slower inflow velocities, hence lower Weber numbers. Therefore, the droplet shape is nearly spherical.

A few experimental studies on the burning of fuel particles such as [27, 28, 29, 76, 88] covered the burning under a convective flow. The effect of natural convection on high pressure droplet combustion was studied by Sato et al. [88]. For pressure below critical pressure of liquid fuel, the burning time decreases and above critical pressure, burning time increases. The presence of natural convection affects the heat and mass transfer across the flame.

Gokalp et al. [27] conducted low temperature droplet burning under normal and reduced gravity conditions under natural and forced convection. They found that the assumption of spherical flame no longer holds for convective conditions. Moreover, due to presence of silica filament to hold the droplet, the droplet shape was closer to an ellipsoid than a sphere in their experiment. The burning rates or surface regression rates using d^2 law involved calculation of characteristic dimension based on equivalent surface area or volume of a sphere. However, the effect of droplet shape specifically on burning rate was not the focus of their work.

The studies by Gollahalli and Brzustowski [29] suggested that the flow conditions drive the nature of the diffusion flame, either an envelope flame or a wake flame or transitioning from envelope flame to wake flame. Such flame development is sensitive to thermophysical properties of ambient gas as well as its inflow velocity. If the inflow velocity is lower than a critical value, envelope flame will be seen. If the gas velocity is higher than a critical value, the wake flame will be observed. Moreover, a sudden drop in evaporation rate was observed when transitioning from envelope flame to wake flame.

Raghvan et al. [76] studied the effect of ambient temperature on the burning rates for different inflow velocities and various flame shapes were observed. On the similar lines, a numerical study by Wu and Sirignano [115] on transient burning of n-octane was performed at high temperature and 20 atm pressure air stream. Specifically, the transient shape of flame, surface temperature and burning rates were studied at different initial Reynolds numbers $Re_0 = \rho_\infty U_{rel} d_0/\mu_\infty$ and initial Damköhler numbers (Da_0) for $d_0 = 50\ \mu m$. The initial Damköhler number is defined as the ratio of reaction rate and convective transport rate.

$$Da_0 = \frac{d_0/U_\infty}{\rho_\infty Y_F^0/\dot{\omega}_0 W_F} \tag{6.1}$$

The results showed that, for given flow conditions, if an envelope flame is observed, it is going to stay an envelope flame through the lifetime of the droplet. However a wake flame can either transition to an envelope flame at the later of lifetime of droplet or can extinguish. This numerical study suggested a critical initial $Da_0 = 1.02$ for n-octane at $P_\infty = 20\ atm$ and $T_\infty = 1500K$. An envelope flame is observed above at $Re_0 = 11$, $Da_0 = 1.2$ and wake flame is seen at $Re_0 = 45$, $Da_0 = 0.3$. Another numerical study by Pope and Gogos [74] analyzed the extinction of the envelope flame for various sizes of n-heptane droplet ranging from $d_0 = 0.1\ mm\ -\ 3\ mm$ at atmospheric pressure and varying temperature conditions. For smaller droplets of $d_0 < 0.1\ mm$, the extinction velocity was found to be proportional to $d^{0.5}$ and the correlation involving Da_0, Re and transfer number B was developed. It is important to note that all these numerical studies were performed with the assumption of spherical (non-deforming) droplet shape under the axisymmetric flow.

Based on this literature review, the interaction of the combustion of deformable droplet under a convective flow environment is not yet unknown. Hence, this work covers the impact of droplet shape on its pure evaporation and combustion under convective flow of moderate Reynolds number using DNS. The droplet shape is varied by modifying the Weber number. This work is organized as follows: Section 6.2 covers the problem formulation and summarizes the flow solver details, Section 6.3 describes the numerical setup including the boundary conditions and the thermo-physical conditions of fluids, this is followed by results and discussion in Section 6.4 and conclusions in Section 6.5.

6.2 Problem Formulation

In the current problem, the combustion of an isolated fuel droplet of n-decane is studied. The initial droplet diameter is $d_0 = 100\ \mu m$. The details of flow solver and combustion mechanism are discussed here.

6.2.1 Flow Solver

This work uses a numerical framework developed in [69] for the analysis of the given problem. This is briefly discussed in Section 2.2, therefore not repeated here. In addition to this, combustion mechanism used for this work is elaborated here.

6.2.2 Combustion Mechanism

A single-step mechanism [114] is used for the combustion of the droplet. Five chemical species in total are solved in gas phase, namely fuel (F), oxygen (O_2) as oxidizer, nitrogen (N_2) and products of combustion, water (H_2O), and Carbon dioxide (CO_2).

$$\mathrm{C_{10}H_{22}} + 15.5\ \mathrm{O_2} \longrightarrow 10\ \mathrm{CO_2} + 11\ \mathrm{H_2O} \tag{6.2}$$

The sum of all species mass fraction sums to unity.

$$\sum_i Y_i = 1 \tag{6.3}$$

Nitrogen is an inert gas and does not participate in combustion. Hence, the species mass fraction of Nitrogen (Y_{N_2}) will be computed as:

$$Y_{\mathrm{N_2}} = 1 - (Y_F + Y_{\mathrm{O_2}} + Y_{\mathrm{CO_2}} + Y_{\mathrm{H_2O}}) \tag{6.4}$$

Therefore, only 4 species need to be solved inside the gas phase.

Burning of the fuel produces heat due to combustion and its value is $\Delta h_c = 44602\ [kJ/kg] = 6305300.0\ [J/mol]$ for n-decane. The fuel consumption rate ($\dot{\omega}_F$) depends on the temperature and pressure of ambient oxidizer and the species mass fraction of fuel (Y_F) and oxidizer (Y_{O_2})

and is defined as:

$$\dot{\omega}_F = W_F \times (-A\ e^{-E_a/R_u\ T_\infty}[\rho^*\ Y_F/W_F]^{0.25}[\rho^*\ Y_{\mathrm{O_2}}/W_{\mathrm{O_2}}]^{1.5}) \tag{6.5}$$

Here, negative sign associated with $\dot{\omega_F}$ is due to consumption of the fuel. The molecular weight of fuel is $W_F = 0.0142\ [kg/mol]$ and the unit for $\dot{\omega}_F$ is $[kg/(m^3 \cdot s)]$. The pre-exponent factor $A = 12016655\ [(mol/m^3)^{1-m-n} 1/s]$, where $m = 0.25,\ n = 1.5$. The activation energy required for the combustion to take place is $E_a = 125520.0\ [J/mol]$, $R_u = 8.314\ [J/(mol \cdot K)]$ is universal gas constant.

The gas phase density ρ^*_G used in combustion calculations takes account of mixture properties. It is calculated using ideal gas law and mixture properties as expressed in Eq. (6.6).

$$\rho^*_G = \frac{P_\infty}{R_u T_\infty (\sum_i Y_i/W_i)} \tag{6.6}$$

It is worth highlighting that ρ^*_G is different from ρ_G which is a constant reference gas density. Similarly to Eq. (6.5), the oxidizer consumption rate, production rate of water and carbon dioxide can be written as:

$$\dot{\omega}_{\mathrm{O_2}} = (W_{\mathrm{O_2}}/W_F) \times (15.5 \times \dot{\omega_F}) \tag{6.7a}$$

$$\dot{\omega}_{\mathrm{H_2O}} = (W_{\mathrm{H_2O}}/W_F) \times (-11 \times \dot{\omega_F}) \tag{6.7b}$$

$$\dot{\omega}_{\mathrm{CO_2}} = (W_{\mathrm{CO_2}}/W_F) \times (-10 \times \dot{\omega_F}) \tag{6.7c}$$

Moreover, the temperature production term can be written as

$$\dot{\omega}_T = -W_F \times \left(\frac{\Delta h_c\ \dot{\omega_F}}{\rho_\infty c_{p_G}} \right) \tag{6.8}$$

As the combustion timescale is much faster than the fluid timescales, advancing the flow using combustion timescale would make the solution computationally intractable. Hence, a segregated timestep advancement model is used. At each time step, a stiff integrator is used to integrate the chemical reaction sources assuming the fluid flow is stagnant. Then the integrated sources are coupled into the fluid and scalar transport equations. This strategy is common in the combustion simulation community, hence not explained in detail here. More details on our implementation of the idea can be found in our previous works [66].

This numerical framework has been validated for pure evaporation under stagnant in [68] and in convective flow [95].

6.3 Numerical Setup

The numerical setup for this problem includes an isolated droplet located at the center of the domain. This study improves on previous numerical studies by not imposing any droplet shape such as sphere or ellipsoid. Instead the droplet freely deforms based on the aerodynamic forces it experiences. The initial droplet diameter is $d_0 = 100\ \mu m$ and it is located at the center of the domain.

The domain size is $30d_0 \times 30d_0 \times 30d_0$ for these studies. A structured non-uniform grid is used for these studies. The dimension of uniform grid region are $30d_0 \times 10d_0 \times 10d_0$ and beyond this region, a stretch ratio of 1.09 is applied in order to optimize the computational accuracy and expense as shown in Fig. 6.1. The grid size in the uniform grid region is $dx = dy = dz = 5 \times 10^{-6}\ m$. Based on the analytical calculation for vapor film thickness around a non-evaporating sphere in convective flow [3], this grid resolution leads 10 cells to cover the vapor film around the droplet which is sufficient to resolve the thermal and vapor film thickness. It is important to note that the domain size is selected such a way that boundaries do not influence the flow around droplet.

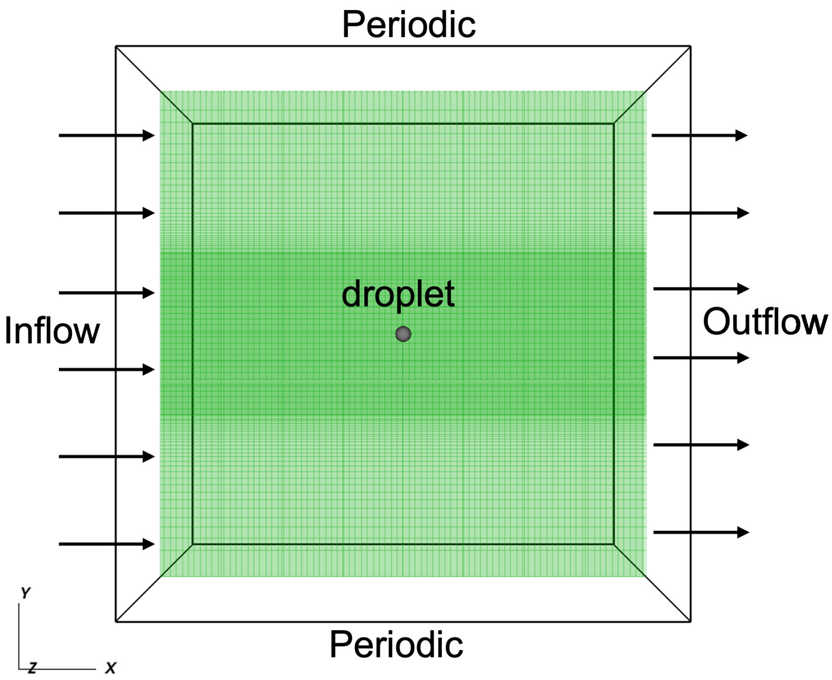

Figure 6.1: A sketch of numerical setup and boundaries

As shown in Fig. 6.1, a fixed inflow boundary condition is applied on the left face of the domain. The right face is used as a convective outflow. The remaining boundaries in y and z directions are treated as periodic. In order to keep the droplet at its predetermined location through out the simulation, "gravity update" method is used. This method mimics the flow over a freely-deforming droplet falling at its terminal velocity. The artificial gravity on the droplet is applied in feedback loop manner in order to accommodate the droplet center shift in time. This method is seen to be effective in minimizing the droplet shift. More details of this can be found in our previous work [50, 92].

The ambient conditions for the numerical studies are $P_\infty = 20\ atm$ and high temperature $T_\infty = 1400\ K$ [115]. The droplet is at its saturated conditions. It evaporates and burns in a convective flow with $Y_{\mathrm{O_2}} = 0.23$, $Y_{\mathrm{F}} = 0$, $Y_{\mathrm{N_2}} : 0.77$, and $T = T_\infty$ at inlet. Reynolds number based on the initial diameter, defined as $Re_0 = \rho_\infty U_{rel} d_0/\mu_\infty$, here U_{rel} is the relative velocity of oxidizer ; $U_{rel} = U_\infty - U_{drop}$. As the droplet stays in the center of the domain, U_{drop} is negligible and hence, for a constant inflow velocity, U_{rel} does not change significantly. $Re_0 = 25$ is considered for these studies as the flow over sphere at this Re_0 is nearly attached [101]. To study the effect of deformation, the initial Weber number $We_0 = \rho_\infty U_{rel}^2 d_0/\sigma$ is varied by modifying the surface tension of liquid. The range for Weber number is $We_0 = 1 - 12$. The upper limit of $We_0 = 12$ is imposed due to the droplet breakup beyond this value [54]. The liquid properties refer to fuel properties and are taken at boiling temperature $T_L = 615\ K$ at $P_\infty = 20\ atm$ [1, 118] and gas properties refer to air and are taken $P_\infty = 20\ atm$ and $T_\infty = 1400\ K$ as mentioned in Section 6.3.

Property	Air	Fuel
Temperature (T)	1399.99	614.05
Density (ρ)	5.04	300.00
Viscosity (μ)	5.05×10^{-5}	4.00×10^{-4}
Specific heat (c_P)	1097.28	–
Thermal conductivity (k)	0.087	0.079
Latent heat of vaporization (h_{fg})	–	48126
Adiabatic flame temperature (T_{ad})	–	2286

Table 6.1: Fluid properties at $P_\infty = 20\ atm,\ T_{boil} = 615\ K,\ T_G = 1400\ K$

6.3.1 Analytical Calculation of Gas Temperature

The solver uses the Bounded Quadratic Upwind Interpolation for Convective Kinematics (BQUICK) algorithm for advective scalar transport [35]. The algorithm is designed to ensure that transported scalars remain strictly bounded between a given minimum and maximum value. For the species mass fraction, the natural choice for these bounds are 0 and 1. For the temperature, the minimum temperature of 600 K is selected which is lower than the boiling temperature of the droplet. The highest temperature in this process is the flame temperature due to burning. To evaluate the flame temperature analytically for the given ambient conditions, a simple 1-D droplet burning model is used [108]. The results of the model are demonstrated in Fig. 6.2. Moving outward from the droplet surface, the temperature increases rapidly towards a peak value, which can be identified as the flame temperature. The temperature then decreases smoothly with increasing distance from the droplet surface.

Various local equivalence ratio exist during the combustion process, hence the flame temperature will be function of the equivalence ratio is defined as $\phi = (A/F)_{st}/(A/F)$. Here (A/F) is the actual air to fuel ratio whereas $(A/F)_{st}$ is the stoichiometric ratio $(A/F)_{st} = 15$. For the flammability limits $\phi_L = 0.8$ and $\phi_U = 1$ for a diffusion flame [76], we found that the flame temperature varies from $\sim 3200 - 3660K$ as shown in Fig. 6.2. Though it is an oversimplified model, this 1-D calculation helps in estimating the highest temperatures that may be observed in the numerical simulations and use an appropriate initial maximum temperature accordingly. With a great amount of margin, the maximum domain temperature is taken as $5000K$ for these studies.

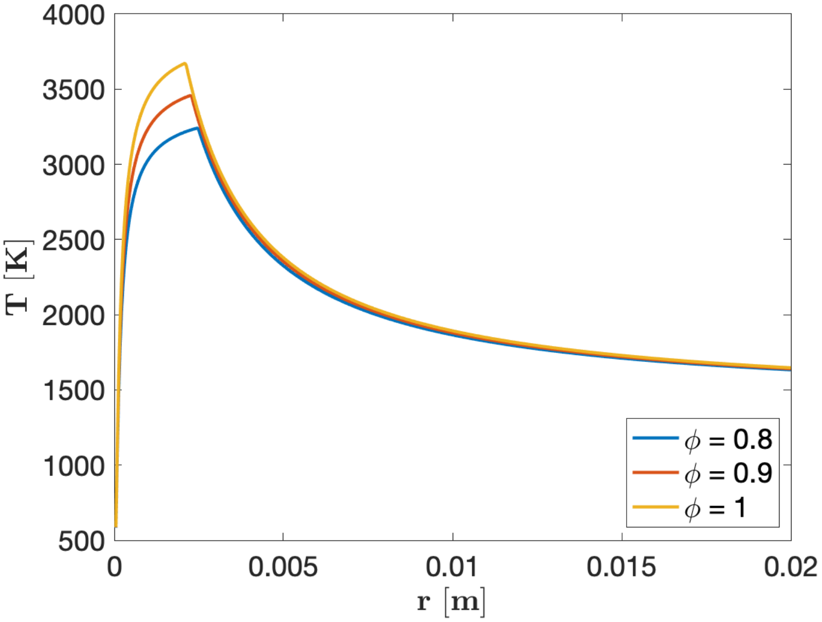

Figure 6.2: Simple droplet burning model: Temperature variation in the radial direction [108]

6.4 Results and Discussion

6.4.1 Effect of Droplet Shape on Pure Evaporation and Combustion

As the combustion process is limited by the evaporation rate of liquid fuel, it is important to study the effect of droplet shape on pure evaporation first under the given ambient conditions. As the droplet shape is governed by its initial Weber number, two cases with $We_0 = 1$ and $We_0 = 12$ are studied at $Re_0 = 25$ for given ambient conditions. The droplet is initially spherical in shape and eventually deforms freely due to the imbalance of forces.

To quantify the effect of droplet shape on pure evaporation and combustion, total evaporation rate ($\dot{m}$ $[kg/s]$) is plotted in Fig. 6.3. The results show time history of surface averaged total evaporation rate over time for both pure evaporation and combustion. The time on x-axis is normalized using a capillary response time (τ_p) for droplet which is defined as

$$\tau_p = \sqrt{\frac{\rho_L + \rho_G}{\sigma}} \left(\frac{d_0}{2\pi}\right)^{3/2} \tag{6.9}$$

In these results, the instantaneous evaporation rate starts at zero and rapidly increases. Since the droplet is preheated to the saturation temperature, this period is due to the adjustment of the gaseous flow field around the droplet. After a small period of time, $\dot{m}$ reaches a steady value for both pure evaporation and combustion cases. In terms of effect of Weber number on $\dot{m}$ at this Re_0, the pure evaporation cases have slightly higher value of $\dot{m}$ for higher Weber number, whereas in case of combustion $We_0 = 12$ show significantly higher $\dot{m}$. An increase of 4.85% is seen at time instant $t/\tau_p \sim 7$. This enhancement increase with time and reaches upto $\sim 9\%$ at $t/\tau_p \sim 15$ as shown in the zoomed-in plot. Moreover, $We_0 = 1$ combustion case have 11.8% higher $\dot{m}$ when compared with pure evaporation. This is due to overall higher temperature of ambient gas around the droplet due to combustion.

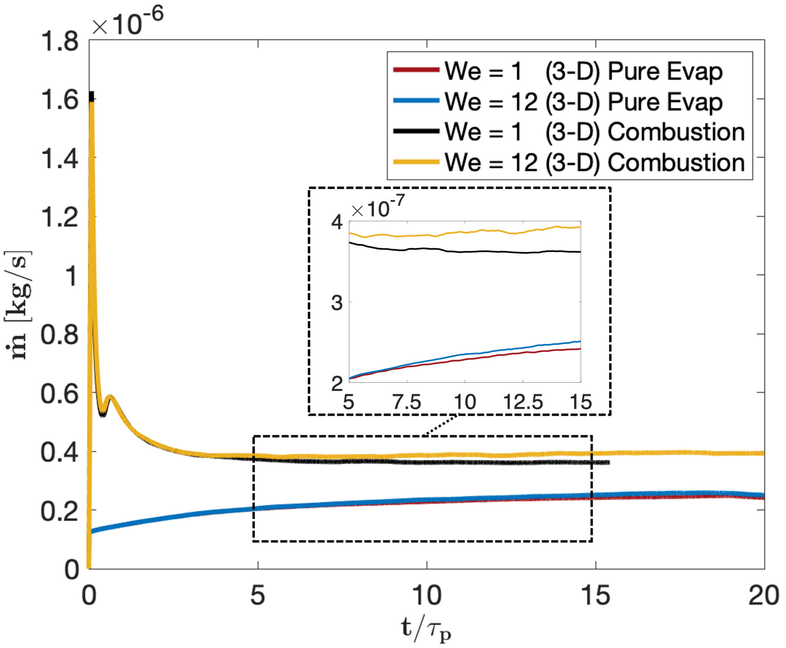

Figure 6.3: Total evaporation rate $[kg/s]$ with t/τ_p at $Re_0 = 25$

Since, these studies involve evaporation (or burning), hence both liquid volume and surface area decrease with time. Therefore, the net effect of the local evaporation flux ($\dot{m}''$) and the total surface area (A) on the total evaporation rate ($\dot{m} = \dot{m}'' \times A$) can be misleading. In order to dissociate the effect of total surface area on $\dot{m}$, these studies are performed where the liquid volume is kept constant artificially while still solving the remaining equations for the fluid dynamical system.

To breakdown the contribution of evaporation flux and surface area in total evaporation rate, Fig. 6.4 and Fig. 6.5 show the time history of surface averaged local $\dot{m}''$ and normalized area A/A_0 respectively. In case of pure evaporation, the averaged value of $\dot{m}''$ for $We_0 = 1$ is nearly the same as $We_0 = 12$. The same is observed for combustion cases but with the higher magnitude of $\dot{m}''$. This suggest weak dependency of Weber number on averaged $\dot{m}''$

at this Re_0.

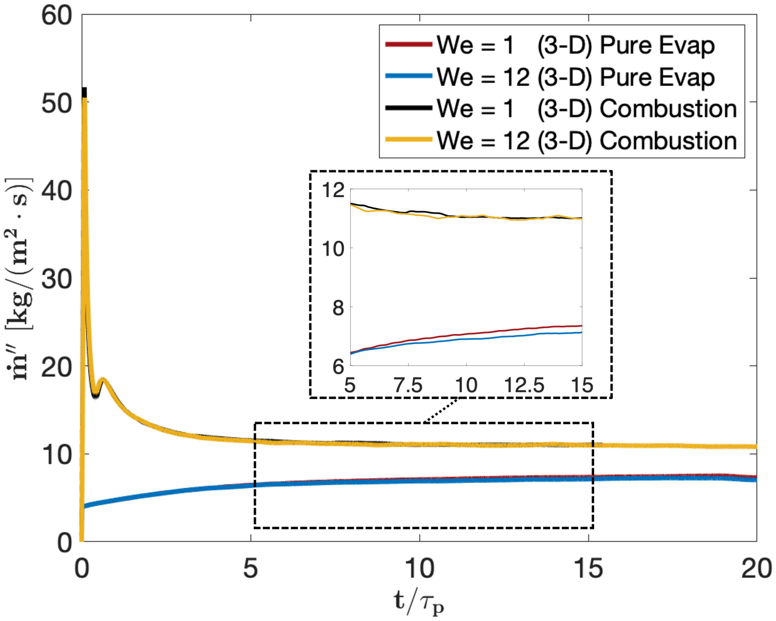

Figure 6.4: Local evaporation rate $[kg/m^2 \cdot s]$ with t/τ_p at $Re_0 = 25$

Due to the presence of convective flow, the droplet deforms. This deformation can be quantified in terms of A/A_0 as shown in Fig. 6.5. Here A_0 is initial droplet surface area. The results show a nearly linear increasing trend with time. This rise in A/A_0 is seen to be faster in the beginning of the evaporation which suggest higher deformations till $t/\tau_p \sim 10$. The slope of A/A_0 reduces at later time and A/A_0 reaches nearly a steady value. Moreover, A/A_0 is higher for $We_0 = 12$ when compared with $We_0 = 1$ for each case. For example: at a time instant $t/\tau_p \sim 7$, $We_0 = 12$ with combustion has 5.4% higher total surface area when compared to $We_0 = 1$. This increase in area for $We_0 = 12$ pure evaporation case is 2.7%. One important observation in normalized area plot is that the trend of A/A_0 for a particular Weber number is same for both pure evaporation and combustion. They both differ by the magnitude of area ratio.

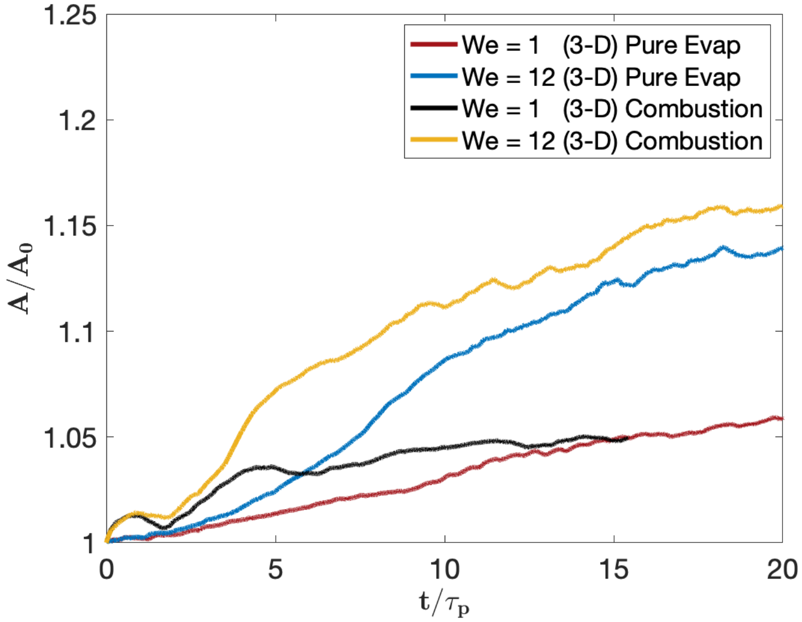

Figure 6.5: Normalized total surface area with t/τ_p at $Re_0 = 25$

These trends in A/A_0 reflect into droplet shape change. Although surface averaged values of $\dot{m}''$ are nearly the same as seen in Fig. 6.4, the droplet shape affects the distribution of local evaporation flux because of interaction between the droplet and inflow. To visualize these results, Fig. 6.6 shows the pseudocolors of local evaporation flux ($\dot{m}''$ $[kg/(m^2 \cdot s)]$) at time instance $t/\tau_p \sim 7$. The droplet shape at $We_0 = 1$ is close to an ellipsoid whereas it is more deformed at $We_0 = 12$ case for both pure evaporation and combustion. In addition to that, the droplet looks further deformed in $We_0 = 12$ combustion case (Fig. 6.6d) when compared to $We_0 = 12$ pure evaporation case (Fig. 6.6b). This suggests an interaction between droplet shape and combustion dynamics.

Due to the convective flow over the droplet, the front of the droplet is exposed to hot incoming air. This leads to higher local flux in front of the droplet. Moreover, the distribution of $\dot{m}''$ in this region depends on the curvature of droplet. Now, while comparing the effect of Weber number for combustion cases in front of the droplet, higher $\dot{m}''$ is observed in $We_0 = 12$

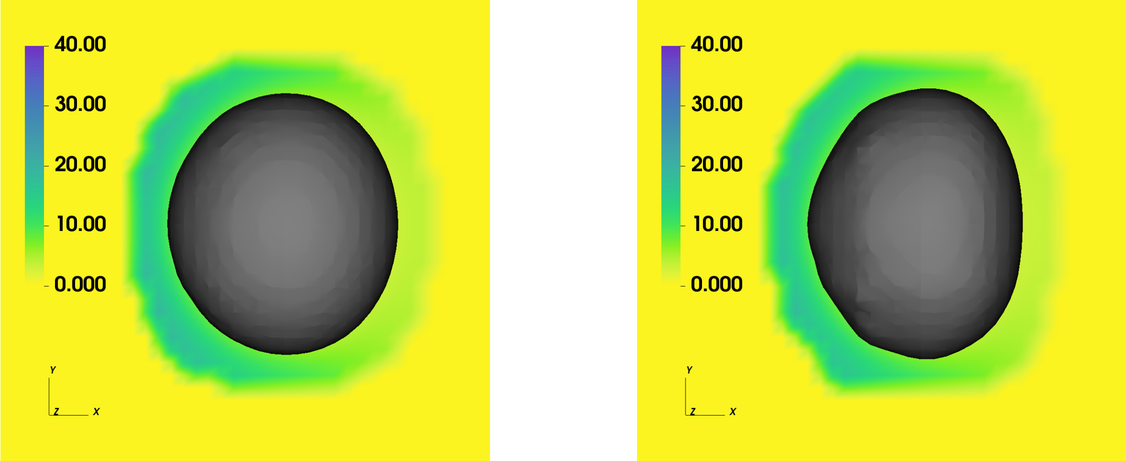

(a) $We_0 = 1$: Pure Evaporation (b) $We_0 = 12$: Pure Evaporation

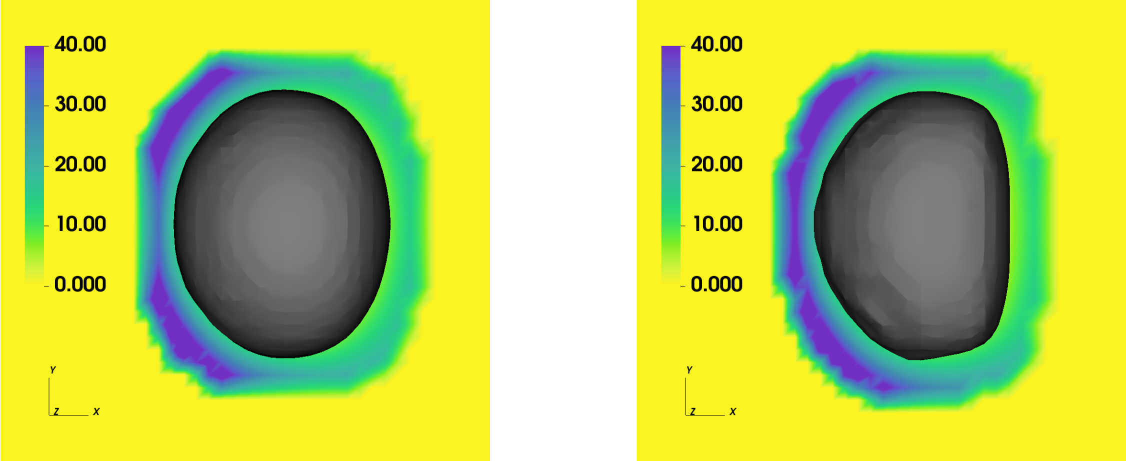

(c) $We_0 = 1$: Combustion (d) $We_0 = 12$: Combustion

Figure 6.6: Psueodcolors of local evaporation flux $[kg/(m^2 \cdot s)]$ at $t/\tau_p \sim 7$ at $Re_0 = 25$

due to the presence of higher curvature when compared to $We_0 = 1$ as shown in Fig. 6.7. The curvature is normalized using curvature of a sphere of diameter d_0. The values for $\dot{m}''$ measured near to the front stagnation point are 41.5 $kg/(m^2 \cdot s)$ and 51.6 $kg/(m^2 \cdot s)$ for $We_0 = 1$ and $We_0 = 12$ respectively. This observation is consistent with the previous studies showing that $\dot{m}''$ is directly proportional to the interface curvature at least in regions where the boundary layer is fully attached [106],[67]. This was also observed in our previous work [95], [94].

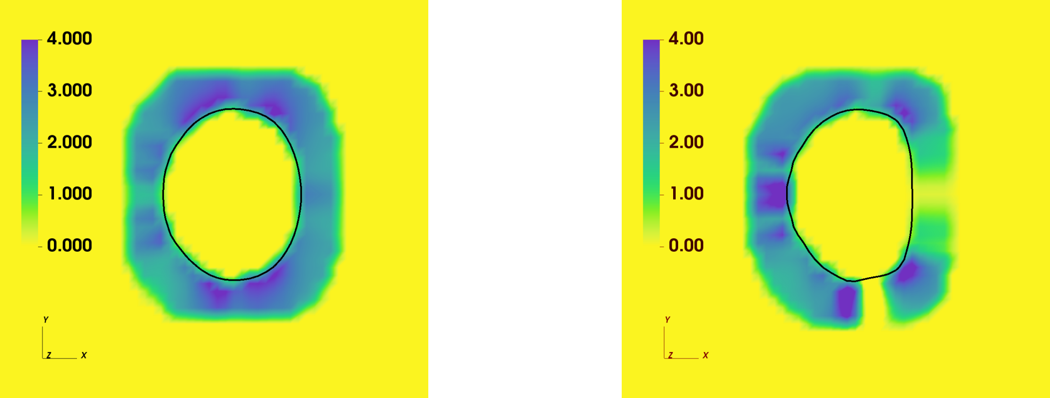

(a) $We_0 = 1$: Combustion

(b) $We_0 = 12$: Combustion

Figure 6.7: Psueodcolors of normalized curvature at $t/\tau_p \sim 7$ at $Re_0 = 25$ *Black line marks the liquid-gas interface.*

Effect of droplet shape on flame

As the auto-ignition temperature for n-decane is 481 K, for the given ambient conditions, the droplet starts burning and the envelope flame appears fairly early in time. This type of flame occurs due to faster reaction rates in comparison to convective transport. Initial Damköhler number at $Re_0 = 25$ and for these ambient conditions is higher than critical value ($Da_0 > 1.02$) as reported in [115]. One way of locating such flame is where stoichiometric combustion of the fuel and oxidizer occurs [98]. This can be defined as a variable $\beta = Y_\mathrm{F} - Y_{\mathrm{O}_2}/(A/F)_{st}$. Hence, $\beta = 0$ marks the location of the flame. Another way of marking the flame location is to plot the contour of maximum species mass fraction for products such as CO_2 and H_2O.

To evaluate the effect of Weber number on the combustion, Fig. 6.8 shows the gas temperature around the droplet along with the contour of maximum species mass fraction of CO_2 ($max\ Y_{\mathrm{CO}_2}$ - marked in yellow line). The flame is pushed towards the droplet and no longer stays as spherical diffusion flame. The gas temperature in the droplet vicinity is significantly lower in comparison to temperature in the flame region due to cooler fuel vapor. The region of maximum temperature lies where fuel vapor meets with oxidizer. This region is seen to coincide with maximum Y_{CO_2} marked with yellow lines for each case.

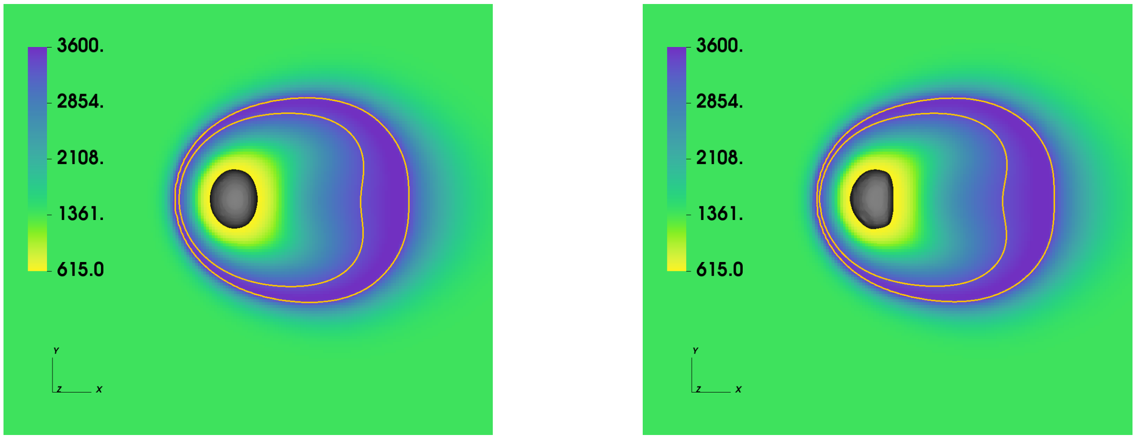

(a) $We_0 = 1$ (b) $We_0 = 12$

Figure 6.8: Psuedocolors of gas temperature $[K]$ at $Re_0 = 25$ at $t/\tau_p \sim 7$.
Yellow line marks the maximum Y_{Co_2}

In terms of comparison between different Weber numbers, same magnitude of maximum gas temperatures as well as maximum Y_{CO_2} are observed despite the changes in $\dot{m}''$ due to shape change in the front. In addition to this, the flame type is still the envelope non-spherical flame for given ambient conditions. Moreover, the contour for maximum Y_{CO_2} and distribution of gas temperature are seen to be qualitatively same for both Weber numbers. To compare the flames further Fig. 6.9 show an overlay of z-section of droplet shape and the flame marked by $\beta = 0$ for different Weber numbers.

The flame base distance (measured from the droplet center to $\beta = 0$ along negative x-direction) and flame stand-off distance (measured from droplet center to $\beta = 0$ along positive y-direction) are observed to be same for both Weber numbers. However, the flame length behind the droplet (measured from the center of the droplet to end of the flame in flow direction) is seen to be longer for $We_0 = 12$. The evaporation in rear region of the droplet is dependent on the flow interaction in wake region which impacts the flame length behind the

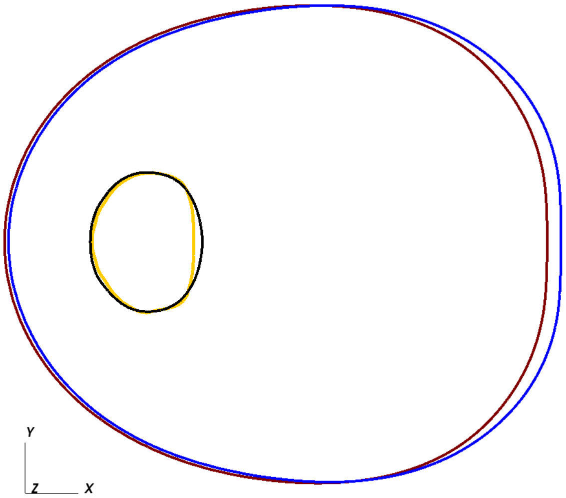

Figure 6.9: Sectional view of droplet and flame shape: $We_0 = 1$ (black) vs $We_0 = 12$ (orange), $Re_0 = 25$.
Maroon line marks flame for $We_0 = 1$ *and blue line marks flame for* $We_0 = 12$

droplet. The flow velocity measured at the end of flame is found to be higher in $We_0 = 12$. This leads to the flame location to be pushed further downstream. The values of velocity and non-dimensional flame length are tabulated in Table 6.2. Overall, combustion at $Re_0 = 25$ shows little sensitivity to the Weber number. Further analysis, however, demonstrates that in this case none of the droplets deform significantly. To further explore this effect, we introduce simulations at $We_0 = 16$ and 20 The cross-section of the droplets at different Weber numbers are overlaid in Fig. 6.10 to compare the droplet shape. These results show that the droplet dimension perpendicular to flow is nearly the same for all Weber number cases. Moreover, droplet break-up is not observed even at $We_0 = 20$ when the droplet is burning. This seems to contradict previous literature on the droplet Weber number effect, which predicts increasing deformation with increasing Weber number. In particular, Weber

Case	v $[m/s]$	$L^* = L/d_0$
$We_0 = 1$	1.65	3.06
$We_0 = 12$	1.78	3.17

Table 6.2: Measurement of flow velocity v and normalized flame length L^* at $Re_0 = 25$

number $We_0 = 12$ was reported as a critical We_0 for the onset of breakup in previous literature such as [36, 45, 54].

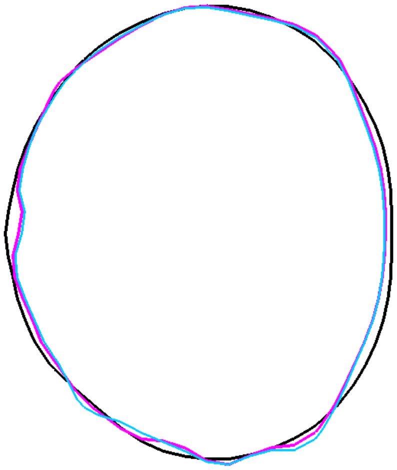

Figure 6.10: Sectional view of droplet shapes at different Weber number at $t/\tau_p \sim 10$, $We_0 = 1$ *(Black)*, $We_0 = 16$ *(Magenta)*, $We_0 = 20$ *(Cyan)*

As a result of this lack of deformation, the results all show surprisingly similar combustion behavior as $We_0 = 1$ in terms of gas temperature and species mass fraction of CO_2. The time history of gas temperature for the new cases is shown in Fig. 6.11 which suggests nearly the same gas temperature for all cases. The spatially averaged gas temperatures and species mass fraction of CO_2 (not shown here) are seen to be closely the same for all Weber numbers.

To investigate this phenomenon further, we simulated non-combusting, non-evaporating droplets at $We_0 = 16,\ 20$ and compared them against the corresponding combusting cases. A cross-section of the droplet for $We_0 = 20$ cases is compared in Fig. 6.12 at time instant $t/\tau_p \sim 10$. Smaller deformations are seen for burning droplet at the same Weber number. Moreover, the droplet break up is observed at time $t/\tau_p \sim 87,\ 81$ for $We_0 = 16$ and $We_0 = 20$ respectively for non-combusting droplet. This clearly points toward a complicated interac-

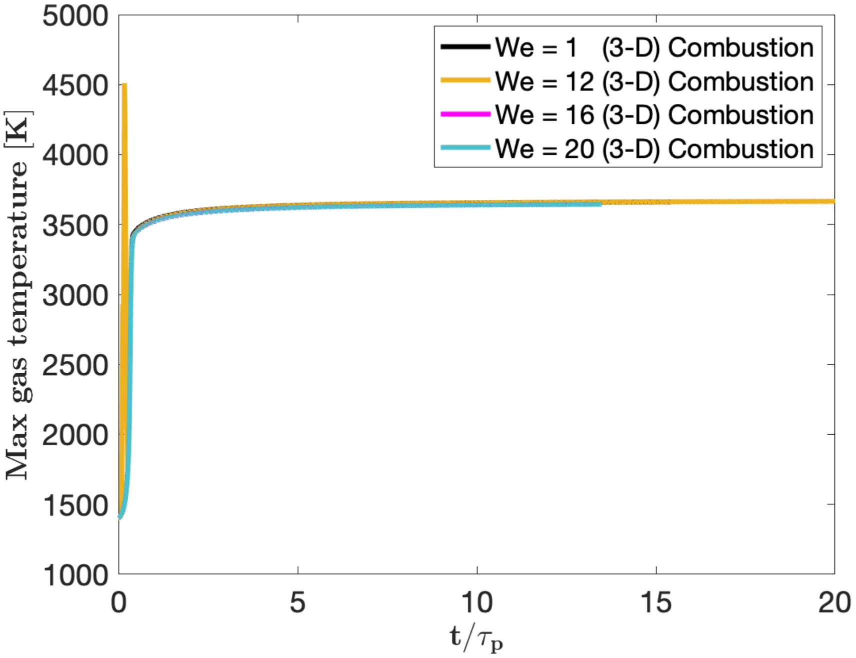

Figure 6.11: Comparison of gas temperature for different Weber numbers at $Re_0 = 25$

tion between combustion and droplet shape as the droplet never reaches to its maximum deformation while burning. It also suggests that the droplet deformation is inhibited due to higher evaporation rates in combustion case. This can also be understood from the jump condition in Eq. (2.13), where the surface tension must balance the pressure difference across the interface and the evaporation flux. For non-evaporating cases, the balance is purely between surface tension and pressure. A large curvature (κ) is required for the surface tension to balance the aerodynamic pressures from the flow around the droplet. Hence, larger deformation results to create this curvature. However, when evaporation is introduced, it works in conjunction with the surface tension to balance the pressure jump. Therefore such large deformations are not required. This is related in concept to established literature that shows the droplet break-up does not only depend on Weber number. Other conditions such as density ratio, viscosity ratio, Ohnesorge number, and ambient gas velocity affect the deformation, break-up time, and break-up mode [72, 112]. This current paper suggests that the evaporation rate is also an important factor in predicting droplet deformation and break-up.

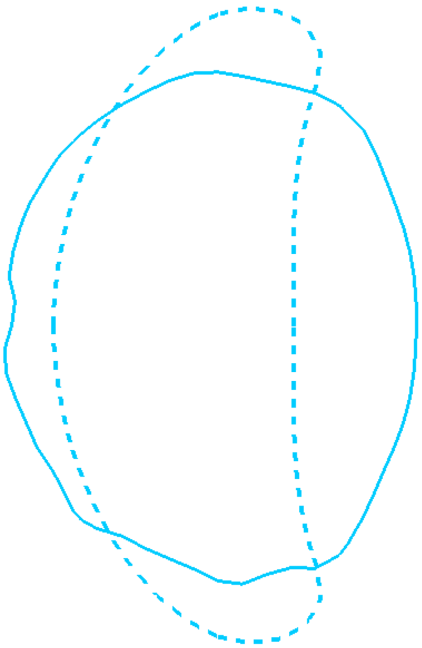

Figure 6.12: Sectional view of droplet shape at $We_0 = 20$ at $t/\tau_p \sim 10$. *//Cyan: with combustion, Cyan dashed: without combustion*

Internal Circulation

It may be expected that the rate of internal circulation inside the droplet can affect the evaporation and combustion properties. In this paper, the droplet is pre-heated, so internal circulation only affects the evaporation and combustion via changing the boundary layer development in and around the droplets. This effect was demonstrated in [70] which investigated the evaporation of multicomponent jet fuel surrogate.

Past studies on the effect of internal circulation [47, 49, 50] showed that the internal circulation can be predicted by the density ratio of two fluids (ρ_l/ρ_g). As the density ratio increases, the magnitude of internal circulation is observed to be decreasing. Therefore, higher density ratio cases demonstrated weaker internal circulation. The density ratio for the presented work is $\rho_l/\rho_g \approx 60$, so internal circulation is expected to be negligible. To demonstrate the internal motion for this study, Fig. 6.13 shows vectors of normalized liquid velocity overlaid on normalized vorticity inside droplet. The initial inflow velocity U_0 and initial droplet diameter d_0 are used for the normalization. A counter-rotating vortex pair is observed near the top and bottom of droplet in both cases. However, the overall magnitude of normalized liquid velocity remains low ($\leq 7.5\% U_\infty$) in both cases. Therefore, the effect of such internal motion is not expected to be significant. This agrees well with the observations in [49].

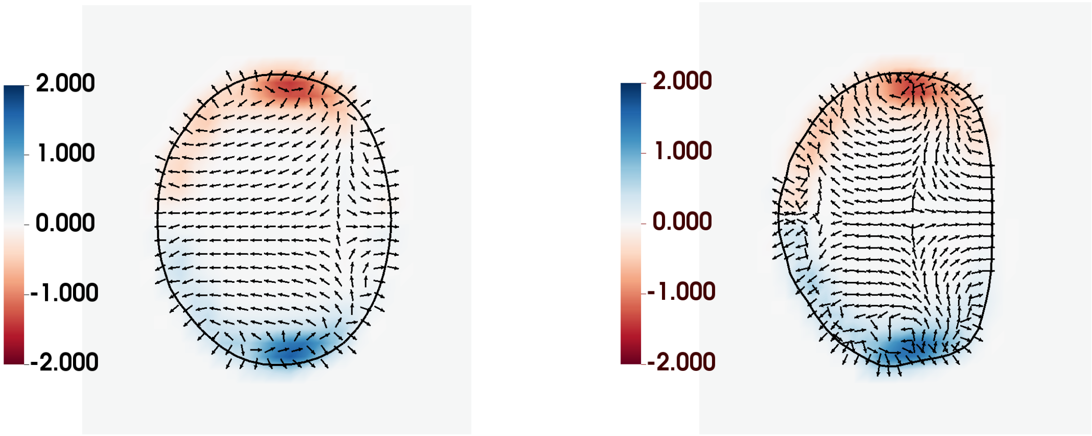

(a) $We_0 = 1$: Combustion (b) $We_0 = 12$: Combustion

Figure 6.13: Normalized vorticity with vectors of normalized liquid velocity at $t/\tau_p \sim 7$ at $Re_0 = 25$
Black line marks the liquid-gas interface.

6.4.2 Comparison of 3-D vs 2-D Results

A common strategy, particularly for simulations, is to develop and test models for multiphase flows such as boiling, evaporation in 2-D [25, 97, 103]. This is due to the significant reduction in computational cost associated to this change in dimensionality. However, this leads to the question of how useful such validations are. Can 2-D studies be used to gain useful trend information about 3-D flows, or are the physics of three dimensionality inherently important to the study of combustion? This can be done by interrogating if 2-D Cartesian analysis sufficient for simulating the droplet evaporation and combustion. Hence, as an additional insight to this research question, this section discusses the qualitative and quantitative differences between 2-D and 3-D results for combustion at $We_0 = 12$. The reason for selecting this Weber number is to analyze the differences for highly deformed shape, making it a more conservative test than the lower Weber number case.

To evaluate 2-D vs 3-D, the comparison of local evaporation flux ($\dot{m}''$), the area evolution (A/A_0), the flame stand-off distance and flame shape is presented in this section. Figure 6.14 shows the comparison between 2-D and 3-D for combustion at $We_0 = 12$ for the given conditions. The surface-averaged $\dot{m}''$ is observed to be higher in 3-D when compared to 2-D. At $t/\tau_p \sim 15$ is 42.5% lower in 2-D (thin yellow line with markers) when compared to 3-D (thick yellow line).

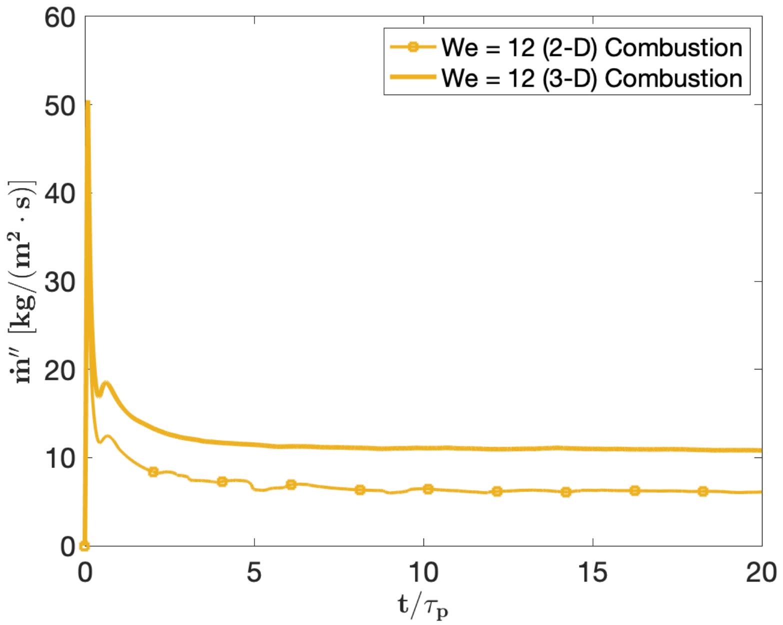

Figure 6.14: 2-D vs 3-D : Local evaporation flux $[kg/(m^2 \cdot s)]$ with t/τ_p at $We_0 = 12$, $Re = 25$

This higher mass flux in 3-D case is associated with the higher temperature gradients near to the liquid-gas interface. Such temperature gradients near the front stagnation point are shown in Fig. 6.15 where the thickness of this region of thermal gradient is lower in Fig. 6.15b than Fig. 6.15a, hence gradients are higher in 3-D.

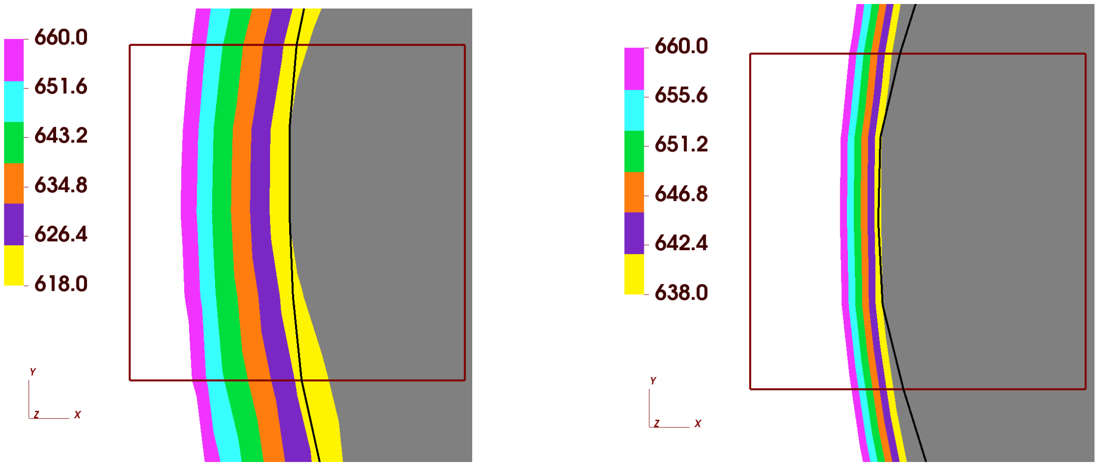

(a) $We_0 = 12$: 2-D Combustion (b) $We_0 = 12$: 3-D Combustion

Figure 6.15: 2-D vs 3-D : Gas Temperature $[K]$ near L-G interface for combustion at $t/\tau_p \sim 7$, $We_0 = 12$, $Re_0 = 25$
The maroon box is of size $l \times w = 20\ \mu m \times 20\ \mu m$

This region of higher temperature gradient in 3-D case is seen to coincide with the higher curvature near the windward stagnation point as shown in Fig. 6.16b when compared to Fig. 6.16a. The curvature is non-dimensionalized using the initial droplet diameter. The peak curvature in the stagnation region in 3-D is seen to be about twice that in 2-D, which agrees with trends for spherical/circular droplets in 3-D/2-D. This higher curvature results in a higher local evaporation flux (Fig. 6.14), consistent with the results from [95].

Figure 6.17 shows the comparison of A/A_0 for combustion at $We_0 = 12$, $Re_0 = 25$. A/A_0 in 3-D shows nearly linear increase in A/A_0 till $t/\tau_p \sim 12-15$ and tends to stabilize at a steady value at later time. However, 2-D results show the oscillations in A/A_0. These oscillations in A/A_0 continue till $t/\tau_p \sim 10-15$ and then reach nearly steady value. As observed from

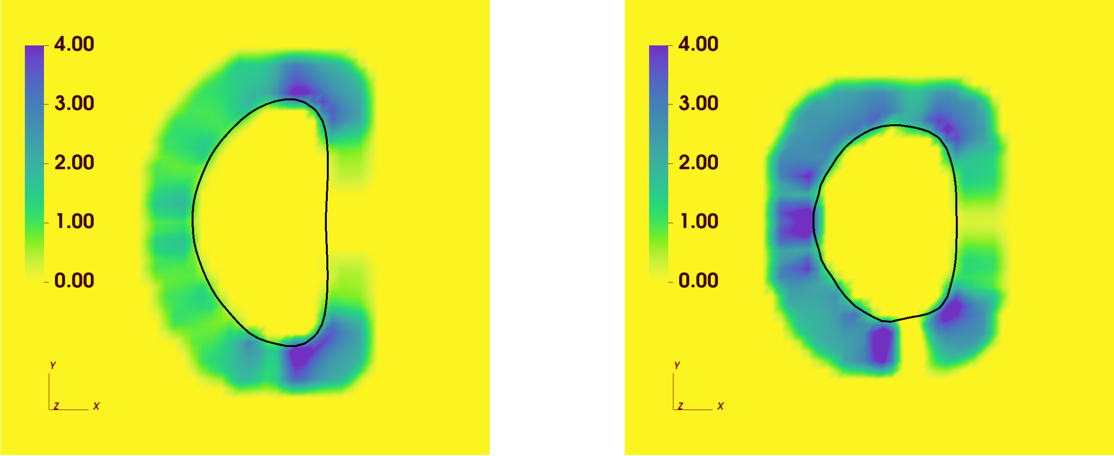

(a) 2-D : $We_0 = 12$ Combustion

(b) 3-D : $We_0 = 12$ Combustion

Figure 6.16: 2-D vs 3-D : Non-dimensional curvature at $t/\tau_p \sim 7$, $We_0 = 12$, $Re = 25$

these results, the trends of normalized surface area indicates that the selection of droplet geometry has a clear impact on the way it deforms. Furthermore, 2-D case has higher initial deformation when compared to 3-D case, however the long term trend is opposite. This comparison of shape is shown in Fig. 6.18.

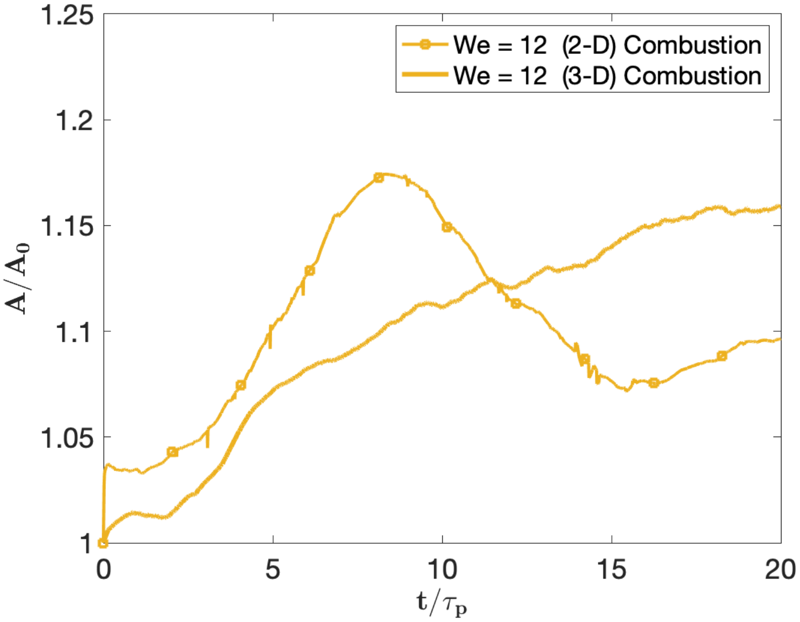

Figure 6.17: 2-D vs 3-D : Normalized total surface area with t/τ_p at $We_0 = 12$, $Re = 25$

To evaluate the difference between 2-D and 3-D on combustion at $We_0 = 12$, Fig. 6.18 shows the flame shape and flow field around the droplet. This demonstrates that although some aspects of the combustion are altered, the fundamental chemical behaviors between 2-D and 3-D droplets remains largely unchanged. However, an intriguing observation is the flame shape at the downstream of the droplet. In 2-D, a stronger vortical region forms in the wake of the droplet is leading to a cusp in the flame which is absent in 3-D cases. Such boundary layer development and the flow separation suggest a stronger influence of the wake dynamics on the combustion. Accordingly, there is a stronger interaction between the droplet shape and the combustion dynamics in 2-D when compared to 3-D.

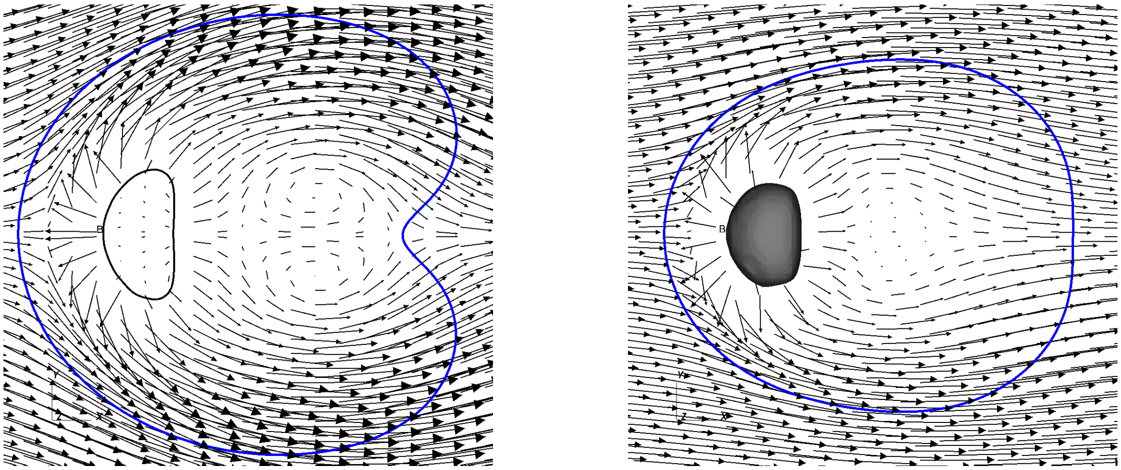

(a) $We_0 = 12$: 2-D Combustion

(b) $We_0 = 12$: 3-D Combustion

Figure 6.18: 2-D vs 3-D : Velocity vector field for combustion at $t/\tau_p \sim 7$, $Re_0 = 25$
blue line marks the flame

It is also interesting to note that, although a cusp was not observed in the 3-D flame Fig. 6.18b (i.e. the stochiometric contour), it is observed on the inner contour of CO_2 and absent on the outer contour of CO_2 Fig. 6.8b, suggesting the nature of the flame development may be different between 2-D and 3-D. Moreover, the flame appears to be wider in 2-D combustion case. The normalized flame stand-off distance S^* is calculated using the following expressions,

$$(S^*)_{2-D} = \frac{A_{flame}}{A_{0\ droplet}} \tag{6.10}$$

$$(S^*)_{3-D} = \sqrt{\frac{A_{flame}}{A_{0\ droplet}}} \tag{6.11}$$

Here $A_{0\ droplet}$ is initial area of droplet. It is important to note that the ‘area’ of the 2-D flame is its the surface area per unit depth i.e. its perimeter. The given expressions are written such that for a spherical (circular) flame in 3-D (2-D) the resulting expression simplifies to r_{flame}/r_0. Using these expressions, the flame stand-off distance history is plotted with non-dimensional time as shown in Fig. 6.19. Higher flame stand-off distance is observed for 2-D cases in comparison to 3-D with combustion. This supports the observation of 34% wider flame in 2-D in Fig. 6.18. Moreover, the magnitude of S^* is seen to be increasing with time which suggests the flame growth in time.

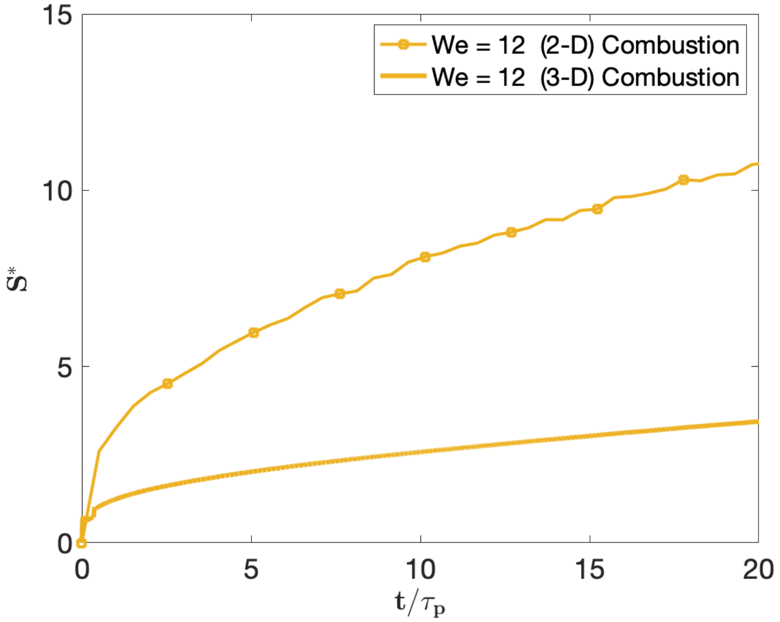

Figure 6.19: 2-D vs 3-D: Normalized flame stand-off distance (S^*) vs t/τ_p at $Re_0 = 25$

It is important to note that the results here are demonstrated for a envelope flame configuration. Given the greater importance of wake dynamics in 2-D compared to 3-D, it is likely that wake flame dynamics and flame stability will be significantly different between 2-D and 3-D. However, such aspects are beyond the focus of this study.

6.5 Conclusions

With the focus on large spray droplets, this work presents a DNS study on the combustion of a freely deformable droplet in a high pressure ($P_\infty = 20\ atm$), high temperature ($T_\infty = 1400\ K$) convective flow at $Re_0 = 25$. This work improves upon the existing understanding of droplet evaporation and combustion as most of the past studies consider the droplet shape to be either spherical or an imposed shape such as ellipsoid throughout its lifetime. However, in reality, these large droplets have tendency to deform due to imbalance of surface tension and aerodynamic forces. This deformation is governed by Weber number. $We_0 = 1$ (nearly spherical shape) and $We_0 = 12$ (the limit for droplet breakup) are selected for this work. A single step combustion mechanism is used for combustion.

The effect of droplet shape on pure evaporation and combustion is studied by varying the surface tension inside the liquid droplet at $Re_0 = 25$ for the same ambient gas conditions. The results showed higher total evaporation rate for higher Weber number case. This enhancement reaches upto 9% for $We_0 = 12$ combustion case. This is due to net effect of decrease in local flux and increase in total surface area for higher Weber number case. Moreover, at this Re_0 and ambient gas conditions, initial Damköhler number is $Da_0 > 1.02$ which favors a non-spherical envelope flame. From the detailed analysis of gas temperatures, flame shape, and flame stand-off distance, it is found that even with the droplet shape change and enhancement in total evaporation rate, the combustion demonstrates little sensitivity to droplet shape at this Re_0. Small differences are noticed in the flame shape, and in particular the flame appears to be longer in the higher Weber number case. However, due to domination of chemical reaction rate over evaporation at given ambient conditions, the overall effect is small. It is also important to note that droplets do not reach critical deformation conditions and break-up even at further higher Weber numbers such as $We_0 = 16,\ 20$. Whereas, the non-combusting, non-evaporating droplets at $We_0 = 16,\ 20$ demonstrate larger deformation and experience the vibrational break-up mode. This leads to an understanding that the droplet deformation is suppressed by the higher evaporation rates during combustion. Therefore, there is a more complex interaction between droplet shape and combustion which needs further investigation.

3-D numerical studies including the combustion are known to be computationally expensive. The question "what can be learned from less expensive 2-D simulations ? " was explored. After a careful scrutiny between 2-D and 3-D results at $We_0 = 12$, it is found that surface averaged local flux is 42.5% lower in 2-D when compared to 3-D. This is due to larger temperature gradient near the droplet, which drives higher evaporation. Moreover, the trend of total surface area of droplet in 2-D is not same as 3-D. Though both cases show envelope flame, the presence of larger recirculation region due to larger deformation is causing a cusp in the flame shape at the downstream in 2-D cases. This wake region is significantly smaller and the vortices in the wake are less powerful in 3-D. This leads to absence of cusp in flame.

Moreover, the flame stand-off distance is higher in 2-D when compared to 3-D. Hence, it is learned that 2-D studies do not represent the accurate flow physics. Although, similar trends are demonstrated for this envelope flame topology. However, it is likely that due to the stronger influence of wake dynamics in 2-D, this strategy will not work well for other flame regimes.

Chapter 7

Summary and Future Work

7.1 Summary

This dissertation covered detailed studies on droplet evaporation and combustion under various environments. Truly, the purpose of these studies is to analyze the small-scale processes involved in spray combustion. Similar to experimental strategy to study such problem, a single isolated droplet is investigated here using numerical tools. An existing numerical framework is utilized which is built upon an in-house multiphase solver NGA. This framework is based on Interface-capturing approach using VOF for fully-resolved phase-changing flows at low Mach numbers. Chapter 2 covers the detailed description of this numerical framework along with short summary of general strategies to solve various multiphase flows numerically.

As the focus of this work is to observe the inside-out of the evaporating/burning droplet, the motion of the droplet needs to be restricted. Instead of using a fiber to suspend the droplet (which is usually one way of doing it in the experiments), a non-intrusive numerical technique "gravity update method" is developed and demonstrated in Chapter 3. This addition in the numerical framework led to minimal droplet shift inside the domain even under highly convective flow conditions and further utilized in all of the presented studies here.

Chapter 4 dealt with the evaporation of a deformable droplet under convective flow. In these studies the droplet deforms freely based on the aerodynamic forces it experiences. Before exploring the effect of droplet shape, the solver accuracy is validated against empirical correlation for droplet evaporation by Abramzon and Sirignano [3] and the results are found in good agreement. To analyze the effect of droplet shape on its evaporation rate, a quasi-steady evaporation approach is implemented. A detailed discussion of this approach is covered in Section 4.2.2. For a constant relative inflow velocity, the droplet shape is varied by modifying Weber number from $We = 1 - 12$. The convective flow velocity is modified by changing initial Reynolds number $Re = 25, 120$. For highly deformed droplet at $We = 12$ and $Re = 120$, 20% enhancement in total evaporation rate is observed when compared to nearly spherical droplet. Strong effects of wake dynamics are uncovered for such highly deformed droplet, suggesting a more complex relationship among We, Re and the evaporation phenomena.

Chapter 5 covered the evaporation of deformable droplet under natural convection. Such natural convection around the hot droplet is a results of varying buoyant forces on liquid and gas phase due to variable density with temperature. The existing framework is modified to account for the variable density of both liquid and gas phases using Bousinessq approximation. A thorough validation of these changes in numerical framework is done against the measured experimental results as well an existing experiment results by Murakami et al. [61]. The solver shows reasonable agreement with the experiment results.

Finally, Chapter 6 demonstrated the combustion of a deformable droplet under convective flow at $Re = 25$. For the selected ambient gas conditions, initial Damköhler number is $Da_0 > 1.02$ which favors an envelope flame. The higher Weber number case consistently show higher evaporation rate when compared to $We = 1$. This enhancement reaches upto 9% for $We = 12$ combustion case. From the detailed analysis of gas temperatures, flame shape, and flame stand-off distance, it is found that even with the droplet shape change and enhancement in total evaporation rate, the combustion demonstrates little sensitivity to droplet shape at this Re_0. Moreover, the droplets do not reach critical deformation conditions and break-up even at further higher Weber numbers such as $We_0 = 16,\ 20$. Whereas, the non-combusting, non-evaporating droplets at $We_0 = 16,\ 20$ demonstrate larger deformation and experience the vibrational break-up mode. This suggests that the droplet deformation is suppressed by the higher evaporation rates during combustion. Therefore, there is a complicated interaction between droplet shape and its burning which calls for further investigation.

7.2 Future Work

While this work has brought significant contributions to our understanding on the droplet evaporation, it is important to acknowledge that there is still ample room for further exploration. The following areas represent promising avenues for future work and deserve careful consideration:

Development of correlation for evaporation under forced convection: It is evident from the results presented in Chapter 4 that the deformation of droplet has significant impact on the evaporation rate under forced convection. These results demonstrate an opportunity to introduce a correction factor based on Weber number in computation of total evaporation rate with point mass assumption. A rigorous focus on correlation development can be a step forward in this direction.

Exploration of droplet shape effect under natural convection: After the validation of numerical solver for variable density in Chapter 5, the solver can be used to investigate the interaction of natural convection and droplet shape on evaporation. This can be done by varying the relevant non-dimensional numbers, i.e. Grashof number and Eötvös number respectively. The findings derived from these results offer valuable insights into the intricate dynamics between natural convection strength, droplet shape, and their combined impact on the development of the boundary layer. Furthermore, this approach can be utilized for the exploration on the droplet evaporation under partial gravity environment.

Advanced Combustion Mechanism: Currently, we utilized one-step combustion mechanism from Westbrook and Dryer [114]. There are more sophisticated combustion mechanisms such as global mechanism which can predict the chemical aspect of combustion process better.

Droplet-Droplet interaction: Under the presence of forced convection, the evaporation of deformed droplet is significantly impacted by the wake interaction. Such interaction is seen to alter the distribution of local evaporation flux especially in the wake region. This learning can inspire further investigation on how these deformed droplets interact with each other.

By addressing these areas of future work, we can further advance our understanding of the complex interplay between droplet shape, evaporation, and combustion, leading to improved numerical modeling for the design and optimization strategies for a wide range of practical applications.

Bibliography

[1] *NIST Chemistry WebBook*. doi:10.18434/T4D303.

[2] Modern Applications of Liquid Fuels. *Nature*, 161(4104):1007, 1948. ISSN 1476-4687. doi:10.1038/1611007c0.

[3] B. Abramzon and W.A. Sirignano. Droplet vaporization model for spray combustion calculations. *International Journal of Heat and Mass Transfer*, 32(9):1605 – 1618, 1989. ISSN 0017-9310. doi:10.1016/0017-9310(89)90043-4.

[4] Johanna Aurell, David Hubble, Brian K Gullett, Amara Holder, Ephraim Washburn, and Dennis Tabor. Characterization of Emissions from Liquid Fuel and Propane Open Burns. *Fire Technology*, 53(6):2023–2038, 2017. ISSN 1572-8099. doi:10.1007/s10694-017-0670-2.

[5] P. Bagchi and S. Balachandar. Steady planar straining flow past a rigid sphere at moderate reynolds number. *Journal of Fluid Mechanics*, 466:365–407, 2002. doi:10.1017/S0022112002001490.

[6] P. Bagchi and S. Balachandar. Inertial and viscous forces on a rigid sphere in straining flows at moderate reynolds numbers. *Journal of Fluid Mechanics*, 481:105–148, 2003. doi:10.1017/S002211200300380X.

[7] B. Banu. Fluids and combustion facility (FCF) and combustion integrated rack (CIR), NASA John H. Glenn Research Center, Payload Accomodations Handbook CIR-DOC-4064, 2008.

[8] Theodore L Bergman, Adrienne S Lavine, Frank P Incropera, and David P DeWitt. *Fundamentals of Heat and Mass Transfer*. Wiley, New York, 8th ed edition, 2017. ISBN 9781119337676.

[9] Madjid Birouk and Patrick Toews. Effect of the initial diameter on the vaporization rate of a fuel droplet in a turbulent atmosphere: Experimental data. In *25th Int. Colloq. Dyn. Explos. React. Syst., Leeds, UK*, 2015.

[10] Christopher E. Brennen. *Fundamentals of Multiphase Flow*. Cambridge University Press, 2005. doi:10.1017/CBO9780511807169.

[11] J W C. Liquid Fuel. *Nature*, 99(2476):134, 1917. ISSN 1476-4687. doi:10.1038/099134a0.

[12] C. Chauveau, X. Chesneau, and I. Gökalp. High pressure vaporization and burning of methanol droplets in reduced gravity. *Advances in Space Research*, 16(7):157–160, jan 1995. ISSN 02731177. doi:10.1016/0273-1177(95)00152-5.

[13] Christian Chauveau, Fabien Halter, Arnaud Lalonde, and Iskender Gökalp. An experimental study on the droplet vaporization: Effects of heat conduction through the support fiber. *22 nd Annual Conference on Liquid Atomization and Spray Systems (ILASS Europe)*, 2008.

[14] Christian Chauveau, Madjid Birouk, Fabien Halter, and Iskender Gökalp. An analysis of the droplet support fiber effect on the evaporation process. *International Journal of Heat and Mass Transfer*, 128:885–891, 2019. ISSN 00179310. doi:10.1016/j.ijheatmasstransfer.2018.09.029.

[15] H. H. Chiu, H. Y. Kim, and E. J. Croke. Internal group combustion of liquid droplets.

Symposium (International) on Combustion, 19(1):971–980, 1982. ISSN 00820784. doi:10.1016/S0082-0784(82)80273-7.

[16] Chong Pyo Cho, Ho Young Kim, and Sam S. Yoon. Interaction of the burning spherical droplets in oxygen-enriched turbulent environment. *Combustion and Flame*, 156(1): 14–24, 2009. ISSN 0010-2180. doi:10.1016/j.combustflame.2008.10.026.

[17] R Clift, J R Grace, and M E Weber. *Bubbles, Drops, and Particles.* Academic Press, Inc., New York, 1978.

[18] Olivier Desjardins, Guillaume Blanquart, Guillaume Balarac, and Heinz Pitsch. High order conservative finite difference scheme for variable density low mach number turbulent flows. *J. Comput. Phys.*, 227(15):7125–7159, jul 2008. ISSN 0021-9991. doi:10.1016/j.jcp.2008.03.027.

[19] Olivier Desjardins, Jeremy McCaslin, Mark Owkes, and Peter Brady. Direct numerical and large-eddy simulation of primary atomization in complex geometries. *Atomization and Sprays*, 23(11):1001–1048, 2013. ISSN 1044-5110. doi:10.1615/AtomizSpr.2013007679.

[20] Daniel L Dietrich, Vedha Nayagam, Michael C Hicks, Paul V Ferkul, Frederick L Dryer, Tanvir Farouk, Benjamin D Shaw, Hyun Kyu Suh, Mun Y Choi, Yu Cheng Liu, C Thomas Avedisian, and Forman A Williams. Droplet Combustion Experiments Aboard the International Space Station. *Microgravity Science and Technology*, 26(2): 65–76, oct 2014. ISSN 0938-0108. doi:10.1007/s12217-014-9372-2.

[21] G. M. Faeth. Mixing, transport and combustion in sprays. *Progress in Energy and Combustion Science*, 13(4):293–345, 1987. ISSN 03601285. doi:10.1016/0360-1285(87)90002-5.

[22] G.M. Faeth. Dynamics of secondary drop breakup—a rate controlling process in dense sprays. In *Institute for Liquid Atomization and Spray Systems*, 2002.

[23] A.C. Fernandez-Pello and C.K. Law. A theory for the free-convective burning of a condensed fuel particle. *Combustion and Flame*, 44(1):97–112, 1982. ISSN 0010-2180. doi:10.1016/0010-2180(82)90066-9.

[24] I. Frankel and D. Weihs. Shape and stability of a liquid drop moving at low Weber number. *Applied Scientific Research*, 40(3):279–294, January 1983.

[25] Frédéric Gibou, Liguo Chen, Duc Nguyen, and Sanjoy Banerjee. A level set based sharp interface method for the multiphase incompressible navier–stokes equations with phase change. *Journal of Computational Physics*, 222(2):536–555, 2007. doi:10.1016/j.jcp.2006.07.035.

[26] George Gogos, Siang Soh, and Daniel N. Pope. Effects of gravity and ambient pressure on liquid fuel droplet evaporation. *International Journal of Heat and Mass Transfer*, 46(2):283–296, 2003. ISSN 0017-9310. doi:10.1016/S0017-9310(02)00269-7.

[27] I. Gokalp, C. Chauveau, J. R. Richard, M. Kramer, and W. Leuckel. Observations on the low temperature vaporization and envelope or wake flame burning of n-heptane droplets at reduced gravity during parabolic flights. *Symposium (International) on Combustion*, 22(1):2027–2035, 1989. doi:10.1016/S0082-0784(89)80218-8.

[28] Subramanyam R. Gollahalli and T.A. Brzustowski. Flame length in the wake of a burning hydrocarbon drop. *Combustion and Flame*, 22(3):313–322, 1974. doi:10.1016/0010-2180(74)90046-7.

[29] Subramanyam R. Gollahalli and T.A. Brzustowski. The effect of pressure on the flame

structure in the wake of a burning hydrocarbon droplet. *Symposium (International) on Combustion*, 15(1):409–417, 1975. doi:10.1016/S0082-0784(75)80315-8.

[30] Jixiang Guo, Yuqi Yang, Shuai Zhang, Dengshan Zhang, Chang Cao, Bo Ren, Lei Liu, Yu Xing, and Ruiying Xiong. Heavy oil-water flow patterns in a small diameter vertical pipe under high temperature/pressure conditions. *Journal of Petroleum Science and Engineering*, 171(March):1350–1365, 2018. ISSN 09204105. doi:10.1016/j.petrol.2018.08.021.

[31] Chawki Habchi and Vahid Ebrahimian. Gravitational Effects on Multi-component Droplet Evaporation. *Microgravity Science and Technology*, 24(3):229–235, 2012. ISSN 1875-0494. doi:10.1007/s12217-012-9303-z.

[32] R. J. Haywood, R. Nafziger, and M. Renksizbulut. A Detailed Examination of Gas and Liquid Phase Transient Processes in Convective Droplet Evaporation. *Journal of Heat Transfer*, 111(2):495–502, 05 1989. ISSN 0022-1481. doi:10.1115/1.3250704.

[33] R. J. Haywood, M. Renksizbulut, and G. D. Raithby. Numerical solution of deforming evaporating droplets at intermediate reynolds numbers. *Numerical Heat Transfer, Part A: Applications*, 26(3):253–272, 1994. doi:10.1080/10407789408955991.

[34] J. J. Hegseth, N. Rashidnia, and A. Chai. Natural convection in droplet evaporation. *Physical Review E - Statistical Physics, Plasmas, Fluids, and Related Interdisciplinary Topics*, 54(2):1640–1644, 1996. ISSN 1063651X. doi:10.1103/PhysRevE.54.1640.

[35] M. Herrmann, G. Blanquart, and V. Raman. Flux corrected finite volume scheme for preserving scalar boundedness in reacting large-eddy simulations. *AIAA Journal*, 44 (12):2879–2886, 2006. doi:10.2514/1.18235.

[36] J. O. Hinze. Fundamentals of the hydrodynamic mechanism of splitting in dispersion processes. *AIChE Journal*, 1:289–295, 1955. doi:10.1002/aic.690010303.

[37] C. Shinn J Robbins. Multi-user droplet combustion apparatus flex2, NASA John H. Glenn Research Center, Reflight Safety Data Package MDC-DOC-1790A, 2010.

[38] Patrick Jenny, Dirk Roekaerts, and Nijso Beishuizen. Modeling of turbulent dilute spray combustion. *Progress in Energy and Combustion Science*, 38(6):846–887, 2012. ISSN 03601285. doi:10.1016/j.pecs.2012.07.001.

[39] M H (Mohammad Hossein) Keshavarz. *Liquid fuels as jet fuels and propellants : a review of their productions and applications / Mohammad Hossein Keshavarz.* Energy Science, Engineering and Technology. Nova Science Publishers, New York, 2018. ISBN 1-5361-4312-X.

[40] Andrei Nikolaevich Kolmogorov, V. Levin, Julian Charles Roland Hunt, Owen Martin Phillips, and David Williams. The local structure of turbulence in incompressible viscous fluid for very large reynolds numbers. *Proceedings of the Royal Society of London. Series A: Mathematical and Physical Sciences*, 434(1890):9–13, 1991. doi:10.1098/rspa.1991.0075.

[41] S. Kotake and T. Okazaki. Evaporation and combustion of a fuel droplet. *International Journal of Heat and Mass Transfer*, 12(5):595–609, 1969. ISSN 0017-9310. doi:10.1016/0017-9310(69)90041-6.

[42] Aniket P. Kulkarni and D. Deshmukh. Planar drop-sizing in dense fuel sprays using advanced laser diagnostic techniques. In Richard Viskup, editor, *Diesel and Gasoline Engines*, chapter 5. IntechOpen, Rijeka, 2020. doi:10.5772/intechopen.90527.

[43] Markku Kulmala, Timo Vesala, Jaroslav Schwarz, and Jiri Smolik. Mass transfer

from a drop—ii. theoretical analysis of temperature dependent mass flux correlation. *International Journal of Heat and Mass Transfer*, 38(9):1705–1708, 1995. ISSN 0017-9310. doi:10.1016/0017-9310(94)00302-C.

[44] Seiichiro Kumagai and Hiroshi Isoda. Combustion of fuel droplets in a falling chamber. *Symposium (International) on Combustion*, 6(1):726–731, 1957. ISSN 0082-0784. doi:10.1016/S0082-0784(57)80100-3.

[45] T. Kékesi, G. Amberg, and L. Prahl Wittberg. Drop deformation and breakup. *International Journal of Multiphase Flow*, 66:1–10, 2014. ISSN 0301-9322. doi:10.1016/j.ijmultiphaseflow.2014.06.006.

[46] C.K. Law. Recent advances in droplet vaporization and combustion. *Progress in Energy and Combustion Science*, 8(3):171–201, 1982. ISSN 0360-1285. doi:10.1016/0360-1285(82)90011-9.

[47] C.K. Law, S. Prakash, and W.A. Sirignano. Theory of convective, transient, multicomponent droplet vaporization. *Symposium (International) on Combustion*, 16(1): 605–617, 1977. ISSN 0082-0784. doi:10.1016/S0082-0784(77)80356-1.

[48] A.H. Lefebvre and V.G. McDonell. *Atomization and Sprays*. CRC Press. ISBN 9781315120911. doi:10.1201/9781315120911.

[49] Yushu Lin and John Palmore Jr. Effect of droplet deformation and internal circulation on drag coefficient. *Phys. Rev. Fluids*, 7:123602, Dec 2022. doi:10.1103/PhysRevFluids.7.123602.

[50] Yushu Lin, Meha Setiya, and John Palmore Jr. A numerical strategy for investigating internal circulation in droplets. *AIAA SCITECH Forum*, 2022. doi:10.2514/6.2022-1443.

[51] Mark Linne. Imaging in the optically dense regions of a spray: A review of developing techniques. *Progress in Energy and Combustion Science*, 39:403–440, 10 2013. doi:10.1016/j.pecs.2013.06.001.

[52] Xu-Dong Liu, Ronald P. Fedkiw, and Myungjoo Kang. A boundary condition capturing method for poisson's equation on irregular domains. *Journal of Computational Physics*, 160(1):151–178, 2000. ISSN 0021-9991. doi:10.1006/jcph.2000.6444.

[53] Yu Cheng Liu, Yuhao Xu, Michael C. Hicks, and C. Thomas Avedisian. Comprehensive study of initial diameter effects and other observations on convection-free droplet combustion in the standard atmosphere for n-heptane, n-octane, and n-decane. *Combustion and Flame*, 171:27–41, 2016. ISSN 0010-2180. doi:10.1016/j.combustflame.2016.05.013.

[54] Eric Loth. Quasi-steady shape and drag of deformable bubbles and drops. *International Journal of Multiphase Flow*, 34:523–546, 06 2008. doi:10.1016/j.ijmultiphaseflow.2007.08.010.

[55] C. Ma and D. Bothe. Numerical modeling of thermocapillary two-phase flows with evaporation using a two-scalar approach for heat transfer. *Journal of Computational Physics*, 233:552–573, 2013. ISSN 0021-9991. doi:10.1016/j.jcp.2012.09.011.

[56] Shev MacNamara and Gilbert Strang. *Operator Splitting*, pages 95–114. Springer International Publishing, Cham, 2016. ISBN 978-3-319-41589-5. doi:10.1007/978-3-319-41589-5_3.

[57] Farzad Mashayek. Dynamics of evaporating drops. part i: Formulation and evaporation model. *International Journal of Heat and Mass Transfer*, 44:1517–1526, 04 2001. doi:10.1016/S0017-9310(00)00199-X.

[58] A. R. Masri. Turbulent Combustion of Sprays: From Dilute to Dense. *Combustion Science and Technology*, 188(10):1619–1639, 2016. ISSN 1563521X. doi:10.1080/00102202.2016.1198788.

[59] R.L Matlosz, S Leipziger, and T.P Torda. Investigation of liquid drop evaporation in a high temperature and high pressure environment. *International Journal of Heat and Mass Transfer*, 15(4):831–852, 1972. ISSN 0017-9310. doi:10.1016/0017-9310(72)90124-X.

[60] Alejandro Millán-Merino, Eduardo Fernández-Tarrazo, and Mario Sánchez-Sanz. Theoretical and numerical analysis of the evaporation of mono- and multicomponent single fuel droplets. *Journal of Fluid Mechanics*, 910:A11, 2021. doi:10.1017/jfm.2020.950.

[61] Yosuke Murakami, Hiroshi Nomura, and Yusuke Suganuma. Experimental Study on Unsteadiness of n-decane Single Droplet Evaporation and Effect of Natural Convection on Droplet Evaporation at High Pressures and Temperatures. *Transactions of the Japan society for Aeronautical and space science, Aerospace Technology Japan*, 19(5):19.647, 2021. ISSN 1884-0485. doi:10.2322/tastj.19.647.

[62] S. Okajima and S. Kumagai. Experimental studies on combustion of fuel droplets in flowing air under zero- and high-gravity conditions. *Symposium (International) on Combustion*, 19(1):1021–1027, 1982. doi:10.1016/S0082-0784(82)80278-6.

[63] Mark Owkes and Olivier Desjardins. A computational framework for conservative , three-dimensional , unsplit , geometric transport with application to the volume-of-fluid (VOF) method. *Journal of Computational Physics*, 270:587–612, 2014. ISSN 0021-9991. doi:10.1016/j.jcp.2014.04.022.

[64] Gonçalo Pacheco, André Silva, and Mário Costa. Single-droplet combustion of jet a-1,

hydroprocessed vegetable oil, and their blends in a drop-tube furnace. *Energy & Fuels*, 35(9):7232–7241, 2021. doi:10.1021/acs.energyfuels.0c03476.

[65] J. A. Palmore Jr. *Numerical Framework for Simulating Multiphase Flows with Phase Change*. PhD Thesis, Cornell University, 2018.

[66] John Palmore Jr. Dns of n-heptane droplet vaporization and combustion. Mar 2019. URL `https://vtechworks.lib.vt.edu/handle/10919/108311`.

[67] John Palmore Jr. On the Vaporization Rate and Flame Shape of Nonspherical Droplets. *Journal of Heat Transfer*, 144(6), 03 2022. ISSN 0022-1481. doi:10.1115/1.4053729.

[68] John Palmore Jr and O. Desjardins. Validating a numerical framework for resolved simulations of vaporizing droplets. In *International Conference on Liquid Atomization and Spray Systems*, 2018.

[69] John Palmore Jr and O. Desjardins. A volume of fluid framework for interface-resolved simulations of vaporizing liquid-gas flows. *Journal of Computational Physics*, 399: 108954, Dec 2019. ISSN 0021-9991. doi:10.1016/j.jcp.2019.108954.

[70] John Palmore Jr and Yushu Lin. Interface-capturing numerical studies of multicomponent spray and droplet vaporization. In *AIAA SCITECH 2022 Forum*. doi:10.2514/6.2022-1444.

[71] Tony Phillips. Strange flames on the iss, 2013. URL `https://science.nasa.gov/science-news/science-at-nasa/2013/18jun_strangeflames`.

[72] M. Pilch and C.A. Erdman. Use of breakup time data and velocity history data to predict the maximum size of stable fragments for acceleration-induced breakup of a liquid drop. *International Journal of Multiphase Flow*, 13(6):741–757, 1987. ISSN 0301-9322. doi:10.1016/0301-9322(87)90063-2.

[73] James Edward Pilliod and Elbridge Gerry Puckett. Second-order accurate volume-of-fluid algorithms for tracking material interfaces. *Journal of Computational Physics*, 199(2):465–502, 2004. ISSN 00219991. doi:10.1016/j.jcp.2003.12.023.

[74] Daniel N. Pope and George Gogos. Numerical simulation of fuel droplet extinction due to forced convection. *Combustion and Flame*, 142(1-2):89–106, 2005. doi:10.1016/j.combustflame.2005.02.010.

[75] Stéphane Popinet. Numerical models of surface tension. *Annual Review of Fluid Mechanics*, 50(1):49–75, 2018. doi:10.1146/annurev-fluid-122316-045034.

[76] V. Raghavan, V. Babu, T. Sundararajan, and R. Natarajan. Flame shapes and burning rates of spherical fuel particles in a mixed convective environment. *International Journal of Heat and Mass Transfer*, 48(25):5354–5370, 2005. ISSN 0017-9310. doi:10.1016/j.ijheatmasstransfer.2005.07.029.

[77] R. H. Rangel and A. C. Fernandez-Pello. Mixed convective droplet combustion withl internal circulation. *Combustion Science and Technology*, 42(1-2):47–65, 1984. ISSN 1563521X. doi:10.1080/00102208408960368.

[78] WE Ranz and WR Marshall. Evaporation from drops. *Chemical Engineering Prog.*, 32(9):1605 – 1618, 1989. ISSN 0017-9310. doi:10.1016/0017-9310(89)90043-4.

[79] Bastian Rauch, Raffaela Calabria, Fabio Chiariello, Patrick Le Clercq, Patrizio Massoli, and Michael Rachner. Accurate analysis of multicomponent fuel spray evaporation in turbulent flow. *Experiments in Fluids*, 52(4):935–948, 2012. ISSN 1432-1114. doi:10.1007/s00348-011-1169-0.

[80] Saroj Ray, Vasudevan Raghavan, and George Gogos. Two-phase transient simulations of evaporation characteristics of two-component liquid fuel droplets at high pres-

sures. *International Journal of Multiphase Flow*, 111:294–309, 2019. ISSN 0301-9322. doi:10.1016/j.ijmultiphaseflow.2018.10.002.

[81] Rolf D. Reitz. *Atomization and other breakup regimes of a liquid jet*. PhD thesis, 1978.

[82] M. Renksizbulut and M. C. Yuen. Numerical Study of Droplet Evaporation in a High-Temperature Stream. *Journal of Heat Transfer*, 105(2):389–397, 05 1983. ISSN 0022-1481. doi:10.1115/1.3245591.

[83] M. Renksizbulut and M. C. Yuen. Experimental Study of Droplet Evaporation in a High-Temperature Air Stream. *Journal of Heat Transfer*, 105(2):384–388, 05 1983. ISSN 0022-1481. doi:10.1115/1.3245590.

[84] Metin Renksizbulut, Rick Nafziger, and Xianguo Li. A mass transfer correlation for droplet evaporation in high-temperature flows. *Chemical Engineering Science*, 46: 2351–2358, 1991.

[85] Adrian Roth, David Frantz, William Chaze, Andrew Corber, and Edouard Berrocal. High-speed imaging database of water jet disintegration Part I: Quantitative imaging using liquid laser-induced fluorescence. *International Journal of Multiphase Flow*, 145: 103641, 2021. ISSN 03019322. doi:10.1016/j.ijmultiphaseflow.2021.103641.

[86] Lucia Rueda Villegas, Romain Alis, Mathieu Lepilliez, and Sébastien Tanguy. A Ghost Fluid/Level Set Method for boiling flows and liquid evaporation: Application to the Leidenfrost effect. *Journal of Computational Physics*, 316:789–813, 2016. ISSN 10902716. doi:10.1016/j.jcp.2016.04.031.

[87] S. Mirjalili, S. S. Jain, and M. S. Dodd. A review of interface-capturing methods for two-phase flow. *Annual Research Briefs 2017, Center for Turbulence Research*, (1): 117–135, 2017.

[88] Jun'ichi Sato, Mitsuhiro Tsue, Mario Niwa, and Michikata Kono. Effects of natural convection on high-pressure droplet combustion. *Combustion and Flame*, 82(2):142–150, 1990. ISSN 00102180. doi:10.1016/0010-2180(90)90093-7.

[89] Nicolò Scapin, Pedro Costa, and Luca Brandt. A volume-of-fluid method for interface-resolved simulations of phase-changing two-fluid flows. *Journal of Computational Physics*, 407:109251, 2020. ISSN 10902716. doi:10.1016/j.jcp.2020.109251.

[90] Jan Schlottke and Bernhard Weigand. Direct numerical simulation of evaporating droplets. *Journal of Computational Physics*, 227(10):5215–5237, 2008. ISSN 0021-9991. doi:10.1016/j.jcp.2008.01.042.

[91] Meha Setiya and John Palmore Jr. Combustion and evaporation of deformable fuel droplets. *ASME Journal of Heat and Mass Transfer*, 2023. doi:10.1115/1.4062784.

[92] Meha Setiya and John Palmore Jr. Method to study effect of straining flow on droplet vaporization at low Reynolds number. *Spring Technical Meeting Eastern States Section of the Combustion Institute*, March 2020. URL `https://vtechworks.lib.vt.edu/handle/10919/108308`.

[93] Meha Setiya and John Palmore Jr. Effect of straining flow and droplet shape on vaporization rate of liquid fuel droplet. *APS Division of Fluid Dynamics Meeting Abstracts*, art. Z14.002, January 2020. URL `https://vtechworks.lib.vt.edu/handle/10919/109736`.

[94] Meha Setiya and John Palmore Jr. Combustion and vaporization of deformable fuel droplets using direct numerical simulation. *International Mechanical Engineering Congress and Exposition*, 2022. doi:10.1115/IMECE2022-94475.

[95] Meha Setiya and John Palmore Jr. Quasi-steady evaporation of deformable liquid fuel droplets. *International Journal of Multiphase Flow*, page 104455, 2023. doi:10.1016/j.ijmultiphaseflow.2023.104455.

[96] Meha Setiya and John Palmore Jr. Evaporation of deformable droplets under natural convection: comparison of DNS results with experiments. In *AIAA Science and Technology Forum and Exposition (AIAA SciTech Forum)*, 2024.

[97] Changxiao Shao, Kun Luo, Min Chai, Haiou Wang, and Jianren Fan. A computational framework for interface-resolved DNS of simultaneous atomization, evaporation and combustion. *Journal of Computational Physics*, 371:751–778, 2018. doi:10.1016/j.jcp.2018.06.011.

[98] William A. Sirignano. *Fluid Dynamics and Transport of Droplets and Sprays*. Cambridge University Press, 1999. doi:10.1017/CBO9780511529566.

[99] M. Sommerfeld. *Numerical Methods for Dispersed Multiphase Flows*, pages 327–396. Springer International Publishing, Cham, 2017. ISBN 978-3-319-60282-0. doi:10.1007/978-3-319-60282-0_6.

[100] Mark Sussman and Mitsuhiro Ohta. A stable and efficient method for treating surface tension in incompressible two-phase flow. *SIAM Journal on Scientific Computing*, 31 (4):2447–2471, 2009. doi:10.1137/080732122.

[101] Sadatoshi Taneda. Experimental investigation of the wake behind a sphere at low reynolds numbers. *Journal of the Physical Society of Japan*, 11(10):1104–1108, 1956. doi:10.1143/JPSJ.11.1104.

[102] Sadatoshi Taneda. Visualization of separating stokes flows. *Journal of the Physical Society of Japan*, 46(6):1935–1942, 1979. doi:10.1143/JPSJ.46.1935.

[103] Sébastien Tanguy, Michaël Sagan, Benjamin Lalanne, Frédéric Couderc, and Catherine Colin. Benchmarks and numerical methods for the simulation of boiling flows. *Journal of Computational Physics*, 264:1–22, 2014. doi:10.1016/j.jcp.2014.01.014.

[104] T. D. Taylor and Andreas Acrivos. On the deformation and drag of a falling viscous drop at low reynolds number. *Journal of Fluid Mechanics*, 18(3):466–476, 1964. doi:10.1017/S0022112064000349.

[105] S. Tonini and G.E. Cossali. One-dimensional analytical approach to modelling evaporation and heating of deformed drops. *International Journal of Heat and Mass Transfer*, 97:301–307, 2016. ISSN 0017-9310. doi:10.1016/j.ijheatmasstransfer.2016.02.004.

[106] Simona Tonini and G. Cossali. An exact solution of the mass transport equations for spheroidal evaporating drops. *International Journal of Heat and Mass Transfer*, 60: 236–240, 05 2013. doi:10.1016/j.ijheatmasstransfer.2013.01.001.

[107] Mario F. Trujillo. Reexamining the one-fluid formulation for two-phase flows. *International Journal of Multiphase Flow*, 141:103672, 2021. ISSN 0301-9322. doi:10.1016/j.ijmultiphaseflow.2021.103672.

[108] S. Turns. *An Introduction to Combustion: Concepts and Applications*. An Introduction to Combustion: Concepts and Applications. McGraw-Hill Companies, Incorporated. ISBN 9780072300963.

[109] Dennis D van der Voort, Nico J Dam, Herman J H Clercx, and Willem van de Water. Characterization of spray-induced turbulence using fluorescence PIV. *Experiments in Fluids*, 59(7):110, 2018. ISSN 1432-1114. doi:10.1007/s00348-018-2561-9.

[110] Cameron Verwey and Madjid Birouk. Experimental investigation of the effect of droplet

size on the vaporization process in ambient turbulence. *Combustion and Flame*, 182: 288–297, 2017. ISSN 0010-2180. doi:10.1016/j.combustflame.2017.04.027.

[111] Cameron Verwey and Madjid Birouk. Experimental investigation of the effect of natural convection on the evaporation characteristics of small fuel droplets at moderately elevated temperature and pressure. *International Journal of Heat and Mass Transfer*, 118:1046–1055, 2018. ISSN 00179310. doi:10.1016/j.ijheatmasstransfer.2017.11.038.

[112] Emmanuel Villermaux and Benjamin Bossa. Single-drop fragmentation determines size distribution of raindrops. *Nature Physics*, 5(9):697–702, 2009. doi:10.1038/nphys1340.

[113] Henri Werlé. Le tunnel hydrodynamique au service de la recherche aérospatiale. 1974.

[114] C.K. Westbrook and Frederick Dryer. Simplified reaction mechanisms for the oxidation of hydrocarbon fuel in flames. *Combustion Science and Technology - COMBUST SCI TECHNOL*, 27:31–43, 12 1981. doi:10.1080/00102208108946970.

[115] Guang Wu and William A Sirignano. Transient burning of a convective fuel droplet. *Combustion and Flame*, 157(5), 5 2010. ISSN 0010-2180. doi:10.1016/J.COMBUSTFLAME.2009.11.019.

[116] Tianying Xia. *Computational simulation of spherical diffusion flame dynamics and extinction in microgravity.* PhD thesis, Rutgers University-Graduate School-New Brunswick, 2015.

[117] Yuhao Xu. *Combustion dynamics of bio-derived, surrogate, and transportation fuel systems.* PhD thesis, Cornell University, 2017.

[118] Carl L Yaws. *Chemical Properties Handbook*. McGraw-Hill Education, New York, first edit edition, 1999.

[119] M.C. Yuen and L.W. Chen. Heat-transfer measurements of evaporating liquid droplets. *International Journal of Heat and Mass Transfer*, 21(5):537–542, 1978. ISSN 0017-9310. doi:10.1016/0017-9310(78)90049-2.

[120] Hongtao Zhang. Evaporation of a suspended droplet in forced convective high-pressure environments. *Combustion Science and Technology*, 175(12):2237–2268, 2003. ISSN 00102202. doi:10.1080/714923282.

[121] Hongtao Zhang, Vasudevan Raghavan, and George Gogos. Subcritical and supercritical droplet evaporation within a zero-gravity environment: Low Weber number relative motion. *International Communications in Heat and Mass Transfer*, 35(4):385–394, 2008. ISSN 07351933. doi:10.1016/j.icheatmasstransfer.2007.08.002.